Development of Highly Efficient Platinum Nanocatalysts for the Dehydrogenation of Ammonia Borane via Rational Design of Graphitic Carbon Nitride-Based Heterojunction Photocatalysts

by

Merve Aksoy

A Dissertation Submitted to the Graduate
School of Sciences and Engineering in Partial
Fulfillment of the Requirements for
the Degree of

Doctor of Philosophy

in

Material Science and Engineering

KOÇ ÜNİVERSİTESİ

July 9, 2021

Development of Highly Efficient Platinum Nanocatalysts for the Dehydrogenation of Ammonia Borane via Rational Design of Graphitic Carbon Nitride-Based Heterojunction Photocatalysts

Koç University

Graduate School of Sciences and Engineering

This is to certify that I have examined this copy of a doctoral dissertation by

Merve Aksoy

and have found that it is complete and satisfactory in all respects, and that any and all revisions required by the final examining committee have been made.

Committee Members:

Assoc. Prof. Dr. Önder Metin

Assoc. Prof. Dr. Alper Uzun

Assoc. Prof. Dr. Sarp Kaya

Prof. Dr. Selmiye Alkan Gürsel

Prof. Dr. İmren Hatay Patır

Date: 09/07/2021

To all Moms in STEM

Attraversiamo!

ABSTRACT

Development of Highly Efficient Platinum Nanocatalysts for the Dehydrogenation of Ammonia Borane via Rational Design of Graphitic Carbon Nitride-Based Heterojunction Photocatalysts

Merve Aksoy

Doctor of Philosophy in Material Science and Engineering, July 9, 2021

In the last decade, the use of hydrogen as an efficient energy carrier has already been started in fuel cells, portable devices, public transportations, and grid systems thanks to the advancements in the related technologic/scientific area. However, the safe storage and delivery of hydrogen are still on-going challenges in front of the hydrogen energy-based society. The implementation of solid chemical hydrogen storage compounds as the hydrogen energy carrier systems is one of the most promising solutions. Among the solid chemical hydrogen storage materials, ammonia borane (NH_3BH_3, AB) arises as one of the most convenient material for the chemical hydrogen storage owing to its advantageous properties. Among the several methods applied for H_2 generation from AB, the hydrolysis route which results in the release of 3 equivalents of H_2 gas in the presence of a suitable metal catalyst has been mostly preferred one for the mobile applications.

Up to date, numerous catalysts have been tested in the HAB, among which platinum nanoparticles (Pt NPs) supported on high-surface-area and porous materials have been reported with one of the highest catalytic activities for the hydrolysis of AB (HAB). However, those Pt NPs were generally synthesized by following the methods comprising high-temperature surfactant-assisted decomposition and reduction of Pt precursors, and then the obtained highly monodisperse Pt NPs were deposited on a suitable support material to prevent their agglomeration. Supported Pt NPs can also be synthesized by the in-situ synthesis method involving the impregnation of Pt precursor into the support material followed by their reduction in catalytic reaction medium, which has distinct advantages over the initial one such as being sustainable, practical, green, atom-economical, cost-effective, and timesaving. Here, the selection of support material is so crucial to obtain stable and reusable nanocatalysts. Graphitic carbon nitride (g-CN) has been suggested as an appropriate substrate to stabilize Pt NPs due to its nitrogen-rich "six-fold interstices" between tri-s-triazine units, having capability of strong interaction with incorporated metal, and its adjustable surface area and morphology obtained by following different synthesis procedures. Besides, g-CN is a visible light active semiconductor material with suitable band positions for the construction of heterojunctions with Pt NPs and other suitable semiconductor materials.

In this thesis, it was aimed to enhancement of the catalytic activity of Pt nanocatalysts in the HAB via the rational design of g-CN based heterojunction photocatalysts. To fulfill this aim, firstly, a novel method for the in-situ generation of Pt NPs supported on mesoporous g-CN (m-g-CN/Pt) during the catalytic HAB was realized under the white-light irradiation. Secondly, U-g-CN, which was synthesized by using urea as an amine precursor via an easy and green synthesis approach compared to m-g-CN, was used as a support material for the in-situ generation of Pt NPs. U-g-CN/Pt showed better catalytic performance than m-g-CN/Pt nanocatalysts under the same conditions. Next, to further enhancing the catalytic activity of the Pt-based nanocatalysts in the HAB, we turned our attention to the in-situ synthesis of the bimetallic MPt NPs supported on U-g-CN (U-g-

CN/MPt). Indeed, U-g-CN/$Pt_{92}Au_8$ and U-g-CN/$Pt_{85}Au_{15}$ provided a higher catalytic activity (hydrogen production rate of 68.9 and 67.4 L H_2 g_{Pt}^{-1} min^{-1}, respectively) than the monometallic counterpart (60.4 L H_2 g_{Pt}^{-1} min^{-1}), which was attributed to the alloy effect, surface plasmon resonance (SPR) contribution, and the heterojunction formation. Thirdly, on the way to thesis's main goal, we tried to further enhance the activity of Pt nanocatalysts in the HAB by supporting them on U-g-CN/WO_x binary nanocomposites by considering the optical properties and charge kinetics of U-g-CN can be improved via the construction of heterojunction with other semiconductors having proper band gap and band potentials. The results revealed that U-g-CN/a-WO_x/Pt nanocatalysts showed a higher catalytic activity than U-g-CN/Pt by providing a maximum hydrogen production rate of 48.1 L H_2 g_{Pt}^{-1} min^{-1}. All the yielded Pt nanocatalysts (m-g-CN/Pt, U-g-CN/Pt, U-g-CN/MPt, and U-g-CN/a-WO_x/Pt) were characterized via many advanced analytical techniques including TEM, HR-TEM, XPS, XRD, ICP-MS, FTIR, PL, and TRES techniques to clarify the reasons behind the enhanced photocatalytic activities in each step. Moreover, the rate law and the activation parameters were also derived by using the data of kinetic studies. Additionally, a reusability test for each developed Pt based nanocatalyst in HAB was also reported. In summary, this thesis demonstrates that g-CN is a appropriate substrate as support and stabilizer for the in-situ synthesis of catalytically active Pt or MPt NPs in hydrogen production from the HAB due to its availability for rational design of heterostructures.

ÖZET

Grafitik Karbon Nitrür Temelli Heteroeklem Fotokatalizör Tasarımları ile Amonyak Boranın Dehidrojenlenmesinde Etkinliği Yüksek Platin Nanokatalizörlerinin Geliştirilmesi

Merve Aksoy

Malzeme Bilimi ve Mühendisliği, Doktora

9 Temmuz 2021

Yakın geçmişte, ilgili teknolojik/bilimsel alandaki gelişmeler sayesinde hidrojenin verimli bir enerji taşıyıcısı olarak yakıt pillerinde, taşınabilir cihazlarda, toplu taşıma araçlarında ve şebeke sistemlerinde kullanımı başlamıştır. Bununla birlikte, hidrojenin güvenli depolanması ve dağıtımı, hidrojen enerjisine dayalı toplumun önünde hala devam eden zorluklardır. Katı kimyasal hidrojen depolama bileşiklerinin hidrojen enerji taşıyıcı sistemleri olarak uygulanması, en umut verici çözümlerden biridir. Katı kimyasal hidrojen depolama malzemeleri arasında amonyak boran (NH_3BH_3, AB), avantajlı özellikleri nedeniyle kimyasal hidrojen depolaması için en uygun malzemelerden biri olarak karşımıza çıkmaktadır. AB'den H_2 üretimi için uygulanan çeşitli yöntemler sayesinde, uygun bir metal katalizör varlığında 3 eşdeğer H_2 gazının salınmasıyla sonuçlanan hidroliz yöntemi, mobil uygulamalar için en çok tercih edilen yöntemdir.

Bugüne kadar test edilen çok sayıda katalizör arasından, yüksek yüzey alanlı ve gözenekli malzemeler üzerinde desteklenen Platin nanopartiküller (Pt NP'ler), AB hidrolizi için en yüksek katalitik aktivitelerden biri olarak rapor edilmiştir. Bununla birlikte, bu Pt NP'ler genellikle yüksek sıcaklıkta yüzey aktif madde destekli ayrışma ve Pt öncüllerinin indirgenmesini içeren özel yöntemler izlenerek sentezlenir ve daha sonra elde edilen yüksek oranda tekil dağılımlı Pt NP'ler, aglomerasyonlarını önlemek için uygun bir destek malzemesi üzerinde biriktirilir. Desteklenen Pt NP'leri sentezlemenin bir başka yolu, Pt öncülünün destek malzemesine emdirilmesi ve ardından bunların katalitik reaksiyon ortamında indirgenmesini içeren yerinde sentez yöntemidir. Bu yöntem, sürdürülebilir, pratik, yeşil, atom ekonomik, uygun maliyetli ve zaman kazandıran olma gibi ilkine göre belirgin avantajlara sahiptir. Burada, kararlı ve yeniden kullanılabilir nanokatalizörler elde etmek için destek malzemesinin seçimi çok önemlidir. Grafitik karbon nitrür (g-CN), tri-s-triazin birimleri arasındaki nitrojen bakımından zengin "altı katlı boşlukları" nedeniyle Pt NP'leri stabilize etmek için uygun bir substrat olarak önerilmiştir. Ek olarak, metal ile güçlü etkileşim kabiliyeti ve farklı sentez prosedürleri izlenerek elde edilen ayarlanabilir yüzey alanı ve morfolojisine sahiptir. Ayrıca g-CN, Pt NP'ler ve diğer uygun yarı iletken malzemelerle heteroeklemlerin inşası için mevcut bant konumlarına sahip, görünür ışıkta aktif bir yarı iletken malzemedir.

Bu tezde, g-CN bazlı heteroeklem fotokatalizörlerin rasyonel tasarımı ile AB hidrolizinde Pt nanokatalizörlerinin katalitik aktivitesinin arttırılması amaçlanmıştır. Bu amacı gerçekleştirmek için, ilk olarak, beyaz ışık altında AB'nin katalitik hidrolizi sırasında mezogözenekli g-CN üzerinde desteklenen Pt NP'lerin (m-g-CN/Pt) yerinde üretimi için yeni bir yöntem geliştirilmiştir. İkinci olarak, m-g-CN' ye kıyasla kolay ve yeşil bir sentez yaklaşımıyla, bir amin öncüsü olarak üre kullanılarak sentezlenen U-g-CN, Pt NP' lerin yerinde üretimi için bir destek malzemesi olarak kullanılmıştır. U-g-CN/Pt, aynı koşullar altında m-g-CN/Pt nanokatalizörlerinden daha iyi katalitik performans göstermiştir. Daha sonra, Pt bazlı nanokatalizörlerin AB hidrolizinde katalitik aktivitesini daha da arttırmak için, dikkatimizi U-g-CN üzerinde desteklenen bimetalik MPt NP' lerin

(U-g-CN/MPt) yerinde sentezine çevirdik. Gerçekten de, U-g-CN/$Pt_{92}Au_8$ ve U-g-CN/$Pt_{85}Au_{15}$ nanokatalizörleri, sırasıyla 68.9 ve 67.4 L H_2 g_{Pt}^{-1} min^{-1} hidrogen üretim hızı sağlayarak, monometalik muadiline kıyasla (60.4 L H_2 g_{Pt}^{-1} min^{-1}) daha yüksek bir katalitik aktivite sağlamıştır. Elde edilen bu aktivite artışı, alaşım etkisine, yüzey plazmon rezonans (SPR) katkısına ve heterojunction oluşumuna atfedilmiştir. Üçüncü olarak, tezin asıl amacına uygun olarak, U-g-CN' nin optik özelliklerini ve yük kinetiğini göz önünde bulundurarak ve uygun bant aralığına ve bant potansiyellerine sahip diğer yarı iletkenlerle heteroeklem inşa ederek, Pt NP lerin U-g-CN/WO_x ikili nanokompozitleri üzerinde desteklenmesiyle, Pt nanokatalizörlerinin AB hidrolizindeki aktivitelerini daha da arttırmak amaçlanmıştır. Sonuçlar, U-g-CN/WO_x/Pt nanokatalizörlerinin, maksimum 48.1 L H_2 g_{Pt}^{-1} min^{-1} hidrojen üretim hızı sağlayarak U-g-CN/Pt' den daha yüksek bir katalitik aktivite gösterdiğini ortaya konulmuştur. Elde edilen tüm Pt nanokatalizörleri (m-g-CN/Pt, U-g-CN/Pt, U-g-CN/MPt ve U-g-CN/WOx/Pt), TEM, HR-TEM, XPS, XRD, ICP-MS, FTIR, PL ve TRES teknikleri ile karakterize edilerek, her adımda daha da gelişmiş fotokatalitik aktivitelerin arkasındaki nedenler açıklığa kavuşturulmuştur. Ayrıca AB hidrolizinde geliştirilen her Pt bazlı nanokatalizör için kinetik çalışmaların sonuçları, hız denklemi, aktivasyon parametreleri ve yeniden kullanılabilirlik testi de rapor edilmiştir. Özetle bu tez, g-CN' nin heteroyapıların rasyonel tasarımı için elverişliliği nedeniyle, AB'nin hidrolizinden hidrojen üretiminde katalitik olarak aktif Pt veya MPt NP'lerin yerinde sentezi için destek ve stabilizatör olarak, uygun bir substrat olduğunu göstermektedir.

ACKNOWLEDGMENTS

Firstly, I would like to express my sincere gratitude to my advisor Assoc. Prof. Dr. Önder Metin for his continuous support, guidance, motivation, and immense knowledge. His guidance not only helped me to conduct my research and compiling this thesis, but also taught me how to manage my time more effectively for both solid research in lab and literature survey. His words 'read at least 1 paper before you sleep' are very taught provoking and ignited a zeal to read more papers. He shared his views and ideas on literature improving our understanding of photocatalysis, inspiring me to read more and work efficiently.

Besides my advisor, I would like to thank the rest of my thesis committee: Assoc. Prof. Dr. Alper Uzun, Assoc. Prof. Dr. Sarp Kaya, Prof. Dr. Selmiye Alkan Gürsel, and Prof. Dr. İmren Hatay Patır, for their insightful comments and hard questions which encouraged me to expand my research with the contribution of different perspectives.

I would like to thank KUYTAM and KUTEM family for being open door for the use of their facilities. Assoc. Dr. Gülsu Şimsek Franci, Dr. Barış Yağcı, and Dr. Hadi Jahangiri, your contribution in the characterization part of this thesis is very precious and valuble to me. Thanks for always being helpful and good-humored.

My sincere thanks also goes to Dr. Sibel Eken Korkut, Dr. Orhan Altan, Dr. Erbay Kalay, Dr. Sepideh Behboudikhiavi, and Dr. Melek Şermin Özer for their continous support, love, knowledge, and peaceful atmosphere they created/maintained in the lab. Sibel Hocam, you have been an elder sister to me, you were always there in the worst time for me with your endless patience and life experiences. I will always appreciate and remember with respect and love. Orhan Hocam, your knowledge, desire to share your ideas in a modesty, and your life perspective makes me admire you. Erbay Hocam, you are the unforgettable smiley face of the lab with your immortal words "there is no wrong possible with us". Sepideh, we will meet in the future in somewhere having natural wonders such as "Niagara waterfall". Melek Hocam, even though you mostly prefer dressed in black, we all know that your character which is full of beautiful colors makes the lab environment more enjoyable and colorful.

My special thanks also goes to my colleaques in the lab, Hüseyin Küçükkeçeci, Buse Sündü, Begümhan Karapınar, Zafer Eroğlu, Seda Yılmaz, Ahsen Sare Yalın, and Temirlan Kubanaliev. Buse, with your helpfulness, endless positivity, and delicious food we shared, you make the lab environment more enjoyable. Zafer and Hüseyin, you both together did really good job for the organization of lab space for better productivity that I will always appreciate. Begüm, you are one of the most ambitious woman I met, and I am sure that you will achieve great success in your PhD and future endeavors. Ahsen, Seda, and Temirlan, you are the most cute and colorful people of the lab with your special personalities. Thanks to all of you for your roles that make my experiences more enjoyable.

I am so grateful to my family for their intimate love and support from my early youth up to now. My mother, Ülfet Demirkıran, had you not taken care of my son in the hardest time of babycare, I could never ever finish my PhD. And my best friend, Aylin Çapkınlar, you are marvelous and I am lucky to have a friend like you. And, my dude, my elder brother, Dr. Satya Vijaya Kumar Nune, even though you are far away, I always feel your love, prayers, and confidence in me.

Last but not the least, my heartful gratitude goes to my dear husband, Mehmet Fatih Aksoy. You make the most important contribution to this thesis with your encouragement, inspiration, and self-sacrifice. It was great comfort to know that you support my decisions. And my cute son, Akif Yiğit Aksoy, you are the best thing that ever happened in my life.

TABLE OF CONTENTS

LIST OF TABLES

LIST OF FIGURES

ABBREVIATIONS

AB	Ammonia Borane
HAB	Hydrolysis of Ammonia Borane
Pt NPs	Platinum Nanoparticles
g-CN	Graphitic Carbon Nitride
m-g-CN	Mesoporous Graphitic Carbon Nitride
m-g-CN/Pt(IV)	Platinum Ion Impregnated Mesoporous Graphitic Carbon Nitride Nanocomposites
m-g-CN/Pt	Platinum Nanoparticles Supported on Mesoporous Graphitic Carbon Nitride Nanocatalysts
U-g-CN	Graphitic Carbon Nitride from Urea Pyrolysis
U-g-CN/Pt(IV)	Platinum Ion Impregnated Graphitic Carbon Nitride from Urea Nanocomposites
U-g-CN/Pt	Platinum Nanoparticles Supported on Graphitic Carbon Nitride from Urea Pyrolysis
MPt NPs	Bimetallic Pt Nanoparticles
PtAu NPs	Platinum-Gold Nanoparticles
U-g-CN/MPt	Bimetallic MPt Nanoparticles Supported on Graphitic Carbon Nitride from Urea Pyrolysis
WO_x	Oxygen-deficient/non-stoichiometric Tungsten Oxide
a-WO_x	Amorphous Oxygen-deficient/non-stoichiometric Tungsten Oxide
U-g-CN/WO_x	Composition of Graphitic Carbon Nitride from Urea Pyrolysis and Oxygen-deficient/non-stoichiometric Tungsten Oxide
U-g-CN/WO_x/Pt(IV)	Platinum Ion Impregnated Composition of Graphitic Carbon Nitride from Urea Pyrolysis and Oxygen-deficient/non-stoichiometric Tungsten Oxide
U-g-CN/WO_x/Pt	Platinum Nanoparticles Supported on Composition of Graphitic Carbon Nitride from Urea Pyrolysis and Oxygen- deficient/non-stoichiometric Tungsten Oxide

U-g-CN/a-WO_x/Pt	Platinum Nanoparticles Supported on Composition of Graphitic Carbon Nitride from Urea Pyrolysis and Amorphous Oxygen deficient/non-stoichiometric Tungsten Oxide
TEM	Transmission Electron Microscopy
HR-TEM	High Resolution- Transmission Electron Microscopy
XPS	X-Ray Photoelectron Spectroscopy
XRD	X-Ray Diffractometry
ICP-MS	Inductively Coupled Plasma Mass Spectrometry
FT-IR	Fourier Transformation Infrared Spectroscopy
PL	Photoluminescence Spectroscopy
TRES	Time-resolved Emission Spectroscopy

Chapter 1

INTRODUCTION

1.1 Motivation: Energy and Environment

Currently, the world's energy demand is mostly supplied by fossil fuels including coal, oil, and natural gas. However, shifting from fossil fuels to the more sustainable and cleaner energy technologies is a must case scenario due to the possible depletion of fossil fuels one day in future and the serious environmental problems caused by the greenhouse gases emitted into atmosphere. Worst of all, it is expected that global temperature will rise at least 3 ^{o}C by the end of the century if the CO_2 emission to the atmosphere continues to increase in this manner, which will have a huge impact on the current climatic conditions. For the sake of better future, the present energy sources must be replaced with the cleaner, affordable, and sustainable energy sources.[1]

With the above perspective, various types of renewable energy sources including solar and wind energy have been widely studied to replace the fossil fuels. The major problem with these renewable energy sources is being discontinues and seasonal such that solar energy is only produced during the day if the weather is sunny and wind energy is only produced when it is windy. Moreover, these energy sources are not available in all geographies of the world at sufficient amount. Therefore, excess of energy generated by these renewable energy sources must be stored for later usage. However, there is currently no energy storage system better than rechargeable metal batteries which are still quite costly, and their storage capacities are limited.[2], [3] Another promising solution to the future energy problem is to use of hydrogen energy carrier, which is the chemical energy stored in hydrogen gas.[4] Hydrogen is the most abundant element in the universe, and it is already used in chemical industry as a feedstock. Due to its carbon free emission property and largest energy density by mass which is approximately 120 MJ/kg, almost three times more than diesel or gasoline, hydrogen is attracting a lot of attention as a green energy carrier to replace the carbon based energy infrastructure.[5], [6] The production of hydrogen takes place by means of steam reforming of methane, a process ends up with unwanted by-products carbon dioxide (CO_2) and carbon monoxide (CO). An alternative way to avoid this is to use renewable energy sources to produce H_2.

For example, an electric current splits water into hydrogen (H_2) and oxygen (O_2), namely water splitting, so that if any excess electricity generated by solar panels, wind turbines or other renewable energy systems could be used to split water into H_2 and O_2 and the produced H_2 could be stored for later use, then hydrogen will be considered renewable as well. Afterwards, the stored hydrogen is converted back into the other energy forms via direct combustion or a fuel cell for domestic and industrial use, with only emission of pure water.

Thanks to the advancement in the field, hydrogen has been utilized as an energy carrier in small electronics to stationary applications, and even for aircrafts, buses, and passenger cars through the fuel cells. As an example, hydrogen powered electric bicycles (Hy-Cycle) produced by Merlin Energy Research group in Sydney since 2016 and the hydrogen powered Toyota Mirai cars available since 2014 are already market ready products. Lastly, the world's largest hydrogen plant opened in Fukushima by Toshiba corporation in 2020 was also shown in Figure 1.1. This solar-powered hydrogen station aims to maximize the utilization of green hydrogen in low cost and to produce enough hydrogen gas for the mobility devices, fuel cell cars, and more, to facilitate the penetration of hydrogen energy into our daily life.

Figure 1.1: Hydrogen powered bicycle (Hy-Cycle), Hydrogen powered car (Toyota Mirai), and Fukushima Hydrogen Energy Research Field (FH_2R).

However, the safe and efficient storage of hydrogen are still ongoing obstacles in front of its widespread application, especially in on-board systems.[7] On a mass basis, hydrogen has the largest energy density, but it suffers in volumetric density by reason of being the lightest gas in the universe. Currently, hydrogen is generally compacted into much smaller volumes by following physical storage methods based on either compression or cooling or combination of both, called cryogenic compression, which makes it expensive, unsafe, and impractical (Figure 1.2). Therefore, development of cheap, safe, and efficient ways to store hydrogen is highly required.

1.2 Hydrogen Storage

Numerous material-based technologies have been developed for efficient and safe hydrogen storage.[8] Figure 1.2 summarizes the material-based hydrogen storage technologies in solid phase. Among them, surface hydrogen storage systems, known as sorbents storing hydrogen via physical adsorption, such as carbonaceous materials (activated carbon[9], graphene[10], carbon nanotubes[11]), zeolites[12], and metal-organic frameworks (MOFs)[13] have been investigated for a long time owing to their high porosity, controllable structural characteristics, and high specific surface area which allow higher hydrogen uptake. Despite reversible nature of the hydrogen adsorption/desorption process for the high surface area sorbents, they suffer from having lower hydrogen capacity at mild operating conditions.[14]

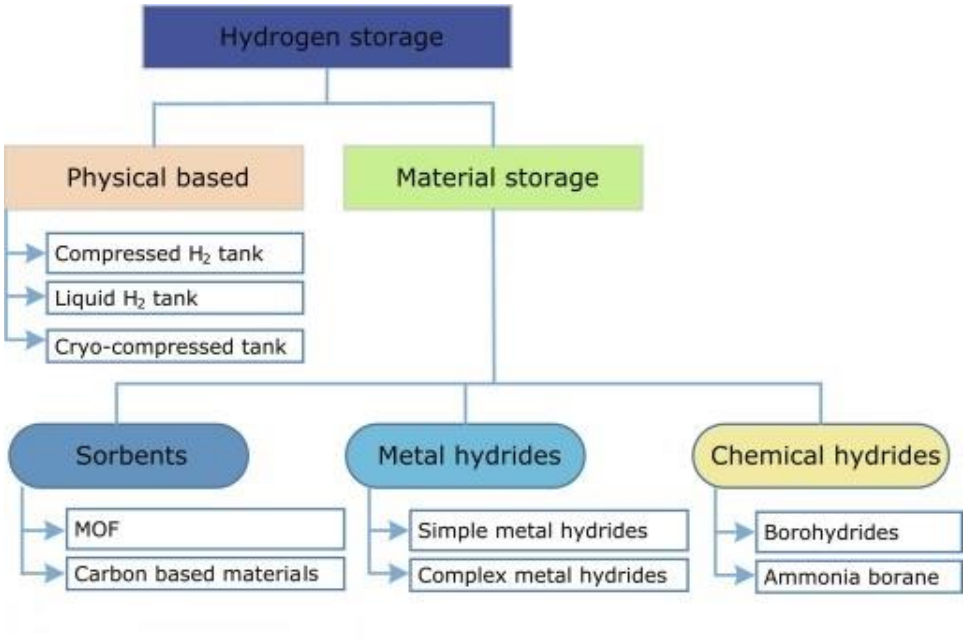

Figure 1.2: Different methodologies available for hydrogen storage.[15]

On the other hand, metal hydrides[16], one of the most widely studied solid state hydrogen storage materials, store hydrogen molecules via incorporating them into the metal lattice, in which the interstitial sites are occupied with hydrides, and finally released the molecular hydrogen upon sufficient heating. However, these materials also have several drawbacks such as having a limited hydrogen storage capacity and requirement of high temperatures for realizing the stored hydrogen. On the contrary, in complex metal or non-metal hydrides, hydrogen is covalently bound to a non-metal atom such as boron to form a complex compound with another molecule with lone pair or an anion that is stabilized with a cation. Some of the best-known complex metal hydrides are $LiBH_4$ and $NaBH_4$. Due to their high total hydrogen content (up to 18.5% by weight for $LiBH_4$), these metal borohydrides have been extensively studied as possible hydrogen storage materials. After all, the research on complex hydrides for hydrogen storage tends to investigate on amine-boranes owing to their unique properties with relatively their high hydrogen contents in mass due to their low molecular weights. Among them, ammonia borane (H_3NBH_3, AB), as the simplest amine-borane, has been regarded as one of the best candidates for the solid-state hydrogen storage. Figure 3 shows a graphical presentation of the some briefly described hydrogen storage materials with respect to volumetric and gravimetric hydrogen density.[17]

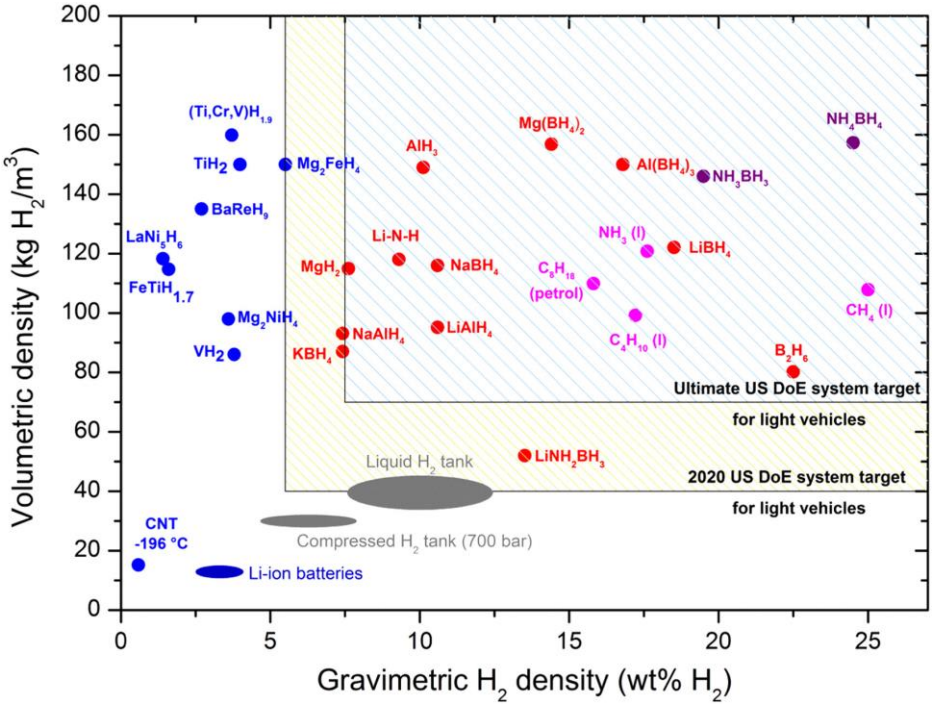

Figure 1.3: Volumetric and gravimetric hydrogen density of selected H_2 storage materials, shown along with the U.S. Department of Energy targets for the hydrogen storage system for comparison.[17]

Besides the above-mentioned solid state hydrogen storage materials, there are several other liquid organic hydrogen storage materials[18], which are mostly unsaturated organic compounds with high hydrogen absorption capacity such as N-ethyl carbazole, due to their convenient handling. In addition, formic acid as a non-toxic, stable, and low-cost organic material, has been also offered as another option for chemical hydrogen storage in liquid state.[19]

1.3 Ammonia Borane as Hydrogen Storage Material

1.3.1 General Properties of Ammonia Borane

Ammonia borane (AB) has attracted attention as a hydrogen storage material for nearly 15 years due to its high gravimetric hydrogen content (19.6% by weight), non-toxicity, and stability in solution under solid or ambient conditions. AB is a colorless molecular crystal with a density of 0.74 g mL^{-1} with a high solubility in water and other relatively polar solvents such as methanol. It is a typical electron donor- acceptor (lewis acid-base) complex formed between NH_3 and BH_3 molecules so that it includes three N-H and B-H covalent bonds and one N-B coordinate covalent bond. The complex is in an arrangement of staggered conformation via reverse alignments of N and B atoms along z-axis, like geometry of isoelectronic ethane (C_2H_6) (Figure 1.4). Its crystal structure is body-centered tetragonal with space group of I4mm at room temperature. Due to the difference in electronegativity of N and B atoms, the hydrogen atoms attached to them acquire different polarity so that hydrogen atoms attached to N and B become partially positive and partially negative, respectively. This results in strong intra-/inter-molecular interaction called as "dihydrogen bonding" originating from $N—H^{\delta+}\cdots{}^{\delta-}H—B$ charge transfer, leading to facile release of H_2. Thus, it can also be used as a reducing agent to convert aldehydes or ketones to alcohols and some metal ions to metal nanoparticles.[20], [21]

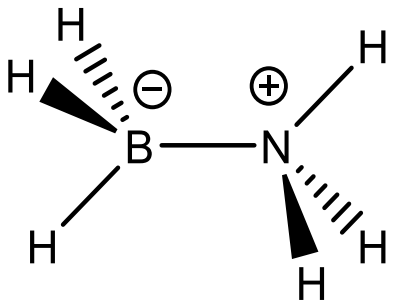

Figure 1.4: Molecular structure of Ammonia Borane.

Even though the synthesis of AB was reported much earlier, in 1955 by Shore and Parry, its capability as a hydrogen storage material has been recently investigated. There are two main ways of producing hydrogen from AB, which are thermolysis and solvolysis. Thermolysis is a three-step process in which one-third of the hydrogen content is released via producing polyaminoborane, polyiminoborane, and boron nitride, respectively. 1 equivalent of H_2 is released at moderate temperatures (~110 °C) and intramolecular polymerization takes place at around 125 °C. 2 equivalents of H_2 is released at temperature of 150-200 °C, but third equivalent of H_2 is released at high temperatures more than 500 °C due to high stability of AB. Besides the requirement of high temperature for the release of 3 equiv. H_2, the thermal decomposition of AB also suffers from the harmful side product formation such as borane, ammonia, borazine, and slow hydrogen release kinetics.[22]–[24] The release of hydrogen along thermal treatment can be summarized in the following equations (1-4):

$$\boldsymbol{H_3NBH_3 \rightarrow H_2NBH_2 + H_2} \quad (\sim 110\ ^{o}C) \quad (1)$$

$$\boldsymbol{n(H_2NBH_2) \rightarrow (H_2NBH_2)_n} \quad (125\ ^{o}C) \quad (2)$$

$$\boldsymbol{1/n(H_2NBH_2)_n \rightarrow 1/n(HNBH)_n + H_2} \quad (150\text{-}200\ ^{o}C) \quad (3)$$

$$\boldsymbol{1/n(HNBH)_n \rightarrow BN + H_2} \quad (>500^{o}\ C) \quad (4)$$

On the contrary, solvolysis of AB, classified as either alcoholysis or hydrolysis, provides more convenient route to dehydrogenation of AB under mild conditions. In the solvolysis reactions, $H^{\delta-}$ bonded to the B atom interacts with the $H^{\delta+}$ of the protic solvent and 3 equivalents of H_2 is released along with B-containing species as by-products, according to the equation (5) and (6) as shown below:

$$\boldsymbol{H_3NBH_3 + 2\,H_2O \rightarrow NH_4BO_2 + 3\,H_2} \quad (5)$$

$$\boldsymbol{H_3NBH_3 + 4\,ROH \rightarrow NH_4B(OR)_4 + 3H_2} \quad (6)$$

Compared with the thermolysis and alcoholysis, HAB has certain advantages such as providing faster hydrogen liberation rate under ambient conditions and being more environmental friendly and cost-effective.[20], [22] However, the HAB with a remarkable H_2 generation rate can only be achieved in the presence of an acid (cation exchange resins, zeolites, and even CO_2) or a metal catalyst due to the intramolecular dihydrogen bonding, causing AB to be relatively stable against hydrolysis under neutral or alkaline conditions.[25], [26]

1.3.2 Investigation of metal catalyzed HAB

A certain understanding of metal catalyzed HAB has been established through some mechanistic studies. For example, Xu and Chandra illustrated that AB interacts with the catalyst surface and then converted to an activated complex which dissociates and releases H_2 upon attack of H_2O.[27] A similar mechanism was also pointed out by Chen et al. that presents H_2O reaction with a transient M-H (where M is metal catalyst) bond to release H_2 (Figure 1.5). It is concluded that the transient M-H bond formation is the prerequisite for the hydrolytic reaction and it is directly related to the properties of metal catalysts.[28]

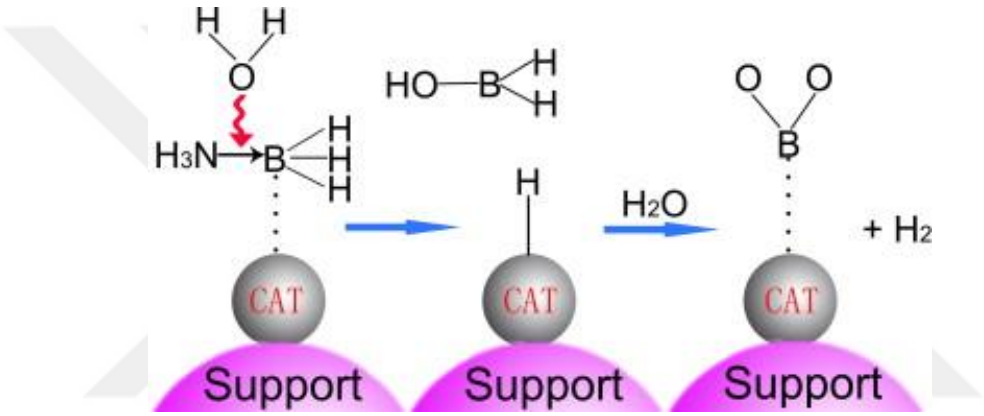

Figure 1.5: Schematic representation of hydrolysis of NH_3BH_3 in the presence of supported metal catalysts.[28]

In another study, Che and coworkers observed increased rate of H_2 release in the presence of OH^- anion that may result from changes in the chemical environment on the catalyst's surface. Moreover, they confirmed that the half of the released H_2 comes from H_2O rather than OH^- by conducting an isotopic labeling experiment within the experimental error limits of isotopic exchange, in which D_2O was used as the solvent for hydrolytic dehydrogenation of AB.[29] Lu et al. reported that the significant increase in the reaction rate with the addition of OH^- ions is related to the hydrolysis mechanism of AB which is shown in Figure 1.6.[30] As it is also proven by Hou et al.[31], multiple SN_2 reactions occur in the HAB process. The OH* reacts with the $–BH_3$ group in NH_3BH_3*, followed by the dissociation of B–N bond in NH_3BH_3 to form the BH_3OH* group, which is major intermediate during all reaction. At the end of three cycles, $BH_2(OH)_2$* and $BH(OH)_3$* are also generated along with release of 3 equivalents of H_2 gas using one hydrogen atom from the $–BH_3$ group of AB and one from the H_2O. Even though the rapid generation of BH_3OH*, $BH_2(OH)_2$*, and $BH(OH)_3$* intermediates, which results in a facile hydrogen

generation process, is achieved in the presence of OH^-, the addition of too much OH^- leads to competitive adsorption with water molecules and inhibition of hydrolysis.

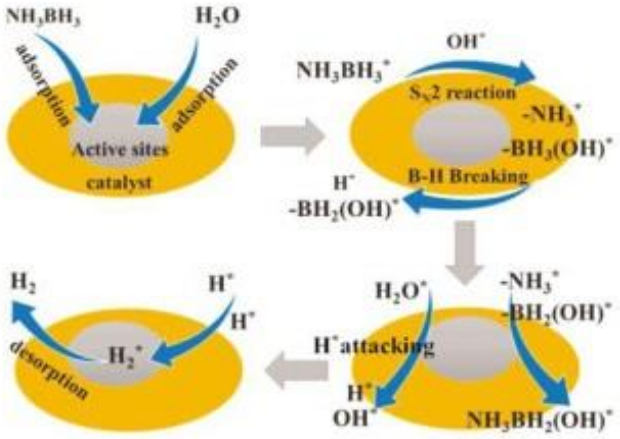

Figure 1.6: A schematic diagram of the AB hydrolytic dehydrogenation process under appropriate catalyst.[30]

For a more efficient HAB, the rate determining step (RDS), which is the most difficult step in the whole process, should be taken into consideration mainly. Therefore, many different aspects have been put forward to provide an understanding of RDS of HAB. For instance, Astruc and his co-workers carried out some mechanistic studies on the catalytic HAB using kinetic isotope effects and reported that the cleavage of an O-H bond in H_2O is the RDS in the HAB.[32] Lu and coworkers found that the RDS of HAB includes two possible activation processes which are synchronous activation of B-H bond in AB and O-H bond in water molecule. They synthesized CoRu alloy nanocatalysts, in which Ru atoms act as active sites for activation of BH bonds, providing adsorption hydrogen atoms on the catalyst surface, and acidic sites of nearby Co atoms work to activate OH bonds in HO for the formation of adsorption hydrogen atoms. and OH radicals on the catalyst surface.[33] It can be concluded that RDS of HAB was closely dependent on the catalyst and it might vary depending on metal catalyst type, reaction medium, and even temperature.[20]

The hydrogen generation specific rate (r) and turnover frequency (TOF) have been used to calculate and compare the activity of metal catalysts. Equations (7) and (8) show these quantities in which Δt is the required time for the generation of ΔV_{H_2} volume or n_{H_2} moles of hydrogen gas. Additionally, n_M and M_w is the molar and mass amount of the metal in the catalyst, respectively.

$$\boldsymbol{r = \frac{\Delta V_{H_2}}{\Delta t * M_W}} \tag{7}$$

$$\boldsymbol{TOF = \frac{n_{H_2}}{\Delta t * n_M}} \tag{8}$$

Another measured parameter of the HAB is its apparent activation energy (E_a) which plays an important role to understand kinetic characteristics of the metal catalyzed hydrolysis reaction. E_a value is calculated according to the Arrhenius equation as illustrated in Equation 9 where k_0 represents the rate constant, R is ideal gas constant, T is the temperature of reaction, and A denotes the pre-exponential factor.

$$\boldsymbol{lnk_0 = \frac{-E_a}{R * T} + lnA} \tag{9}$$

Additionally, the durability test is very essential to investigate the ability of the metal catalyst to maintain its initial activity. The active sites of the metal catalyst can be destroyed along with the collapse of the nanostructure or agglomeration of the metal nanoparticles, which results in decrease of its initial activity. For this reason, the stability of metal catalyst should be improved for a better result of durability and practical application of the catalyst in HAB along with being highly efficient, easily prepared and recovered, non-toxic and economical.

1.4 The literature survey on the catalysts tested in the HAB

Up to now, numerous transition metal catalysts including excellent noble metal catalysts (such as Rh, Ru, Pd and Pt)[34]–[40] and inexpensive non-noble metal catalysts (such as Ni, Co, Fe and Cu)[41]–[48] have been investigated for the HAB. One of the smart ways to produce highly efficient metal catalyst for HAB is to increase the number of surface-active sites via enlarging specific surface area of the catalyst. For this reason, zero valent well-dispersed metal nanoparticles/clusters having small particle size and large specific surface

area have been extensively studied. The activity enhancement of single- metal nanoparticles is provided by alloying them with a second or third metal, which is generally a cheaper metal than the first one so that the cost of the catalyst can be reduced as well. The rationale behind this is that blending of different types of metal brings in special electronic interactions derived from synergistic effects between them. Thus, bi/trimetallic nanoparticles show improved chemical/physical properties strongly depending on their composition, shape, and size.[49]–[56] Although these metal NPs exhibit excellent catalytic activities in HAB, they usually suffer from deficiency in stability and durability due to their agglomeration or dissociation during the reaction. For this reason, many researchers have been recently worked on the improvement of the cycling stability of metal NPs by introducing a large variety of support materials, especially the ones having large surface area, high porosity, and surface functionality.

In addition to zero valent nanocatalysts, non-zero valent metal catalysts such as oxides[57]–[62], phosphides[63]–[65], and borides[66], [67] have been also examined and found highly effective catalyst in HAB due to their varied elemental composition and diverse electronic structure. Among all the mentioned catalysts, platinum (Pt) based nanocatalysts, which is including Pt NPs or their derivatives anchored on a suitable support material, have been reported with one of the highest activity in HAB. Since the aim of the current thesis is to illustrate the development of highly efficient Pt based nanocatalysts in catalytic HAB, the Pt based nanocatalysts that have been tested in the HAB were summarized below.

1.4.1 Platinum based nanocatalysts for HAB

Mostly, highly dispersed mono/bimetallic Pt NPs are prepared by following colloidal synthesis methods which generally require the reduction of Pt precursor at high temperatures in the presence of long-chain stabilizing agent(s) and organic solvent.[68] Although the synthesized colloidal Pt NPs may have very good uniformity, clear shape and small size, they have very high surface energies and tend to agglomerate and form larger size to reduce their surface energy. Therefore, these monodispersed Pt NPs are assembled on an appropriate support material via liquid self-assembly method to maintain their stability and catalytic activity, and to resolve recycling issue to some extent.

Another synthesis route which does not require high temperature, organic phase, and difficulty in removing long-chain stabilizers, which block metal active sites and result in decrease of catalytic activity, includes the impregnation of Pt precursors in a suitable support material followed by reduction of impregnated Pt ions via a reducing agent under

ambient conditions. In this method, the selection of support material is extremely important to obtain highly dispersed and stable Pt NPs since the chosen support material is also expected to act as a stabilizer. An ideal support material should have suitable functional groups and a reasonable surface area to ensure strong binding and good dispersion of Pt NPs, respectively, on the support, in addition to being cost-effective and environmentally friendly.

Pt based nanocatalysts for the hydrolytic dehydrogenation of AB reported between 2014 and 2021 were summarized in Table 1.1. Among the reported studies, one of the highest activities belong to the $PtCo_{20}$/CNTs catalyst, which is 1.8 times higher than its monometallic counterpart. It is revealed that decoration of CoO on Pt by 20 cycle of ALD provides a unique Pt-Co interfaces and targeted Pt electronic properties which is lowering activation energy and promoting O-H bond cleavage being rate determining step.[69] In other study in which the importance of the interaction between the metal NPs and support was pronounced, the electronic environment of Pt NPs was modified by oxidizing the surface of MXenes with ozone such that deposited Pt NPs on this surface have shown high dispersion with less average particle size along with modified electronic environment. This electronic modification is believed to enhance the catalytic activity of Pt NPs.[70]

Although great development has been achieved in Pt based nanocatalysts only a few studies showed that hybrid nanocatalysts, including Pt NPs and visible light active support materials, were used as a photocatalysts for hydrogen evolution reaction from AB.[71] Considering environmental friendliness, cost, and green chemistry, some new methods such as fabrication of effective photocatalyst should be also developed for promoting the HAB. For this reason, graphitic carbon nitride (g-CN) as a semiconductor having dual role of being both support and stabilizer for the growth of Pt NPs is suggested as a candidate due to its unique properties as discussed in following part.

Table 1.1: Catalytic activity of some Platinum based nanocatalysts for the HAB published between 2014 and 2021.

Metal Catalyst	TOF (mol_{H2} min^{-1} mol_{Pt}^{-1}) @ 25 °C	Ea (kJ/mol)	Cycle number	Maintaining initial Catalytic Activity	Ref.
Pt/MXene-H_2O	272 (@30 °C)	99	-	-	[70]
PtPd DEN	108.5	47.8	-	-	[72]
Pt-Al alloy	82.8 L H_2 min^{-1} g^{-1}catalyst (rate)	20.4	10	90	[73]
$Pt_{0.5}Ni_{0.5}$/g-C_3N_4	250.8 (10 °C)	38.09	10	55	[54]
Pt/CNT-G	135	35.34	-	-	[74]
Pt@PC-POP	55.62	56.42	5	~100	[75]
PtCo20/CNTs	675.1	42.5	-	-	[55]
Pt@CF-12	17.8 L H_2 $min^{-1}g^{-1}$cat (rate) (30 °C)	30.67	7	100	[76]
hnp–$Pt_{35}Cu_{65}$	108	40.5	5	68	[77]
NP $Pt_{40}Co_{60}/Co_3O_4$	131	38.8	5	65	[78]
Pt(8%)/CCF-500	35.0	39.2	5	~100	[79]
KB-$Cu_{68}Pt_{32}$	859	39	5	75	[56]
SNP-$Pt_{65}Ti_{35}$	51.4	39.4	5	63	[80]
Pt20/CNT (by ALD)	416.5	48.3 ± 1.2	4	40	[81]
Pt-CeO_2 /rGO NC	93.8	64.7	10	92	[82]
NP-$Pt_{70}Ru_{30}$	59.6	38.9	5	70	[83]
PC3/SAG	123.1	30.2	2	100	[84]
Pt@SiO_2	158.6	-	5	~100	[85]
Pd–Pt@PVP NPs	125	51.7 ± 2	5	61	[86]
Pt–Ru@PVP NPs	308.0	56.3 ± 2	5	72	[87]

DEN=Dendrimer-Encapsulated Nanoparticle, g-C_3N_4=Graphitic Carbon Nitride, CNT-G=Carbon Nanotube-Graphene, PC-POP=Porous Organic Polymers, CNT=Carbon Nanotube, CF-12=Carboxylic acid functionalized 3D cage-type mesoporous silica FDU-12, hnp= hierarchical nanoporous, NP=Nanoporous, CCF=Cotton Derived Carbon Fibers, KB=Ketjen Black, SNP=Stratified Nanoporous, ALD=Atomic Layer Deposition, rGO=reduced Graphene Oxide, NC=Nanocomposites, PC/SAG=Platinum-Cobalt/Mesoporous Silica Aerogel, PVP=Poly(N-vinyl-2-Pyrrolidone)-stabilized.

1.5 Graphitic Carbon Nitride based photocatalytic materials

1.5.1. General properties of graphitic carbon nitride

Graphitic carbon nitride (g-CN), a polymeric n- type semiconductor material, has been widely used as a photocatalyst due to its high thermal and chemical stability, non-toxicity, and facile large-scale synthesis. It is a metal-free semiconductor which is composed of earth abundant C, N, and peddle H and O atoms. It is built up through the stacking of 2D layers consisting of tri-s-triazine (heptazine) units linked by amino groups (Figure 1.7). There are strong van der Waals forces between the layers of g-CN contributing to its chemical stability. Indeed, g-CN is dispersible and stable in many polar solvents such as water, alcohol, dimethylformamide (DMF), and dimethylsulfoxide (DMSO) for a long time. In addition to its chemical stability, it also shows high thermal stability at high temperatures as much as 650 ^{o}C, which is attributed to the stability of C-N aromatic heterocycles. It can be synthesized by thermal polymerization of several N-rich precursors such as urea, thiourea, guanidine hydrochloride, melamine, cyanamide, dicyandiamide, or their mixture between 450-650 ^{o}C as shown in Figure 1.7.

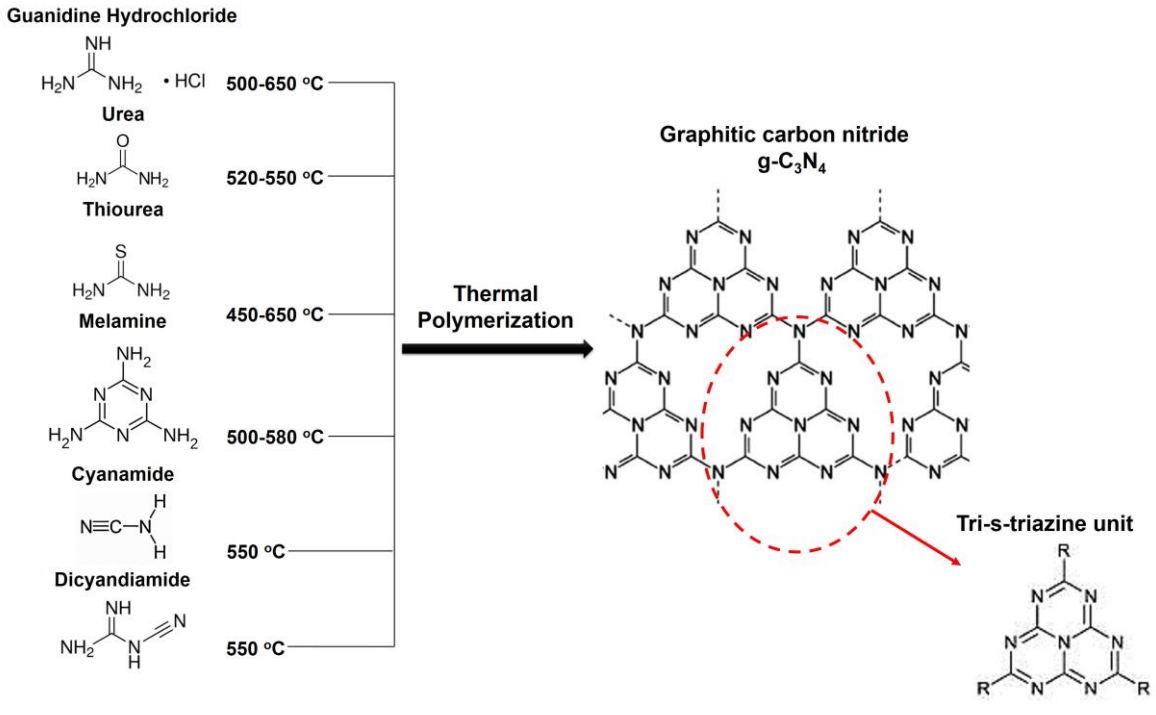

Figure 1.7: Schematic illustration of the methods for the synthesis of g-CN by following thermal polymerization of guanidine hydrochloride, urea, thiourea, melamine, cyanamide, and dicyandiamide.[88]

Moreover, g-CN possesses various surface functional groups, which are desired for many applications including electronic properties, nucleophilic properties, and ability to form H bonds.[89] Especially the presence of basic sites on the surface of g-CN makes it so attractive to serve as a growth platform for uniform dispersion of metal NPs. There are two surface basic sites on the surface of g-CN which are nitrogen sites in the C-N-C ring, labelled as the Lewis basic site, and the primary and/or secondary amine groups (−NH and/or ═NH) on the terminating edges, known as Brönsted basic site as shown in Figure 1.8. The hydrogen atoms on the terminating edges illustrate the incomplete condensation of g-CN and the existence of surface defects, which might be useful for catalytic application.[88]

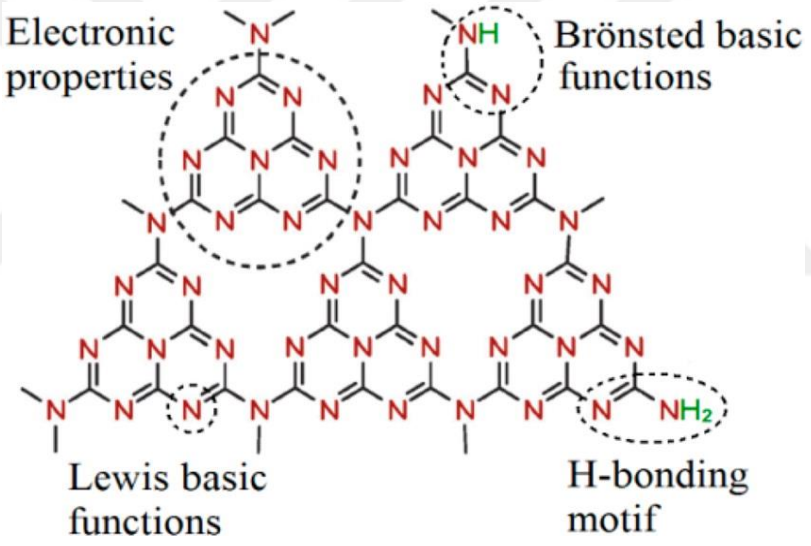

Figure 1.8: Multiple functionalities of g-CN.[88], [90]

For instance, Pérez-Ramírez et al. reported that g-CN was an appropriate substrate to stabilize metal atoms at different size including single atoms, dimers, trimers, clusters or nanoparticles efficiently due to the presence of nitrogen atom rich “six-fold interstices” between tri-s-triazine units.[91] These cavities have strong capability of interaction with incorporated metal atoms due to the significant charge transfer or strong interaction between the metal atoms and the neighboring pyridinic nitrogen atoms, which is also verified by the computational studies.[92], [93] Furthermore, the surface area of g-CN can be enlarged by modifying its structure. For example, mesoporous g-CN (m-g-CN) and exfoliated g-CN nanosheets can be easily synthesized via the use of templates and thermal

treatment, respectively, such that enhanced surface area and porosity of g-CN work together with its functional groups for a better stabilization and dispersion of metal NPs.

Besides all these benefits, g-CN has excellent physicochemical properties such as having unique electronic structure and appropriate band gap (2.7 eV, 454 nm), which make it active under visible light irradiation. The suitable valence band (VB) and conduction band (CB) potentials of g-CN, which are +1.6 eV and -1.1 eV, respectively, are favorable to trigger various redox process such as water splitting, organic transformation reactions, and degradation of organic pollutants. An electron in the VB absorbs a photon of a certain wavelengths, excited to the CB, and eventually moves to the surface of the metal catalyst to initiate reduction reaction. At the same time, a hole formed in the valence band due to the lack of electron moves to the surface to promote oxidation reaction as illustrated in Figure 1.9.

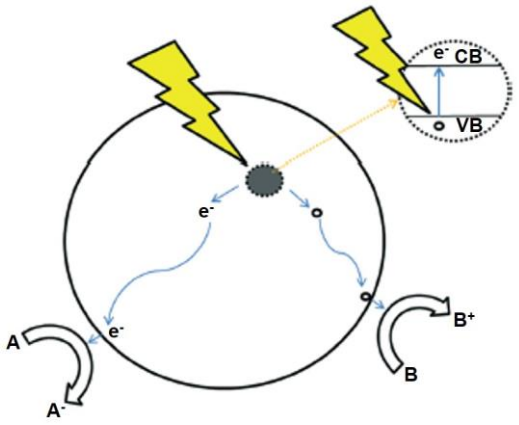

Figure 1.9: The mechanism of oxidation and reduction reactions in a photocatalyst.[94]

Along the continuous charge transition process, the electrons fall from the CB to the VB, into a hole, which result in electron-hole recombination and decrease in photocatalytic activity. The pristine g-CN performs insufficient photocatalytic activity due to its intrinsic drawbacks such as low visible light absorption ability, low electronic conductivity, and high recombination rate of photo generated carriers. Therefore, to increase the separation efficiency of photo generated electrons and holes is one of the principles for the improvement of photocatalytic performance. There are many strategies for enhancing the photocatalytic activity of g-CN under visible light such as morphology optimization to increase number of active sites, sensitization with different sensitizers, doping with different metals/nonmetals, generation of defect/vacancy, and interfacial engineering.

Among them, the interfacial engineering is the one mostly applied to boost photocatalytic activity of g-CN via accelerating electron-hole growth rate and prolonging their lifetime.

1.5.2. Interfacial engineering applied on g-CN

As it is well-known, interfacial engineering is achieved if the interface properties of the bare components match sufficiently depending on their energy band structure or Fermi level. It is obvious that nitrogen functional groups of g-CN can provide binding sites for the metal NPs, making g-CN as an ideal support and stabilizer for metal NPs, such that an effective metal/g-CN interface serving as a charge separator can be built up. Moreover, combining g-CN with a suitable secondary semiconductor to form g-CN based heterojunctions is another extensively studied method under the title of interfacial engineering due to its ability of suppressing charge recombination and enhancing visible light absorption.

1.5.2.1. Construction of metal/g-CN interface

Noble metal NPs are often preferred to be used for the effective interfacial engineering of g-CN due to their high work function. When noble metals are deposited on g-CN, there are two possible phenomena occur at the metal/g-CN interface, known as Schottky barrier and Surface Plasmonic Resonance (SPR), enhancing the overall photocatalytic activity.[95] The band position of g-CN is generally suitable to promote the formation of Schottky heterojunction via loading of noble metal NPs, as the work function of most noble metals is located between the CB and VB of g-CN (Figure 1.10a). Photoexcited electrons flow through the noble metal/g-CN interface until Fermi level equilibrium is reached, resulting in bending of the conduction band and formation of the Schottky barrier at the interface.[96] Through the Schottky barrier, the separation of electrons and holes are accelerated via electron flow occurring only from semiconductor to metal NPs, and then these electrons are captured by metal NPs (Figure 1.10b). In other words, Schottky barrier acts as an effective electron trap such that the irreversible electron flow makes the metal NPs act as an electron sink. The metals having lower work functions compared to semiconductor leads to minor changes in photocatalytic performance. The effectiveness of the Schottky barrier depends on its height that will be higher if the difference between the values of work functions of metal and semiconductor is enlarged. Eventually, the charge separation at the interface is enhanced and lifespan of the electrons is prolonged, which are desired to boost photocatalytic activity.[97]

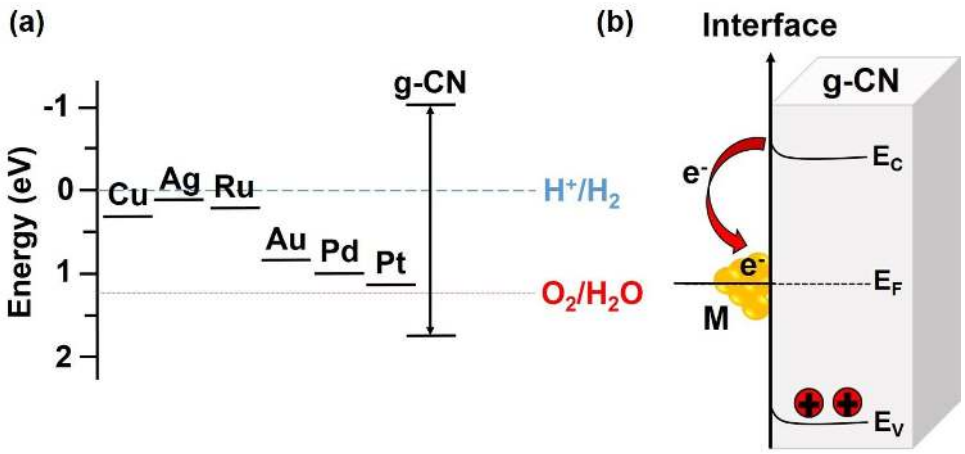

Figure 1.10: (a) Work functions of various metals (M) and band structure of graphitic carbon nitride (data from literature on a potential scale (V) versus NHE, (b) Schematic view of Schottky-type g-CN/M contact (E_F: work function, E_C: conduction band, E_V: valence band).[97], [98]

Another important phenomenon happens at the interface is SPR, which has the ability to create electromagnetic field and improve photocatalytic activity. Surface plasmon resonance is the charge density oscillation and electric field creation at the interface between metal and semiconductor. When the light is illuminated on the plasmonic metal, the change of electron density on each side of the metal occurs, which results in creation of an electric field inside and outside of the metal accordingly. Additionally, a series of charge density oscillations take place through the coulombic restoring forces. Among the mechanisms proposed to explain how the SPR effect contributes to photocatalytic activity, the production of hot electron-holes in the plasmonic metal is the extensively investigated.[94]

According to the hot electron transfer mechanism, the hot electrons produced on the metal are supplied to the conduction band of the semiconductor for the photo reduction reaction under visible light irradiation (Figure 1.11).[99] On the other hand, this mechanism creates a paradox between Schottky barrier and SPR in terms of whether the metal is trapping electrons from conduction band or the metal is supplying electrons to the conduction band. When the Schottky barrier is formed to trap electrons into the metals, hot electron transfer from metal to semiconductor is expected via SPR effect. Simultaneously, the transferred electrons can easily flow back to the metal if Schottky barrier exists. In other words, the electron flow from the semiconductor to the metal is independent of the source of the electrons, whether it comes from VB of the semiconductor or the metal,

if the electrons fall into the CB of semiconductor and the metal is in contact with the semiconductor. It can be concluded that hot electron transfer mechanism is unable to guarantee that all the electrons excited from metal contribute to the photoreduction because they are transferred to the metal afterwards through the Schottky barrier.

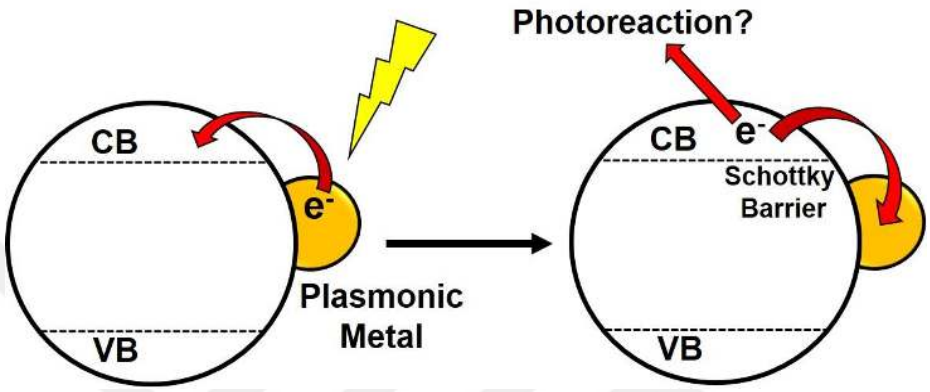

Figure 1.11: Possible pathways of the electron after being transferred from metal to CB of semiconductor.[94]

1.5.2.2. Construction of g-CN/secondary semiconductor heterojunctions

When a secondary semiconductor is combined with g-CN to form heterojunction, photocatalytic performance will be improved due to the enhanced separation of photo generated electrons and holes. Depending on the alignment of the energy bands of secondary semiconductor at the interface, g-CN based heterojunctions are classified as being type-I, type-II, type-III, and Z-scheme (Figure 1.12). In case of type-I heterojunction, the band gap region of g-CN covers both VB and CB of the secondary semiconductor such that all the photo generated electrons and holes in g-CN flow in one direction towards the secondary semiconductor and all charges accumulated in the secondary semiconductor (Figure 1.12a). For this reason, photo-generated electrons and holes are hardly separated, and the recombination is unavoidable. In type-II heterojunction, band edge potentials of both semiconductors are staggered. The photo generated electrons on the CB of g-CN flow to the CB of secondary semiconductor while the holes in VB migrate in opposite direction, from VB of secondary semiconductor to VB of g-CN (Figure 1.12b). Therefore, separation efficiency of the carriers is enhanced along with the elimination of electron-hole recombination.

In type-III heterojunctions, VB and CB of g-CN and secondary semiconductor do not overlap with each other (Figure 1.12c). As a result, the efficient separation of photo-generated electrons and holes cannot be achieved. Finally, Z-scheme heterojunctions have been introduced recently, in which photo-generated electrons in the CB of the secondary semiconductor are transferred to the VB of g-CN, so that photo-generated electrons are in the CB of g-CN and holes are separated. effectively succeeded in the VB of the secondary semiconductor (Figure 1.12d).[100]

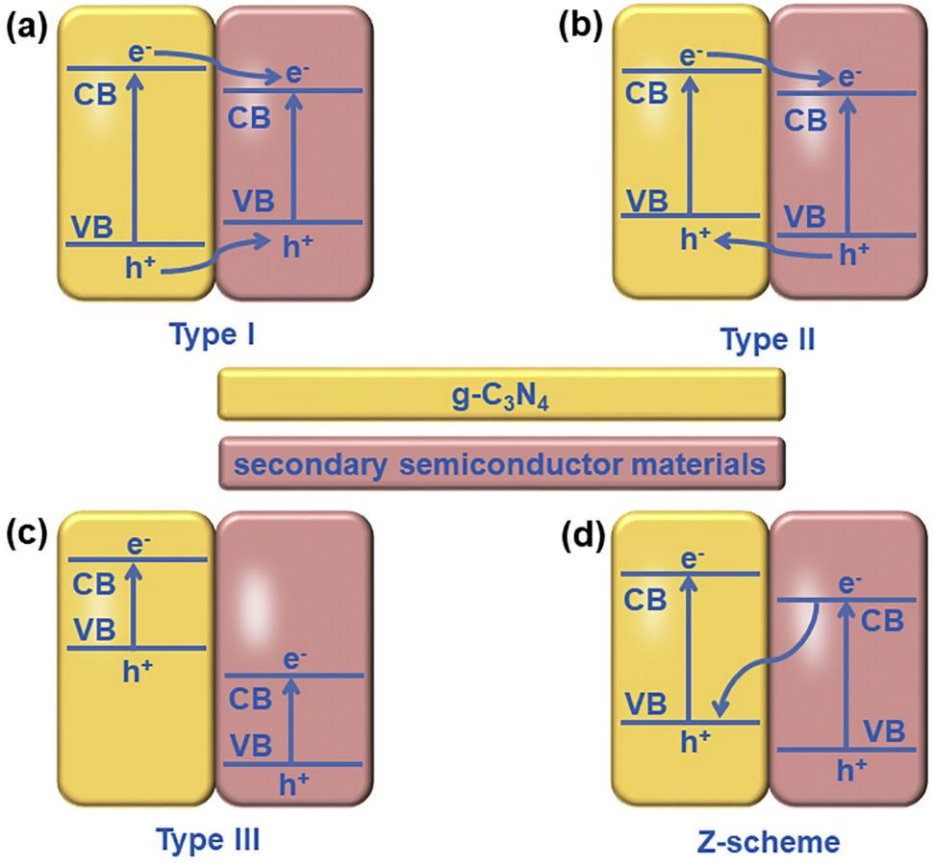

Figure 1.12: Schematic energy band diagram of (a) type-I, (b) type-II, (c) type-III, and (d) Z-scheme heterojunctions built up by g-CN and a secondary semiconductor material.[100]

According to this discussion, type-II and Z-scheme g-CN based heterojunctions are highly desirable in the construction of g-CN based heterojunctions compared to others for the sake of improved separation and life span of charges. The visible light absorption ability of g-CN can also be improved for a better utilization of solar energy, which is in company with other enhancements to boost the overall photocatalytic activity. Besides,

introducing secondary semiconductor does not affect the unique molecular structure of g-CN, and consequently advantage of g-CN as being a stabilizer for the metal NP deposition is still preserved.

There are many types of semiconductors having the appropriate potential energy of VB and CB to form type-II heterojunctions with g-CN, such as wide band gap metal oxides (TiO_2, SnO_2)[101], [102], metal sulfides (CdS, ZnS)[103], [104], and ternary oxides ($BiVO_4$)[105] as shown in Figure 1.13. Although g-CN based type-II heterojunctions are excellent at reducing the recombination rate and enhancing separation efficiency, it suffers from poor reduction/oxidation ability. The reason behind this is that flow of photo generated electrons from the CB of g-CN to the CB of secondary semiconductor, which is positioned at less negative potential value and jumping of holes from VB of secondary semiconductor to VB of g-CN, which is positioned at less positive potential value. In contrary, the g-CN based Z-scheme heterojunctions can retain redox capability of both photo generated electrons and holes, because they are kept at more negative reduction potential value and more positive oxidation potential value, respectively. There are many examples of reported g-CN based Z-scheme heterojunctions including g-CN/TiO_2[106], g-CN/Fe_2O_3[107], g-CN/$CoTiO_3$[108], and g-CN/WO_3[109] serving for both photocatalytic oxidation and reduction reactions such as hydrogen evolution, CO_2 reduction, and degradation of organics with high efficiency. Among them, WO_3 is a very good candidate for the effective construction of Z-scheme g-CN/WO_3 heterojunctions for the photocatalytic HAB due to its matched energy band levels with g-CN along with its oxygen-deficient/non-stoichiometric nature bringing the modified band structure.[110,111] Moreover, as discussed in Section 1.3.2, the interaction between the metal catalyst surface and H atom of AB and the formation of activation species is the prerequisite for hydrogen evolution from AB. In Pt case, even though Pt metal show very good activity to dissociate B-H bond within AB, it is intrinsically inactive in dissociation of O-H bond within water, which is claimed to be RDS.[112] However, some transition metal oxides such as WO_3 exhibits very good potential for facile H_2O dissociation such that if the surface of g-CN based Pt nanocatalyst can be modified with WO_3, a rational design of Pt nanocatalysts, having dual active sites and visible light active sites can be achieved for photocatalytic dehydrogenation of AB.[113]

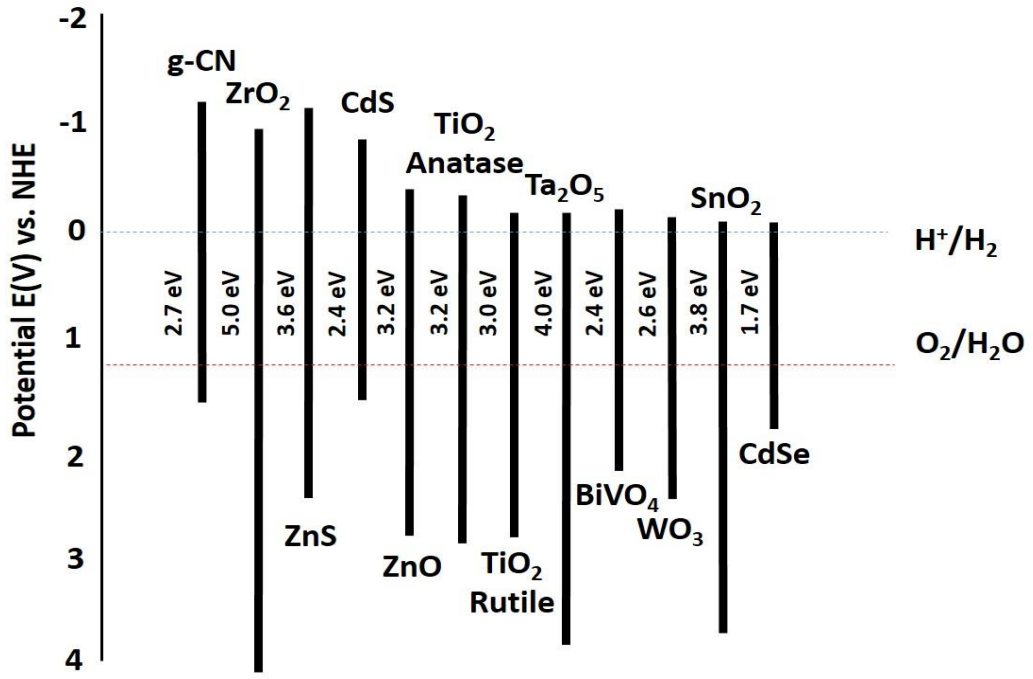

Figure 1.13: Schematic illustration of the band structures and potentials for various semiconductors constructing type-II heterojunction with g-CN.[114]

1.6 Objective and Summary of the thesis

In this thesis, in the light of the discussed concepts and ideas above, it was aimed to develop efficient photo active metal nanocatalysts for H_2 production from the HAB. The suggested metal nanocatalysts consist of transition metal NPs supported on semiconductor 2D materials. Due to its unique capacity to dissociate B-H bond within AB and excellent activity results reported for HAB, Pt NPs having good dispersion, stability and durability were aimed to synthesize. The in-situ synthesis method, which involves impregnating the Pt precursor to the porous support and then reducing it in the catalytic reaction medium, is preferred because it is an easy, time-saving, and cost-effective synthesis method compared to others. However, this method involves a good choice of support material which also should act as a stabilizer due to the absence of stabilizing agents in the reaction medium, otherwise dispersion and stability of Pt NPs is hardly provided. g-CN is found to be very good candidate as a growth platform for the in-situ synthesis of Pt NPs owing to its layered structure, functional group rich surface, easy-to-handle synthesis, easily modified morphology to improve surface area, non-toxicity, and visible light active semiconductor nature. Besides, the work function of Pt NPs is available to construct a Schottky barrier at the interface. It improves the charge separation and lifetime of the electrons, which lead to

electron enrichment of metal surface and more efficient HAB.

In Chapter 2, mesoporous graphitic carbon nitride (m-g-CN), synthesized via silica hard templating method, was used for the in-situ synthesis of m-g-CN/Pt nanocatalysts and concomitant dehydrogenation of AB. The effect of the light and the amount of Pt on the dehydrogenation of AB was examined. Owing to its unique electronic structure and surface functional groups, the stabilizing effect of m-g-CN on impregnated Pt ions were strongly enough to yield high results of activity and reusability. This study is known as the first one coupling the terms of "m-g-CN", "Pt NPs", and "HAB", and makes a contribution to close the gap of "photocatalytic dehydrogenation of AB enhanced via construction of Schottky barrier" in the literature.[115]

In Chapter 3, graphitic carbon nitride (g-CN) obtained via condensation of urea (U-g-CN) in the absence of silica template was reported as being more effective support material compared to m-g-CN for Pt NPs growth and concomitant HAB, which is attributed to its morphological differences and improved photophysical properties such as higher absorption ability, lower band gap, and longer life span of charges compared to those of m-g-CN. Owing the mentioned enhanced abilities of U-g-CN, it was preferred for the aim of further development of Pt based nanocatalysts. For this reason, bimetallic MPt (M: Au, Ag, Cu) NPs of varying compositions were in-situ synthesized. The main reason behind the chosen of Au, Ag, and Cu metals to form MPt bimetallic NPs is that they have strong SPR effect that might contribute to the photocatalytic activity by following any of SPR mechanisms, which is a phenomenon happening at the metal/semiconductor interfaces along with Scottky barrier. Among all synthesized U-g-CN/MPt nanocatalysts, U-g-CN/$Pt_{92}Au_8$ and U-g-CN/$Pt_{85}Au_{15}$ nanocatalysts provided higher activity than U-g-CN/Pt_{100}, and the reasons behind this resultwere further investigated.

In Chapter 4, g-CN/WO_x/Pt heterojunctions were aimed to synthesize and characterize along with the investigation of their photocatalytic activities in HAB. g-CN/WO_x heterojunction composites including different amount of W were synthesized and their photophysical properties were investigated to explain their contribution to catalytic activity in HAB under white light illumination. The obtained characterization results support the formation of amorphous phase WO_x (a-WO_x) substances in multiple oxidation states. Even though it is aimed to obtain g-CN/WO_3 heterojunctions and test their contribution to the photocatalytic HAB, the followed synthesis method, consisting of thermal polymerization of urea in the presence of tungstate salts, directed the research

towards the investigation on g-CN/a-WO_x heterojunctions, which are the heterojunctions taking an important part in the literature of the photocatalysts.

In summary, all the stepwisely developed Pt nanocatalysts in each chapter was to achieve enhancement in photocatalytic activity of Pt NPs for HAB. For this reason, g-CN based heterojunctions were aimed to build up for the in-situ growth of Pt NPs, being highly active in HAB with their electron enriched surfaces. And, this electron enrichment can be achieved with their loading on highly efficient visible-light active g-CN based heterojunctions.

Chapter 2

m-g-CN/Pt NANOCATALYSTS FOR THE HAB

2.1 Introduction

Our initial studies were focused on the synthesis of Pt NPs supported on m-g-CN (m-g-CN/Pt) in which m-g-CN served as a semiconductor support material and stabilizer. m-g-CN/Pt nanocatalysts were synthesized in situ during the hydrolytic dehydrogenation of AB under the visible light irradiation. Additionally, the photocatalytic activity of the in situ generated m-g-CN/Pt nanocatalysts in the hydrolysis of HAB was investigated by performing many experiments on different reaction parameters. The Pt loading effect on the particle size, dispersion, uniformity of particle distributions, and eventually on the photocatalytic activity of m-g-CN/Pt nanocatalysts was investigated in detail. Due to the dual role of m-g-CN as a support material and stabilizer, in situ synthesized Pt NPs showed a good durability and robustness with no additional stabilizer. This study was the first example of the in situ synthesized Pt NPs supported on m-g-CN during the HAB, a promising candidate as a photocatalyst for the hydrogen storage systems involving AB as a solid storage material. The results of this chapter was published as a full paper in ACS Applied Nano Materials (2020, 3 (7), 6836-6846).[115]

2.2 Experimental

2.2.1 Chemicals

Guanidine hydrochloride (GnHCl, 98%), LUDOX HS-40 colloidal silica (40 wt % suspension in H_2O), ammonium hydrogen difluoride (NH_4HF_2, >98 %), chloroplatinic acid hexahydrate ($H_2PtCl_6.6H_2O$, >37.5 % Pt basis, ACS reagent) and ammonia borane (AB, 90%), ethanol absolute (≥ 99.9%), and deionized water (DI, 0.055 $\mu S.cm^{-1}$) are the chemicals and solvents purchased and used as received.[115]

2.2.2 Instrumentation

TEM images were recorded on a HT7700 TEM instrument with dual-mode objective lens (EXALENS) features for the HR-TEM analysis operating at 120 kV. To identify crystalline phases of the synthesized m-g-CN/Pt nanocatalysts, Bruker D2 Phaser X-Ray Diffractometer (XRD) equipped with Cu Kα radiation source (1.5418 Å) and LynxEye detector with 1D mode was operated at step size of 0.012°. Agilent 7700x Inductively Coupled Plasma-Mass

Spectrometer (ICP-MS) was used to detect Pt loading of the nanocatalysts. To prepare samples for the ICP-MS analysis, the powder nanocatalysts were digested in 10 mL of aqua regia acid solution by Start D Milestone Microwave Digestion system. And then, the collected solution was diluted with 2 v/v% HNO_3 blank solution. Thermo K-Alpha X-Ray Photoelectron Spectrometer (XPS) equipped with Al−Kα source was operated to get useful chemical state information from the surface of nanocatalysts. UV-Vis Diffuse reflectance spectroscopy data was collected by using Shimadzu UV-3600-UV-VIS-NIR spectrometer. Kubelka-Munk function was used to transform reflectance data to absorbance. Subsequently, optical band gap energy was determined according to Tauc' method. Fourier transform infrared (FTIR) spectroscopy technique is followed to detect any change in surface functional groups of m-g-CN with the addition of Pt NPs with Thermo Scientific iS10 FT-IR instrument. Photoluminescence (PL) emission data was collected with Agilent Cary Eclipse PL spectrophotometer using an excitation source of 350 nm. Time-resolved spectroscopy measurement was performed with Edinburgh Instruments FLS1000 Spectrometer using a 377 nm excitation source.[115]

2.2.3 Synthesis of mesoporous graphitic carbon nitride (m-g-CN)

A well-established hard-templating method was followed for the synthesis of m-g-CN.[116] The method includes the thermal poly condensation of guanidine hydrochloride along with LUDOX HS-40 colloidal silica. Here, the colloidal silica was used as a template for the formation of mesopores in the structure. The 4 g of GnHCl dissolved in 4 mL DI water were added slowly and dropwise to 10 mL of silica suspension while stirring vigorously. The solution was stirred overnight at 50 ^oC to let the water in the solution evaporate, and the solute left behind was white powder. Next, the obtained powder was put into a quartz holder covered with a lid and placed in a tube furnace. It was heated to 550 ^oC along 2 h, kept at this temperature for 2 h and let to be cooled down naturally under a gentle argon gas flow. The product obtained was dark yellow. The silica template was removed by etching the yellow powder in 200 mL of 4M NH_4HF_2 solution via stirring along 2 days. After 2 days of stirring, the resulting solid product was separated by centrifugation at 9000 rpm for 10 min, washed with DI water twice and eventually with ethanol by applying the same centrifugation procedure. The final product was dried in vacuum furnace at 50 ^oC.[115]

2.2.4 Synthesis of m-g-CN/Pt(IV) Composites

100 mg of m-g-CN was dispersed in absolute ethanol by sonication in ultrasonic bath for 1h. A certain amount of $H_2PtCl_6.6H_2O$ salt was dissolved in absolute ethanol and added dropwise into the m-g-CN solution prior to on-going sonication along 3 h. The resultant mixture was allowed to stir overnight at room temperature. Finally, the m-g-CN/Pt(IV) composite powder was precipitated by centrifugation at 9000 rpm for 10 min and dried under vacuum at 50 ^oC.[115]

2.2.5 In-situ syntesis of m-g-CN/Pt Nanocatalysts and the concomitant HAB

10 mg of m-g-CN/Pt(IV) composites in 8 mL of DI water was sonicated via an ultrasonic bath for 1 h. The dispersion was carried into the two-necked jacketed vessel connected to a circulating water bath to keep the solution at constant temperature (25 ± 0.5 ^oC) and the vessel was closed by a lid. As a light source, Philips 150 W lamp (Master Color CDM-T 150 W/942, 340-800 nm range) was used. The lamp, magnetic stirrer and reaction vessel were placed in a mirror box. The light source caused to only 1-1.5 ^oC temperature rise of the reaction solution in the first 10 min. The temperature of the solution did not continue to raise further as the circulating water bath adjusted to 25 ^oC was continuously used. Subsequently, 34.3 mg AB (1 mmol) dissolved in 2 mL of H_2O was injected into the solution, and the hydrogen generation versus time was started to be tracked simultaneously via water-filled burette apparatus, shown in Figure 2.1.[115]

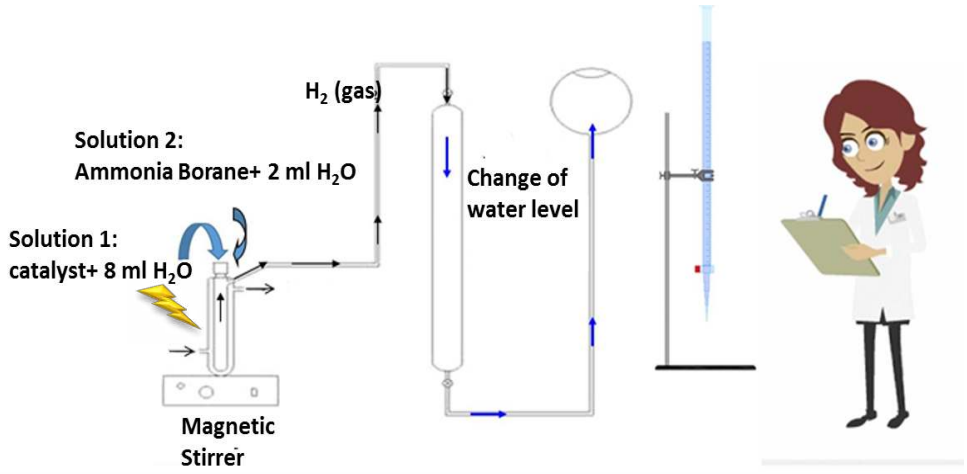

Figure 2.1: The schematic representation of the water-filled burette system (water displacement method) used for the H_2 gas generation.

The displacement of water level in time was noted and the generated H_2 gas was calculated. The resulting m-g-CN/Pt nanocatalysts were brown in color. They were washed with 4:1 water/ ethanol mixture twice via centrifugation at 9000 rpm along 10 min and dried in vacuum furnace at 50 °C overnight. All synthesized nanocomposites and nanocatalysts including different amount of Pt were kept for further characterization. All the synthesis process is summarized in Figure 2.2.[115]

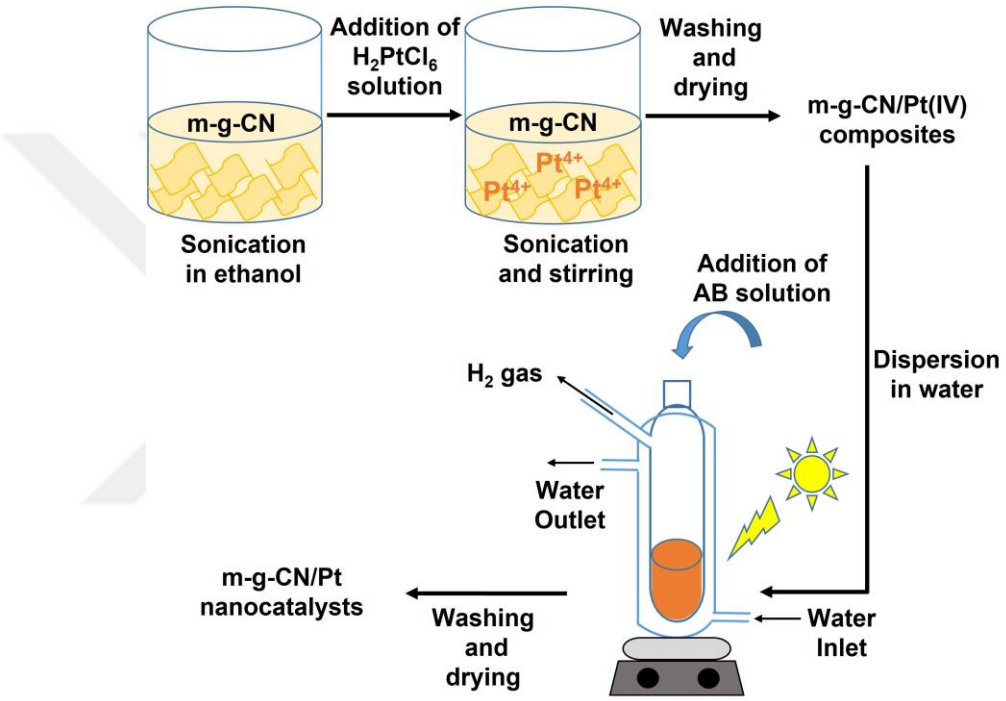

Figure 2.2: Scheme for the synthesis of m-g-CN/Pt(IV) nanocomposites and m-g-CN/Pt nanocatalysts.[115]

2.3 Results and Discussion

The Pt content of m-g-CN/Pt nanocomposites was determined by using ICP-MS measurements. The theoretical Pt loadings on m-g-CN in terms of weight percentage (wt%) were compared with the results obtained by ICP-MS. As shown in Table 2.1, there is a noticeable difference between the theoretical and experimental (determined from ICP-MS) Pt loadings and the difference gets higher as the theoretical loading percentage is increased. The reason might be the lost some amount of Pt ions that are not interacting with the functional groups of m-g-CN during the washing process. Of course, we used the Pt loading determined by the ICP-MS analysis for the further studies.[115]

Table 2.1: Pt loading weight percent (wt %) of m-g-CN/Pt(IV) composites theoretically and by ICP-MS measurement.[115]

Pt loading % (theoretically)	Pt loading % (ICP-MS)
10	5.94
5	3.82
2.5	2.08
1.25	1.16

TEM images of m-g-CN/Pt nanocatalysts including different amount of Pt was shown in Figure 2.3 and Figure A1 (see Appendix). According to TEM images, highly dispersed small Pt NPs having average particle size of less than 6 nm were formed on m-g-CN. The average particle size of the Pt NPs was calculated to be 5.9 nm, 3.5 nm, 3.8 nm, and 5.9 nm for the 5.94, 3.82, 2.08, and 1.16 wt% Pt loaded m-g-CN/Pt nanocatalysts, respectively. Even though average particle size of Pt NPs was almost similar for all Pt loadings, the dispersion of the NPs showed quite difference as the Pt amount varies. In the case of 5.94 wt% Pt loaded m-g-CN/Pt nanocatalyst, agglomerates and large particles were observable which were not seen in the TEM images of the nanocatalyst with other Pt loadings. The m-g-CN/Pt nanocatalyst with 3.82 wt% Pt displayed the most uniform particle size distribution and the smallest average particle size (3.5 nm). Compared to the 3.82 wt% Pt loaded nanaocatalysts, TEM images of 2.08 wt% Pt loaded one showed Pt NPs widely apart from each other, attributed to the presence of almost 2-fold less amount of Pt impregnated into m-g-CN. The deviation from the pattern became more strict in 1.16 wt% Pt loaded nanocatalyst with the higher average size and non-uniform size distribution.[115]

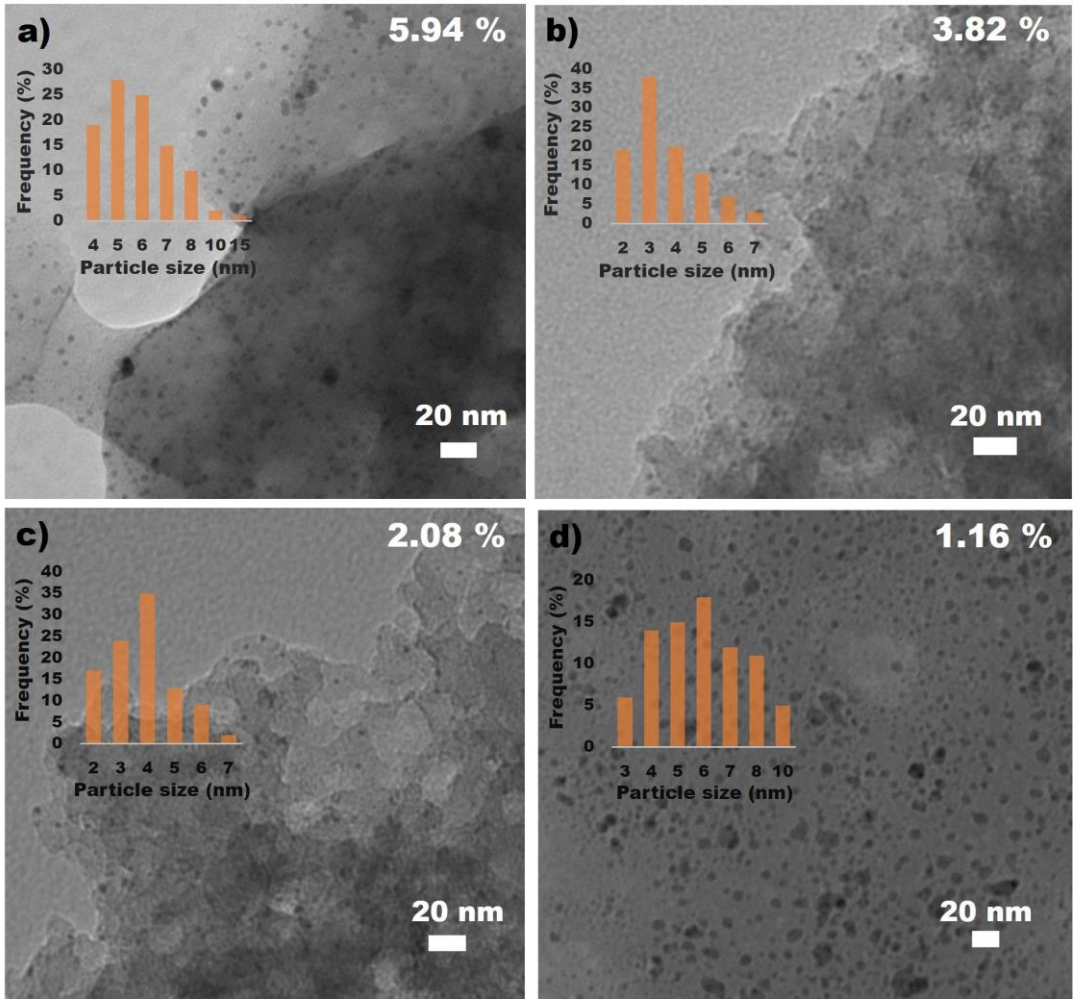

Figure 2.3: TEM images of m-g-CN/Pt nanocatalysts with different Pt loading ratios (a) 5.94 wt%, (b) 3.82 wt%, (c) 2.08 wt%, and (d) 1.16 wt%. The inset graphs show particle size distribution of Pt NPs.[115]

The crystal structure of m-g-CN and m-g-CN/Pt nanocatalysts were investigated by XRD and the recorded XRD patterns are shown in Figure 2.4. Two major peaks of m-g-CN were observable at $2\theta = 13.2°$ and 27.5°, which were attributed to (100) and (002) planes corresponding to the distance between the intralayer replicating tri-s-triazine units and the interlayer distance of m-g-CN, respectively (JCPDS card no: 87-1526).[116], [117] These planes were also apparent in the XRD patterns of m-g-CN/Pt nanocatalysts (5.94 wt%, 3.82 wt%, 2.08 wt% Pt loaded) without any shifting in their peak positions. For the m-g-CN/Pt nanocatalysts, three diffraction peaks observable at 2θ =39.6°, 46.7°, and 64.5° were belong to the (111), (200), and (220) planes of face centered cubic (fcc) Pt (JCPDS card no: 88−2343), respectively.[81], [118]

These assigned peaks were very broad due to the small particle size of Pt NPs. The less intensive peaks of fcc-Pt, which are observable at 2θ = 46.7° and 64.5°, were both almost detectable only in the pattern of 5.94 wt% Pt loaded nanocatalyst. When the Pt loading amount diminished from 5.94 to 3.82 wt%, the intensity of the peaks located at 2θ =39.6° and 46.7° became less and the peak corresponding to (220) plane was disappeared. Besides, all the peaks of fcc Pt, even the most intensive one, are missing in the XRD pattern of 2.08 wt% Pt loaded nanocatalyst. The same pattern was also obtained for 1.16 wt% Pt loaded one such that it was not preferred to be illustrated. Scherrer equation was employed on the (111) plane of fcc Pt to calculate nano crystallite size of m-g-CN/Pt (5.94 wt% Pt) and m-g-CN/Pt (3.82 wt% Pt) nanocatalysts. For the 5.94 wt% Pt loaded one, the particle size was calculated to be 3.35 nm (2θ= 39.8 degree & FWMH= 2.52), with deviation of 2.5 nm from the one calculated based on TEM image (5.9 nm). For the 3.82 wt% case, it was found to be 3.53 nm (2θ= 39.8 degree & FWMH= 2.39), which is in good agreement with the average particle size calculated from TEM image (3.5 nm).[115]

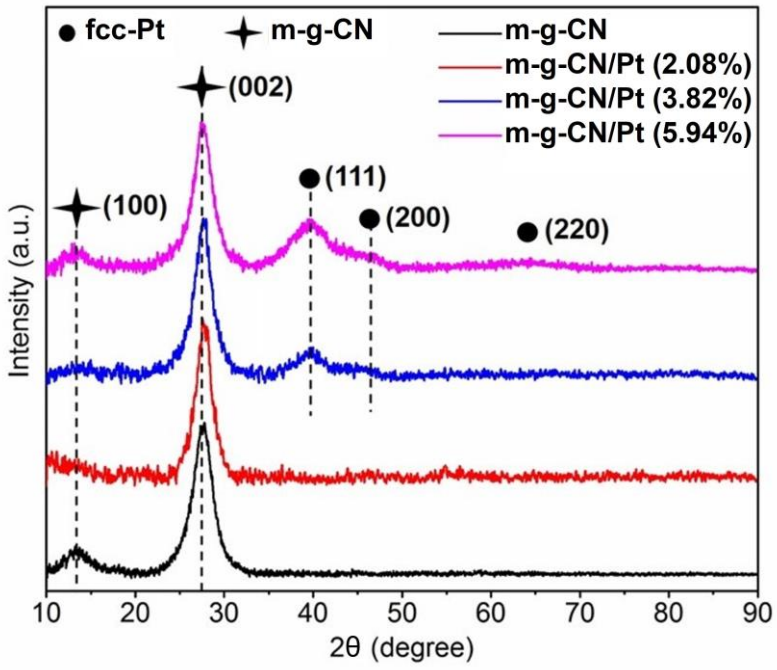

Figure 2.4: XRD patterns of m-g-CN and m-g-CN/Pt nanocatalysts containing different amount of Pt (2.08 wt%, 3.82 wt%, 5.94 wt%).[115]

The chemical states of the elements present on the surface of sample m-g-CN/Pt (3.82 wt% Pt) were investigated by X-ray photoelectron spectroscopy (XPS). The XPS survey spectra confirmed the existence of all constituent elements which are C, N, O, and

Pt (Figure A2, see appendix). The high resolution XPS spectra recorded for the C 1s, N 1s, O 1s and Pt 4f regions were studied. In C 1s spectra, three major peaks at binding energies (BEs) of 284.5, 286.1, and 288.1 eV were observed. These peaks were attributed to C atoms of the C−C or C = C functionalities, sp^2-hybridized s-triazine aromatic ring C coordinated to terminal amino groups (N−C(−NH_2) = N), and s-triazine aromatic ring C ((-N-)$_2$-C = N), respectively (Figure 2.5a).[115], [116] The high resolution XPS spectra of N 1s region displayed three major peaks at BEs of 398.7 eV, 400.3 and 401.3 eV, readily assigned to the sp^2-hybridized s-triazine aromatic ring N (C = N−C), sp^3-hybridized nitrogen which is connecting s-triazine rings (N(-C−)$_3$), and nitrogen of terminal amino groups (−C−NH_2), respectively, as shown in Figure 2.5b.[115], [119] To analyze whether there was a formation of any oxygen species, the high resolution XPS spectra of O 1s core-level was also studied. The peak at 532.5 eV demonstrated the presence of ionization due to the weakly adsorbed oxygen species on m-g-CN (Figure 2.5c).[120] There was no strong evidence for the formation of PtO species, because no peak labelled in the low energy side of the O 1s binding energy scale (527.7 eV- 530.5 eV) corresponding to oxygen ions with a "2-" formal charge.[121], [122] The high-resolution XPS spectra of Pt 4f region was deconvoluted to the doublet pairs, which are at BEs of 71.2 eV/ 74.6 eV (doublet 1) and 72.9 eV/76.3 eV (doublet 2), indicating the presence of Pt (0) and Pt (II), together with the entire reduction of Pt (IV) ions (Figure 2.5d).[115],[123] Due to the presence of Pt (II) ions, the complete formation of Pt (0) NPs were not succeeded.[115]

Incomplete reduction of Pt (II) ions was also verified by some other evidence. Firstly, the nanocomposite (m-g-CN/Pt(IV) (3.82 wt% Pt)) was reduced by sodium borohydride (SB) instead of AB by following the same reaction conditions. The Pt $4f_{7/2}$ peak intensity ratio of Pt (II) to Pt (0) was considerably smaller than that of the one reduced by AB, as shown in Figure 2.6. Since SB has stronger reducing ability than AB, less amount of Pt (II) ions remained in the SB reduced m-g-CN/Pt nanocatalysts.[115]

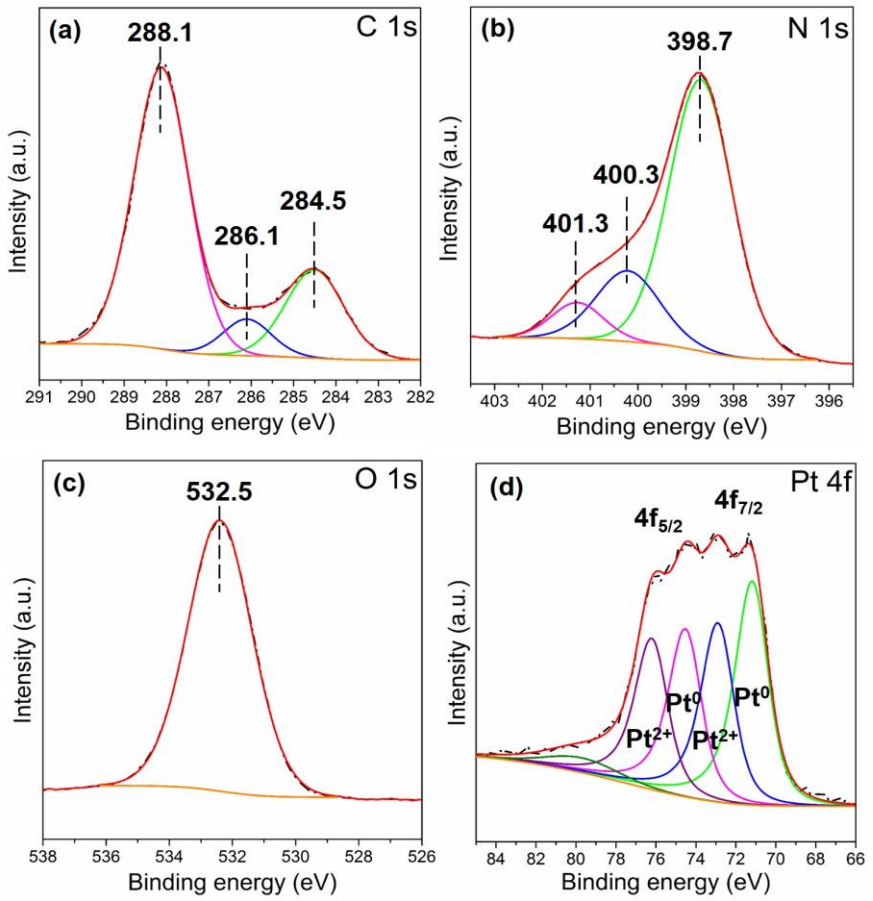

Figure 2.5: HR-XPS (a) C 1s, (b) N 1s, (c) O 1s, (d) Pt 4f spectra of m-g-CN/Pt (3.82 wt% Pt) nanocatalysts.[115]

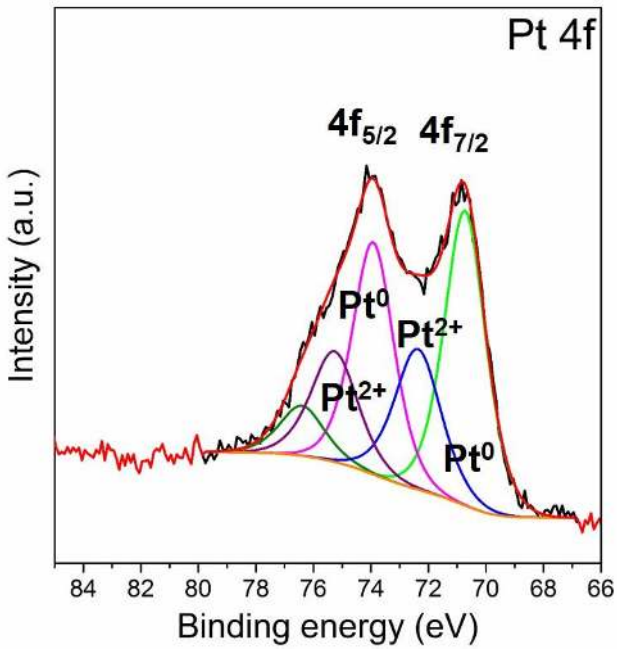

Figure 2.6: HR-XPS Pt 4f spectra of m-g-CN/Pt (3.82 wt% Pt) nanocatalysts reduced by SB instead of AB.[115]

Secondly, Pt $4f_{7/2}$ peak intensity ratio of Pt (II) to Pt (0) decreased after the 10^{th} run of reusability test involving 10 times reduction of m-g-CN/Pt(IV) (3.82 wt% Pt) nanocomposite during the HAB, which resulted in the formation of more Pt(0), as illustrated in Figure 2.7a. Finally, the role of support material was tested by using reduced graphene oxide (r-GO) instead of m-g-CN by following the same reaction conditions. According to HR-XPS spectra of Pt 4f region, all Pt (IV) ions supported on r-GO were reduced to Pt (0) by HAB for once (Figure 2.7b). On the other hand, it was not possible to achieve the complete reduction of Pt (IV) ions supported on m-g-CN even after the t10^{th} run. These results clearly supported that there was an interaction between the m-g-CN and incorporated $[PtCl_6]^{2-}$ ions leading to the formation of stable Pt complexes such that the reduction of Pt ions became difficult.[115]

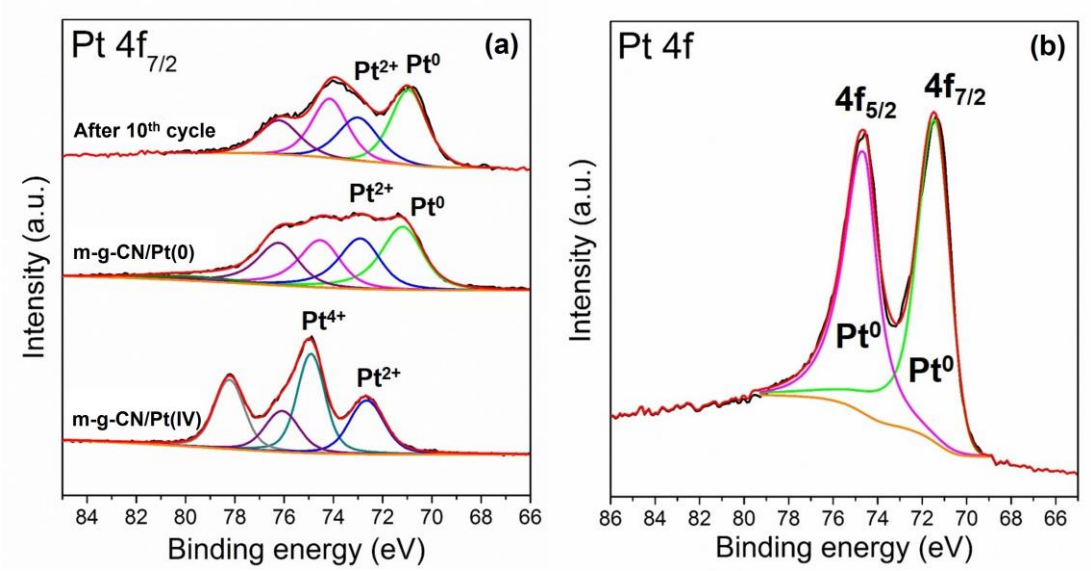

Figure 2.7: (a) Pt $4f_{7/2}$ HR-XPS spectra of m-g-CN/Pt (3.82 wt% Pt) nanocomposites before AB dehydrogenation (m-g-CN/Pt(IV)), after AB dehydrogenation (m-g-CN/Pt), and after 10^{th} run reusability test, (b) Pt 4f HR-XPS spectra of r-GO/Pt nanocatalysts reduced by AB.[115]

We thought that the surface nitrogen functional groups of m-g-CN might be involved in the reduction of Pt(IV) to Pt(II) via substitution of two Cl^- ions in the coordination sphere of the $[PtCl_6]^{2-}$ complex ion.[115], [124] To understand the interaction between the Pt and nitrogen functional groups of m-g-CN, XPS spectra was further investigated. Figure 2.8 shows high-resolution XPS spectra of N 1s region of m-g-CN, m-g-CN/Pt(IV) (3.82

wt% Pt) nanocatalysts. The N 1s peaks of m-g-CN/Pt(IV) composites and m-g-CN/Pt nanocatalysts show a clear shift to the higher binding energy compared to those of pristine m-g-CN. This result indicates that nitrogen functional groups of m-g-CN is responsible to interact with incorporated Pt ions or in situ generated NPs via electron donation.[115]

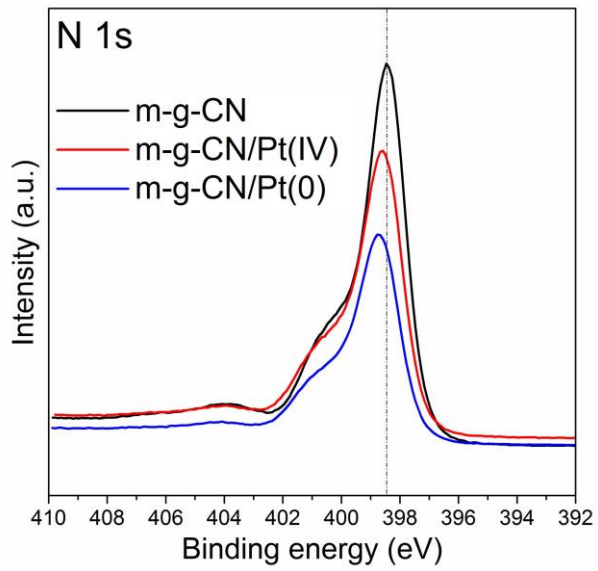

Figure 2.8: HR-XPS spectra of N1s region of m-g-CN, m-g-CN/Pt(IV) composites and m-g-CN/Pt nanocatalysts (3.82 wt% Pt).[115]

Next, N 1s spectra shown in the Figure 2.8 were deconvoluted into three peaks (Figure 2.9a). N atoms in different functional groups were circled on the structure of m-g-CN with the same color of their corresponding N 1s features as illustrated in Figure 2.9b. Moreover, the BE values of all three peaks for three samples were written in Table 2.2. According to the BEs of these peaks, the most intense peak at BE of 398.5 eV, attributing to the s-triazine aromatic ring nitrogen, was the most responsible one to interact with Pt ions or Pt NPs due to the most pronounced shifting value (0.21 eV) compared to other two peaks (0.11 eV).[115], [125] However, it does not mean that there is no interaction between other N atoms with Pt ions or Pt NPs.

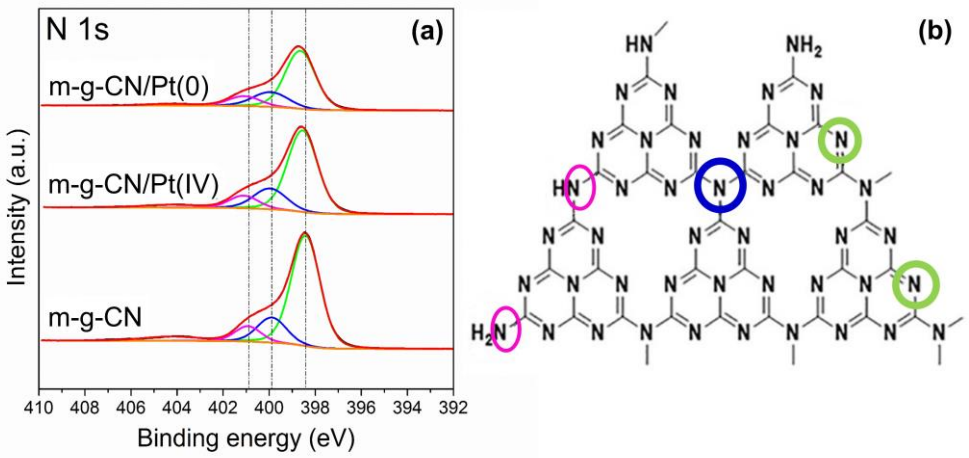

Figure 2.9: (a) N 1s HR-XPS spectra of m-g-CN, m-g-CN/Pt(IV) nanocomposites, and m-g-CN/Pt nanocatalysts; (b) m-g-CN structure on which N atoms are circled with the same color corresponding to each deconvoluted peak in (a).[115]

Table 2.2: The corresponding binding energy values of each peak shown in Figure 2.9.[115]

N groups	m-g-CN	m-g-CN/Pt(IV)	m-g-CN/Pt
C=N-C	398.47	398.58	398.68
N(-C-)$_3$	399.87	399.98	399.98
–C–NH$_2$	400.97	401.08	401.08

FTIR measurements were carried out to investigate the functional groups of pristine m-g-CN and m-g-CN/Pt nanocatalysts with different Pt loadings. According to FTIR spectrum of m-g-CN shown in the Figure 2.10, m-g-CN has many nitrogen functional groups. The broad band at 3000-3500 cm^{-1} was ascribed to the hydrogenated N atoms (-NH, -NH$_2$) of terminal groups. A weak shoulder at ~3500 cm^{-1} was assigned to the O–H stretching modes due to the adsorbed water molecules on the surface. The peak at 807 cm^{-1} was belong to out-of-plane ring bending mode of C–N heterocycles. And finally, the peaks at 1621, 1568, 1410, 1313, and 1235 cm^{-1} were associated with C–N stretching modes in s-triazine aromatic ring. These all-mentioned peaks illustrates the successful synthesis of m-g-CN. And finally, the peak at 2180 cm^{-1} can be attributed to cyano groups (-C ≡ N) located at the defect sites of m-g-CN.[115]

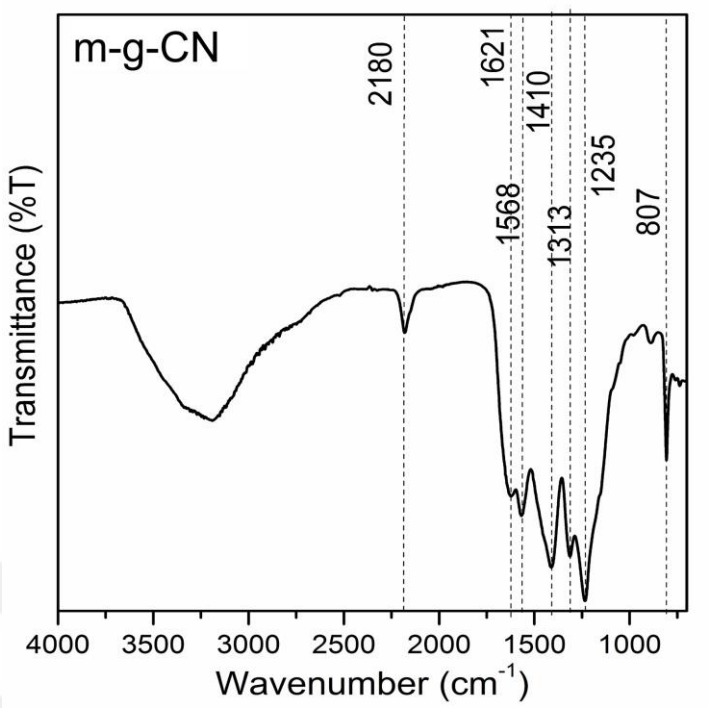

Figure 2.10: FTIR spectra of pristine m-g-CN.

The differences in the functional groups of m-g-CN/Pt nanocatalysts were also investigated. All the above-mentioned functional groups are also observable in the FTIR spectrum of m-g-CN/Pt nanocatalysts with some minor differences (Figure 2.11). The peaks at 1235 and 1313 cm^{-1} shifted to the higher frequency values which indicates the role of C−N groups in s-triazine units for the stabilization of Pt NPs (Figure 2.9b).[62] This result agrees with the conclusion obtained by the XPS measurement. The small shifts observed both in FTIR peak (ca. 4 cm^{-1}) and in N 1s XPS spectrum (0.21 eV) might not seem a strong evidence for the interaction of metal sites with s-triazine units of m-g-CN, but considering the low Pt loadings (less than 6% for each nanocatalyst), these results make sense because such a low Pt loading is not effective to cause a pronounced shift in the XPS or IR spectrum.[115]

Absorption behavior of m-g-CN and m-g-CN/Pt nanocatalysts was analyzed by performing UV−vis diffuse reflectance spectroscopy (UV−vis DRS). The measured reflectance spectra were transformed to the corresponding absorption spectra as shown in Figure 2.12a by applying the Kubelka–Munk function.[126] Figure 2.12b shows the DRS spectra of m-g-CN and m-g-CN/Pt (indirect band gap semiconductors) transformed according to Tauc method, which was plotted against the photon energy (hν) and called Tauc plot.[127] Here, the observed linear region showing the increase of light absorption with the increase of energy is the typical feature of semiconductor materials. The

intersection point of the linear fit on the x-axis gives the estimate value of the band gap energy (Eg), which were calculated as 2.79 eV and 2.84 eV for m-g-CN and m-g-CN/Pt (3.82 wt% Pt) nanocatalysts, respectively. It is concluded that m-g-CN/Pt (3.82 wt% Pt) nanocatalysts represents higher absorption ability with a lower band gap value compared to that of m-g-CN.[115]

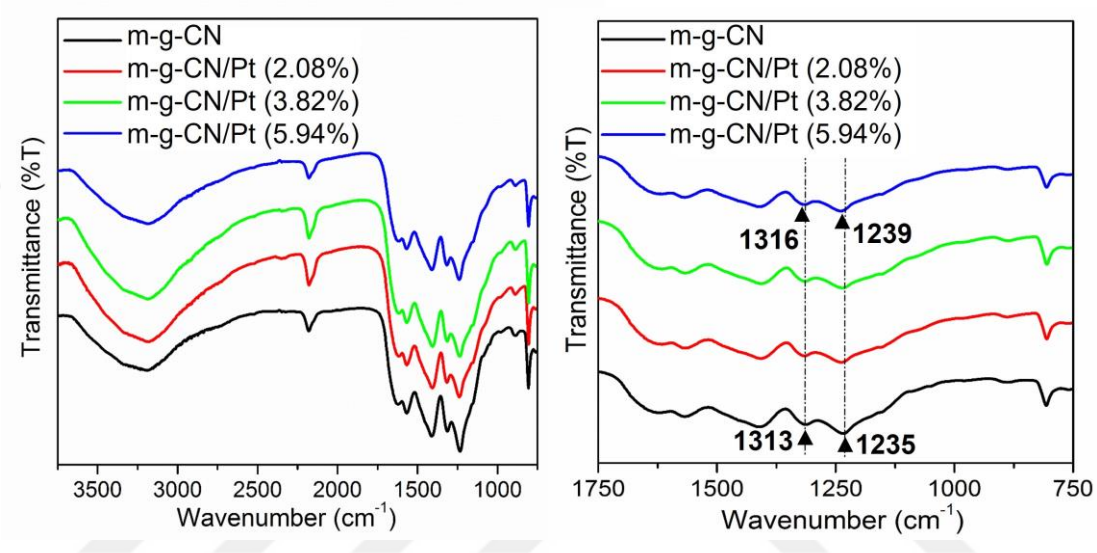

Figure 2.11: FTIR spectra of pristine m-g-CN, m-g-CN/Pt (2.08 wt% Pt), m-g-CN/Pt (3.82 wt% Pt), and m-g-CN/Pt (5.94 wt% Pt) nanocatalysts.[115]

Photoluminescence (PL) and time-resolved emission spectroscopy (TRES) techniques were followed for further investigation of optical properties of m-g-CN and m-g-CN/Pt nanocatalysts. Due to the formation of Schottky barrier between m-g-CN and Pt NPs, the transfer of electron from m-g-CN to Pt was promoted and back migration of electrons from m-g-CN to Pt was prevented. Therefore, recombination rate of the electron-hole pairs decreased in m-g-CN/Pt nanocatalysts, resulted in decreasing of emission intensity compared to pristine m-g-CN (Figure 2.12c). Besides, average lifetime of the photo-generated charges was healed due to the observed increase of average lifetime value from 5.25 ns to 6.20 ns with the addition of Pt NPs (Figure 2.12d). As a conclusion, presence of Pt NPs supported on m-g-CN leaded to the creation of Schottky barrier which inhibited the recombination of electron-hole pairs along with improving the average lifetime of charges, and finally resulted in enhanced photocatalytic activity.[128], [129]

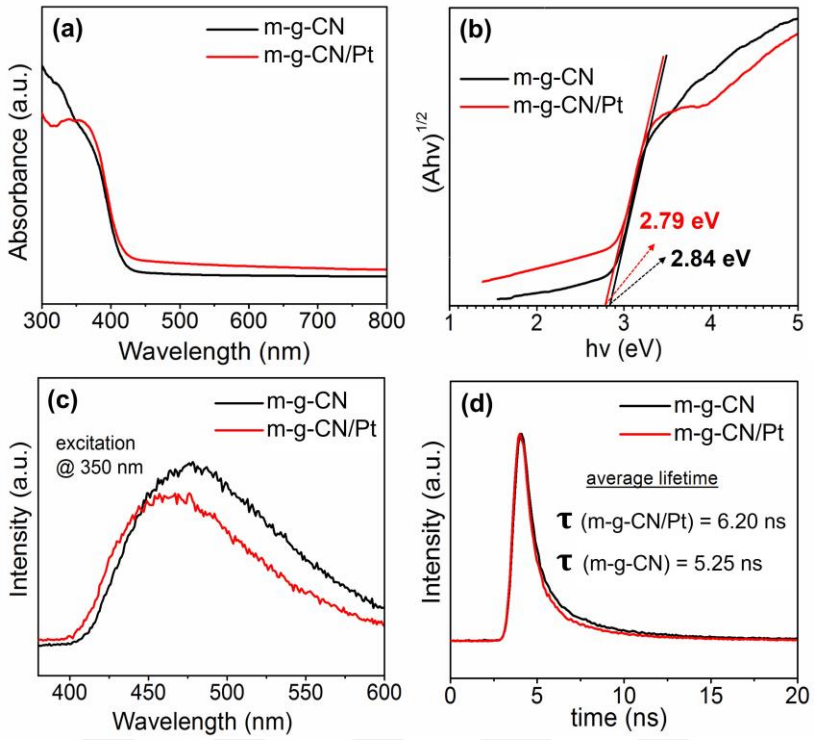

Figure 2.12: (a) UV−vis diffuse reflectance spectra, (b) Tauc plot, (c) PL spectra, and (d) time-resolved emission spectra of m-g-CN and m-g-CN/Pt (3.82 wt% Pt) nanocatalysts.[115]

After the detailed characterization of m-g-CN and m-g-CN/Pt nanocatalysts, the catalytic activity of m-g-CN/Pt nanocatalysts in the HAB was studied at room temperature. Since m-g-CN/Pt nanocatalysts were proved to be a Schottky type photocatalysts, the effect of light on the catalytic HAB was initially studied. As shown in Figure 2.13a, the molar amount of produced H_2 (mmol) versus time (min) was plotted for both in dark and under visible light conditions. All represented H_2 production rate values were calculated from the linear portion of the graphs and small variation in total volume of produced hydrogen gas was attributed to the personal mistakes experienced during weighing AB or reading error from the inverse-burette system. In addition, hydrogen evolution curves had a sigmoidal shape indicating the formation of Pt NPs by following a autocatalytic growth mechanism from the reduction of Pt (IV) and Pt (II) ions during the HAB (Figure 2.13a).[115], [130]–[132] Both curves (dark and light) showed the same sigmoidal pattern, which were similar to the studies in literature showing hydrogen evolution curves under both conditions (dark and light).

The 2.25-fold increment in H_2 production rate was observed under white-light illumination compared to that of in dark. This result clearly proved that m-g-CN/Pt nanocatalysts acted as Schottky-type photocatalysts in the HAB. The enhancement in catalytic activity under white light illumination was explained by a proposed reaction mechanism as illustrated in Figure 2.13b. Here, the valence band (VB) and conduction band (CB) energies of m-g-CN was known to be 1.75 eV and −1.05 eV, respectively and the work function of Pt was located between the VB and CB of m-g-CN.[97], [129] Upon the irradiation of m-g-CN/Pt nanocatalyst, the electrons and holes are generated in the CB and VB of m-g-CN. The excited electrons in the CB moved to the d-band of Pt which had a lower energy than CB of m-g-CN through the interface built between m-g-CN and Pt NPs. And finally, Schottky barrier was formed at the interface, assisting the suppression of charge recombination and promotion of charge separation. Hence, electron enrichment in the active sites of Pt NPs facilitates the hydrolytic dehydrogenation of AB to a certain extent.[115], [133], [134] It might be proposed that the enhancement in activity was due to the light-exposure that creates photothermal process. Firstly, it should be noted that all the photocatalytic hydrolysis reactions were performed in a jacketed reactor that is connected to a circulating constant temperature water-bath. Therefore, the temperature was kept constant well during the entire catalytic reactions. To clarify the point that enhancement in activity was photocatalytic rather than photothermal, a temperature-change control experiment was performed during a typical photocatalytic HAB. In this experiment, the change in temperature of the solution was measured by a probe thermometer inserted into the jacketed reactor. Firstly, the temperature of the circulation system was adjusted to 25 ± 0.5 ^{o}C. Then, the reactor was illuminated by white-light and the variation of temperature versus time is measured. After 10 min irradiation, the reaction temperature elevated by only 1-1.5 ^{o}C during the entire experiment. This negligible temperature elevation might be due to either light-exposure that created photothermal process as it might be proposed or exothermic nature of the HAB.[135], [136] Moreover, it should be better to compare both data depicted by Figure 2.13a and Figure 2.17, which shows the rate increase due to the incorporation of light to the system and the rate increase due to change of temperature from 298 K to 303 K. The enhancement in rate were found to be 2.25-fold and 1.28-fold, respectively, which provides compelling evidence for the existence of photocatalysis rather than photothermal process.

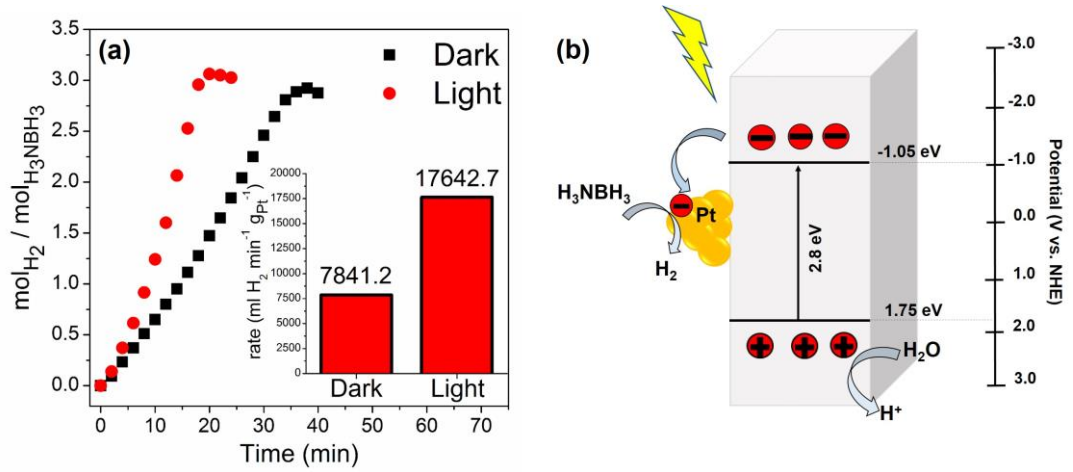

Figure 2.13: (a) Time versus mol H_2/mol H_3NBH_3 plots for the m-g-CN/Pt (2.95 wt% Pt) catalyzed HAB conducted in the dark and under white-light irradiation (inset: H_2 production rate graphs for each condition), (b) Mechanism proposed for the HAB in the presence of m-g-CN/Pt nanocatalysts under white light irradiation.[115]

Next, the effect of Pt loading amount on the photocatalytic activity of m-g-CN/Pt nanocatalysts in the HAB was studied (Figure 2.14). The maximum hydrogen production rate of 31.5 L H_2 g_{Pt}^{-1} min^{-1} was achieved with the largest amount of Pt loaded m-g-CN/Pt nanocatalysts (5.94 wt% Pt), since greater amount of dispersed Pt NPs served as electron donor cites for the decomposition of AB. Even though 5.94 wt% Pt loaded m-g-CN/Pt nanocatalysts gave the highest rate, it was not practical and economical for the catalytic applications due to the significant amount of Pt loss in its production process. The gap between theoretical and experimental Pt loading amount was getting bigger when the theoretical Pt loading was increased so that loss of Pt reached up to 40% in the production process of m-g-CN/Pt (5.94 wt% Pt) nanocatalysts. Therefore, it was decided to prefer 3.82 wt% Pt loaded m-g-CN/Pt nanocatalysts, exhibited the second-best hydrogen production rate of 23.3 L H_2 g_{Pt}^{-1} min^{-1} together with much less loss of Pt in the production step, for the further investigations.

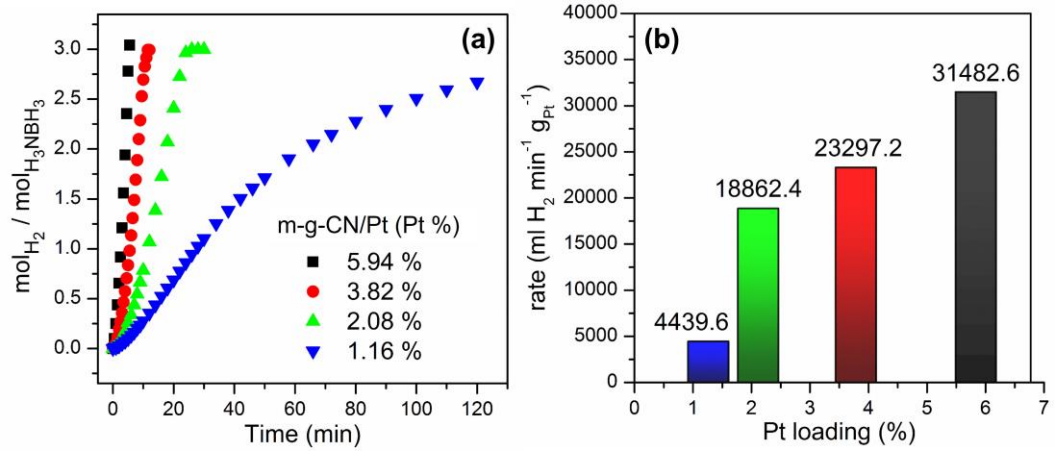

Figure 2.14: (a) Time versus mol H_2/mol H_3NBH_3 plots for the m-g-CN/Pt catalyzed HAB conducted at different Pt loadings (1.16 wt%, 2.08 wt%, 3.82 wt%, and 5.94 wt%), (b) H_2 production rate (mL H_2 g_{Pt}^{-1} min^{-1}) comparison of the corresponding catalysts.[115]

Moreover, 3.82 wt% Pt loaded m-g-CN/Pt nanocatalysts is the one having the smallest average particle size (3.5 nm) with the most uniform particle distribution as shown in TEM images (Figure 2.3). Actually, except the 5.94 wt% Pt loaded one, showing agglomerated particles and clamps, all m-g-CN/Pt nanocatalysts have similar average particle size and dispersion of Pt NPs. That's why, 3.82 wt% Pt loaded m-g-CN nanocatalyst is preferred to be used for further kinetic studies since it supplied the second best H_2 generation rate of 23.3 L H_2 g_{Pt}^{-1} min^{-1} together with providing much less Pt loss in its preparation and having the smallest average particle size (3.5 nm) with the uniform particle dispersion.[115]

The kinetics of HAB were investigated by change of Pt amount, AB amount, and temperature. Firstly, Pt concentration is varied from 0.1 mM to 0.3 mM along with keeping AB amount constant to understand the effect of catalyst amount on photocatalytic H_2 production rate at 25 ± 0.5 °C. As shown in Figure 2.15a, the H_2 evaluation rate calculated from the linear portion of the graph increased as the Pt concentration is increased. The slope of the logarithmic plot of hydrogen generation rate versus Pt concentration was calculated to be 0.91. This value verified that the rate of HAB with respect to Pt concentration was the first-order (Figure 2.15b).[115]

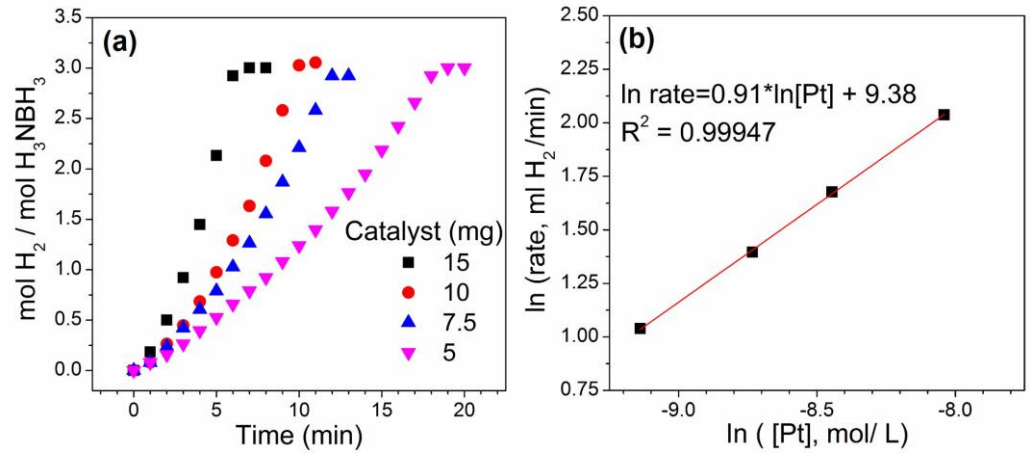

Figure 2.15: (a) Plot of molar amount of H_2 produced by HAB catalyzed by m-g-CN/Pt (3.82 wt% Pt) nanocatalyst versus time at different reaction conditions including [AB] = 100 mM, T = 25 °C, and [Pt] = 0.1−0.3 mM, (b) logarithmic plots of H_2 production rate versus Pt concentration.[115]

The volume of produced H_2 was also tested by varying AB concentration from 50 to 200 mM under white light irradiation at 25 ± 0.5 °C (Figure 2.16a). The slope of the logarithmic plot of hydrogen production rates versus AB concentrations equals to −0.08 (Figure 2.16b) such that the rate of HAB followed zeroth-order kinetics with respect to AB concentration.[115]

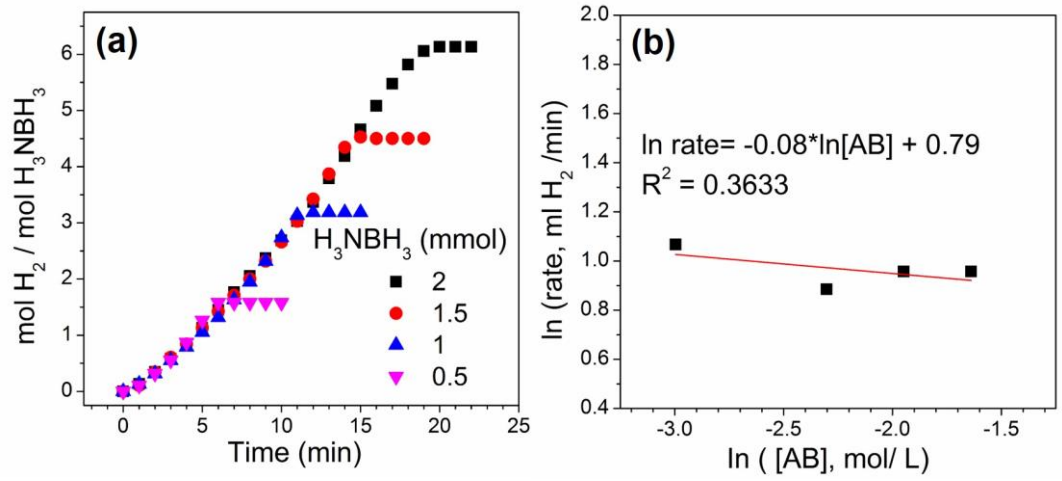

Figure 2.16: (a) Plot of molar amount of H_2 produced by HAB catalyzed by m-g-CN/Pt (3.82 wt% Pt) nanocatalysts versus time at different reaction conditions including [Pt] = 0.2 mM, T= 25 °C, and [AB] = 50-200 mM, (b) logarithmic plots of H_2 production rate versus AB concentrations.[115]

The effect of temperature on the catalytic activity was also studied by varying T from 288 K to 303 K. Hydrogen generation rate increases remarkably as the reaction temperature is increased (Figure 2.17a). According to the logarithmic plot of rate constant k_{obs} (the values of k_{obs} are shown in Table A1, see Appendix A) versus 1/T, which is known as Arrhenius plot, the apparent activation energy (E_a^{app}) was calculated to be 40.7 kJ/mol (Figure 2.17b).[115]

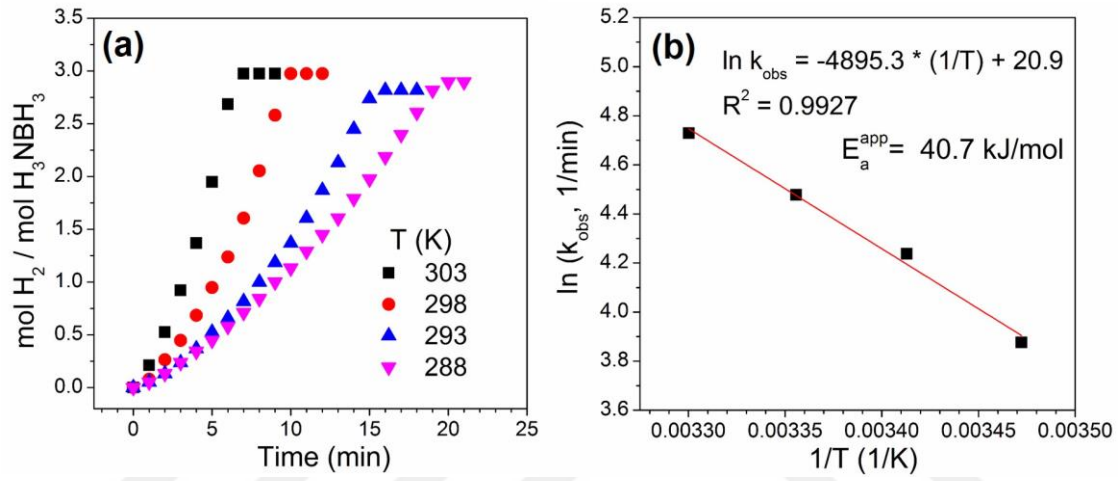

Figure 2.17: (a) Plot of molar amount of H_2 produced by HAB catalyzed by m-g-CN/Pt (3.82 wt% Pt) nanocatalysts versus time at different reaction conditions including [AB] = 100 mM, [Pt] = 0.2 mM, and T = 288-303 K, (b) Arrhenius plot of ln k_{obs} versus 1/T.[115]

A reusability test was also performed to understand the stability of the m-g-CN/Pt (3.82 wt% Pt) nanocatalysts in the HAB. After each run, the powder nanocatalysts was washed with ethanol/water mixture and precipitated via centrifugation at 9000 rpm along 10 mins. Next, it was dried at 80 °C in the centrifuge tube, dispersed in 8 mL of DI water, and added into the hydrogenation reactor for the next run. The hydrogen production rate of the m-g-CN/Pt (3.82 wt% Pt) nanocatalyst after 10th run was found to be 18.3 L H_2 g_{Pt}^{-1} min^{-1} such that it can maintain 78% of its initial activity after 10 runs (Figure 2.18a), which is an excellent recycling ability. After the 10th run, TEM picture of the nanocatalyst was taken to investigate any change in particle size and dispersion that might be the reason behind the decreased activity. According to Figure 2.18b, the average particle size increases from 3.5 to 7 nm after the 10th run, because more amount of reduced platinum involved in the formation of Pt NPs. This result is supported by Pt $4f_{7/2}$ XPS spectra

showing the increase in the ratio of Pt (0) to Pt (II) peak intensity after 10th run (Figure 2.7a). Besides, the Pt (0) NP formation is not completed even after 10th run according to Figure 2.7a. Activity loss is attributed to the increase in average particle size.[115]

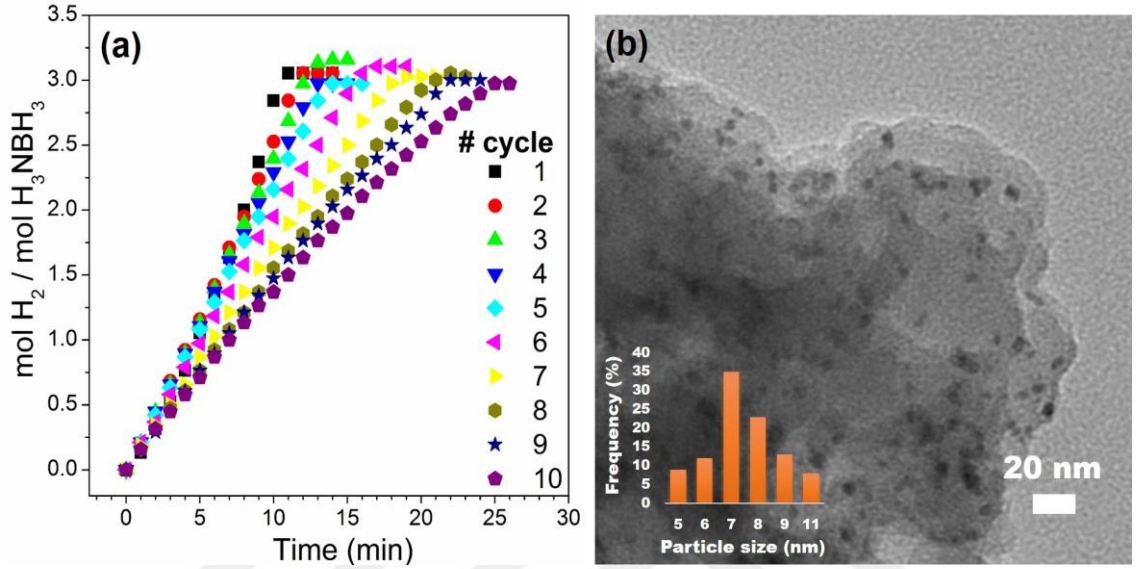

Figure 2.18: (a) H_2 generation versus time catalyzed by m-g-CN/Pt (3.82 wt% Pt) nanocatalyst during a 10-run reusability test, (b) TEM image of the nanocatalyst after 10th run.[115]

Chapter 3

U-g-CN/MPt NANOCATALYSTS FOR THE HAB

3.1 Introduction

As it is well known, bimetallic nanoparticles show better catalytic performance than their monometallic counterparts owing to the synergistic effect caused by the charge interaction between two distinct metals.[137] In this chapter, it was questioned whether the catalytic activity of m-g-CN/Pt Nano catalysts, which were already discussed in Chapter 2, could be improved via the preparation of bimetallic MPt (M: Au, Ag, and Cu) NPs supported on m-g-CN in the photocatalytic HAB. The method used for the synthesis of m-g-CN/Pt nanocatalysts described in Chapter 2 was also used for the synthesis of g-CN/MPt nanocatalysts with several modifications. For instance, the amine precursor used in the synthesis of m-g-CN was replaced with urea, which is greener and cheaper than guanidine hydrochloride. Additionally, the synthesis of g-CN from urea (abbreviated as U-g-CN hereafter) does not include the usage of any hard template and other chemicals for the etching process, which makes the synthesis of g-CN as more practical, economical, and time saving. Moreover, it is found that the catalytic activity of Pt NPs in the HAB was enhanced when they were synthesized on U-g-CN. The reasons behind the enhanced catalytic activity of U-g-CN/Pt than m-g-CN/Pt were discussed based on the characterization data acquired. From now on, U-g-CN was preferred as stabilizer and support material instead of m-g-CN for the synthesis of bimetallic MPt NPs. The discussion was carried on the activity of U-g-CN/MPt nanocatalysts in which M is one of the metals possessing surface plasmon resonance (SPR) including Au, Ag, and Cu. These metals were intentionally selected as the second metal by considering the fact that their SPR can resonate with UV-visible light and create a more effective heterojunction on semiconductor U-g-CN, which can result in improved photocatalytic activity in the HAB due to the enhanced electron density on the Pt atoms. Another reason behind the selection of these metals is that they have a proper reduction potential that can be reduced by AB at room temperature, which is not possible for first row transition metals such as Fe, Co, and Ni that are usually preferred for bimetallic alloy formations of Pt. The results revealed that U-g-CN/AuPt nanocatalysts showed higher catalytic activity compared to m-g-CN/Pt,

U-g-CN/AgPt, and U-g-CN/CuPt nanocatalysts. Therefore, this chapter is mainly focused on the detailed structural characterization of U-g-CN/AuPt nanocatalysts to find the reason behind its enhanced photocatalytic activity.

3.2 Experimental

3.2.1 Chemicals

Urea, hexachloroplatinic acid hexahydrate ($H_2PtCl_6.6H_2O$, >37.5% Pt basis, ACS reagent), tetrachloroauric acid trihydrate ($HAuCl_4.3H_2O$, ≥99.9% trace metals basis), silver nitrate ($AgNO_3$, ACS, 99.9+% (metals basis)), copper nitrate trihydrate ($Cu(NO_3)_2.3H_2O$, purum p.a., 98.0-103% (RT)), ammonia borane (AB, 97%), ethanol absolute (≥ 99.9%) and deionized water (DI, 0.055 $\mu S.cm^{-1}$) were purchased from Merck and used as received.

3.2.2 Instrumentation

All instruments described in the section *2.2.2* was also used for the characterization of materials synthesized in this chapter. Additionally, high-resolution TEM (HR-TEM), high annular angle dark field scanning transmission microscope (HAADF-STEM) images, and the associated EDS elemental mapping were recorded on a JEOL JEM-ARM200CFEG UHR-TEM instrument, equipped with STEM and EDS.

3.2.3 Synthesis of U-g-CN

The U-g-CN was synthesized by the thermal polycondensation of urea.[138] Briefly, 10 g of grounded urea was put into a porcelain crucible with a lid, and placed into a muffle furnace. It was kept at 80 °C for 1 h, heated up to 550 °C with a rate of 15 °C/min, kept at 550 °C for 4 h, and cooled naturally. The yellowish g-CN powder was obtained and used without further treatment.

3.2.4 Synthesis of U-g-CN/M(X)Pt(IV) composites (M(X): Au(III), Ag(I), Cu(II))

50 mg of U-g-CN was dispersed in 20 mL absolute ethanol by sonication in ultrasonic bath for 1 h. A certain amount of $H_2PtCl_6.6H_2O$ and a second metal precursor ($HAuCl_4.3H_2O$, $AgNO_3$, or $Cu(NO_3)_2.3H_2O$) were dissolved in DI water in two separate glass volumetric flasks to prepare their stock solutions. The stock solutions of metal salts of Pt, Au, Ag, and Cu have concentration of 7.96 mg/mL, 2.27 mg/mL, 2.29 mg/mL, and 1.63 mg/mL, respectively. All the prepared stock solutions were kept in dark at 4 °C. To impregnate Pt and M (Au, Ag, or Cu) salts into the g-CN, the calculated volume of prepared stock solutions was added dropwise into the dispersion of U-g-CN. The solutions were allowed to be sonicated for 3 h followed by overnight stirring on a magnetic stirrer at room temperature. Finally, the resulted

U-g-CN/Au(III)Pt(IV), U-g-CN/Ag(I)Pt(IV), and U-g-CN/Cu(II)Pt(IV) composites, including different compositions of M and Pt ions, were obtained by removing the solvent under vacuum.

3.2.5 In situ synthesis of U-g-CN/M_xPt_{100-x} nanocatalysts and the concomitant HAB

10 mg of U-g-CN/M(X)Pt(IV) composites were dispersed in 6 mL of DI water along 20 min in an ultrasonic bath. The dispersion was added into the two-necked jacketed reaction vessel via pipette and the remaining amount of the suspension was dispersed in additional 3 mL of water and added into the vessel. The same photocatalytic H_2 generation system described in Section *2.2.5* and schematically represented in Figure 2.1 was used for measuring the catalytic activities of the bimetallic Pt nanocatalysts. After the circulating water bath was adjusted to 25 ^oC and thermal equilibrium has been reached, 30.8 (1 mmol) mg of AB dissolved in 1 mL DI water was injected and the generated H_2 gas versus time was recorded. The obtained U-g-CN/MPt nanocatalysts were washed and dried by following the same procedures explained in Section *2.2.5*.

3.3 Results and Discussion

3.3.1 Comparison of the catalytic activities of U-g-CN/Pt and m-g-CN/Pt in the HAB and their characterization

ICP-MS was performed on as-prepared materials to determine the Pt content of U-g-CN/Pt nanocomposites. It is found that U-g-CN/Pt nanocomposites contain 4.24 wt%, which is close to that of m-g-CN/Pt nanocomposites, (3.82 wt% Pt, Table 2.1). TEM images of U-g-CN/Pt nanocatalysts recorded at different magnification with different scale bars (100, 50, 20 nm) and particle size histogram of Pt NPs were represented in Figure 3.1. It is clearly seen from the TEM images that highly dispersed Pt NPs were in situ generated on layered U-g-CN nanosheets (Figure 3.1a-c). The average particle size of Pt NPs supported on U-g-CN was calculated to be 2.6 nm (Figure 3.1d), which is slightly lower than that of ones on m-g-CN (3.5 nm). The reason behind the differences in the dispersion and average particle size of Pt NPs could be relied on the morphological differences in the m-g-CN and U-g-CN. Even though they both have similar specific surface area (SSA), which are found to be 182 and 183.04 m^2/g via BET method for m-g-CN and U-g-CN, respectively, their pore size distribution shows some differences due to the differences in their synthesis approaches.[116], [139] Firstly, m-g-CN has a very narrow pore diameter distribution with a single type of pore with an average pore size of 9 nm, which is an expected result for a porous material obtained via hard templating method. As also shown in the TEM images of m-g-CN/Pt nanocatalysts (Figure 2.3 and Figure A1), m-g-CN has

a sponge-like porous structure, and its porous structure is the main reason of the enhanced surface area compared to its bulk form. On the other hand, U-g-CN includes different types of pores, which are small (2-5 nm) and large (5-50 nm) mesopores and macropores (50-80 nm) due to absence of template to regulate pore size distribution.[139] Besides, U-g-CN is exfoliated into the thin nanosheets along heating process such that random aggregation of these nanosheets results in large number of pores.[140] This kind of morphological differences might be effective on the dispersion and particle size of Pt NPs growth on the m-g-CN and U-g-CN.

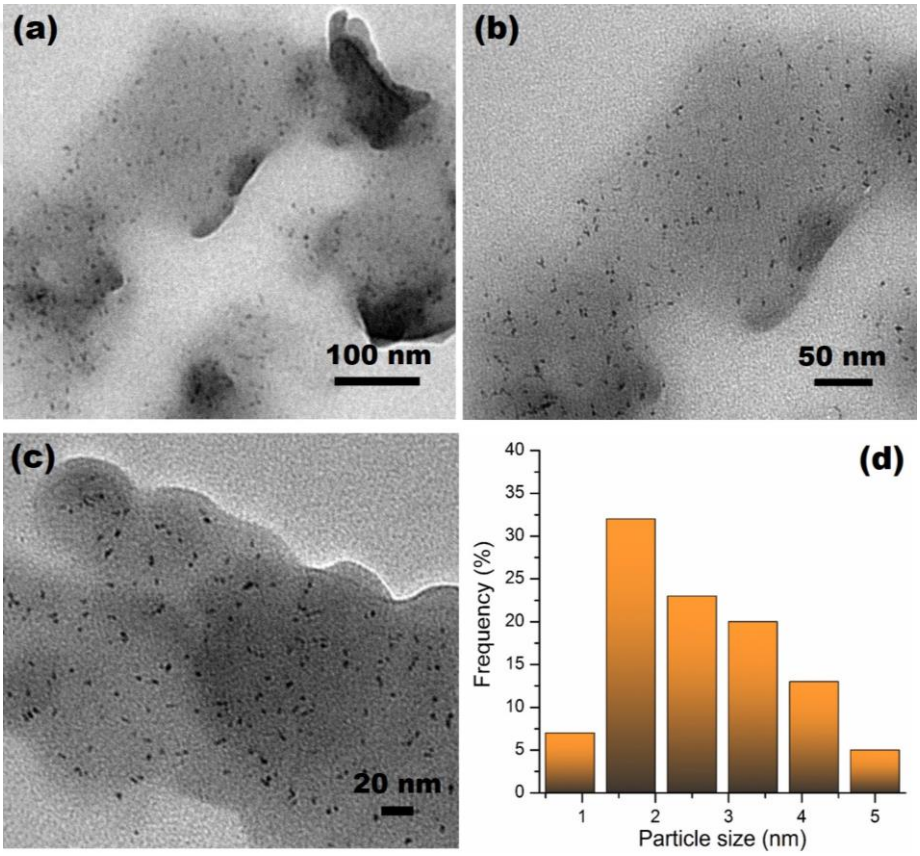

Figure 3.1: TEM images of U-g-CN/Pt (4.24 wt% Pt) nanocatalyst with different scale bars (a) 100 nm, (b) 50 nm, (c) 20 nm, (d) particle size distribution of Pt NPs.

XRD measurement was carried out to investigate the crystal structure of U-g-CN/Pt (4.24 wt% Pt) nanocatalysts. In the XRD pattern of U-g-CN/Pt shown in Figure 3.2, two major peaks at 2θ = 13.2° and 27.5° are attributed to (100) and (022) planes of U-g-CN, and the major peaks observable at 2θ = 39.8°, 46.0°, and 62.9° are referred to (111), (200), and (220) planes of fcc metallic Pt, respectively (JCPDS card no: 87−1526 and 88−2343). These results confirm that Pt NPs were successfully generated on U-g-CN.

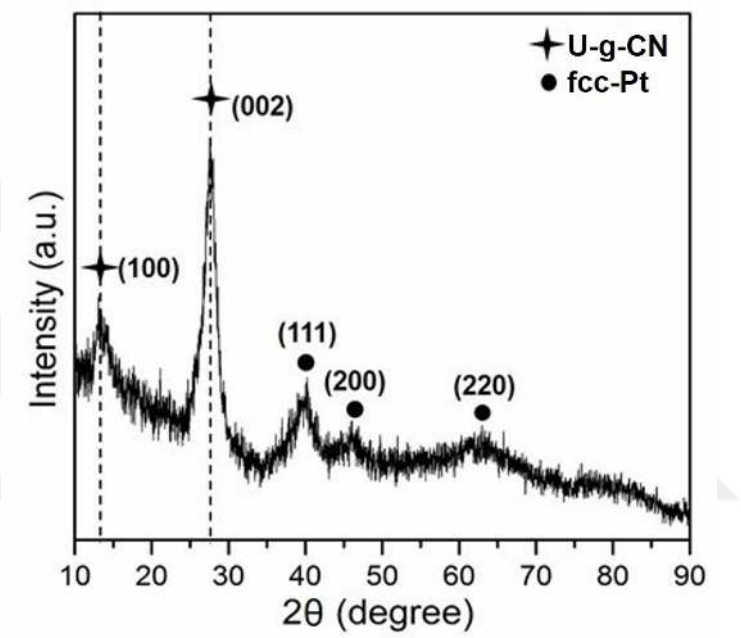

Figure 3.2: XRD pattern of U-g-CN/Pt (4.24 wt% Pt) nanocatalyst.

Since the U-g-CN and m-g-CN were used as a visible-light active semiconductor support material for the generation of Pt and MPt NPs, their photophysical properties were comparatively investigated by using diffuse reflectance (DRS), photoluminescence (PL), and time-resolved emission spectroscopy (TRES), to exhibit their differences. According to UV-Vis absorbance spectra shown in Figure 3.3a, U-g-CN and m-g-CN show similar absorption behavior in UV-vis region except that the absorption edge wavelength of U-g-CN is slightly shifted to a larger wavelength value, which was reflected on their band gap calculations. The band gap of U-g-CN was calculated as 2.80 eV from its Tauc plot, which is slightly lower than that of m-g-CN (2.84 eV, Figure 3.3b). The charge kinetics of the U-g-CN and m-g-CN were analyzed with PL and TRES, and the results were depicted in Figure 3.3c and 3.3d, respectively. As can be clearly seen from the PL spectra, emission intensity of m-g-CN is significantly lower than that of U--CN even though the lifespan of

the charges is higher in U-g-CN. When the lower PL intensity of m-g-CN was coupled with its lower charge lifespan, it can be concluded that non-radiative recombination is more effective in m-g-CN due to its mesoporous structure. Here, large number of mesopores in m-g-CN behaving like surface recombination centers lower the radiative recombination of the charges such that PL intensity is observed lower in m-g-CN compared to U-g-CN. That's why the PL intensity of m-g-CN is lower than U-g-CN even though the lifespan of charges of U-g-CN is higher.[141]

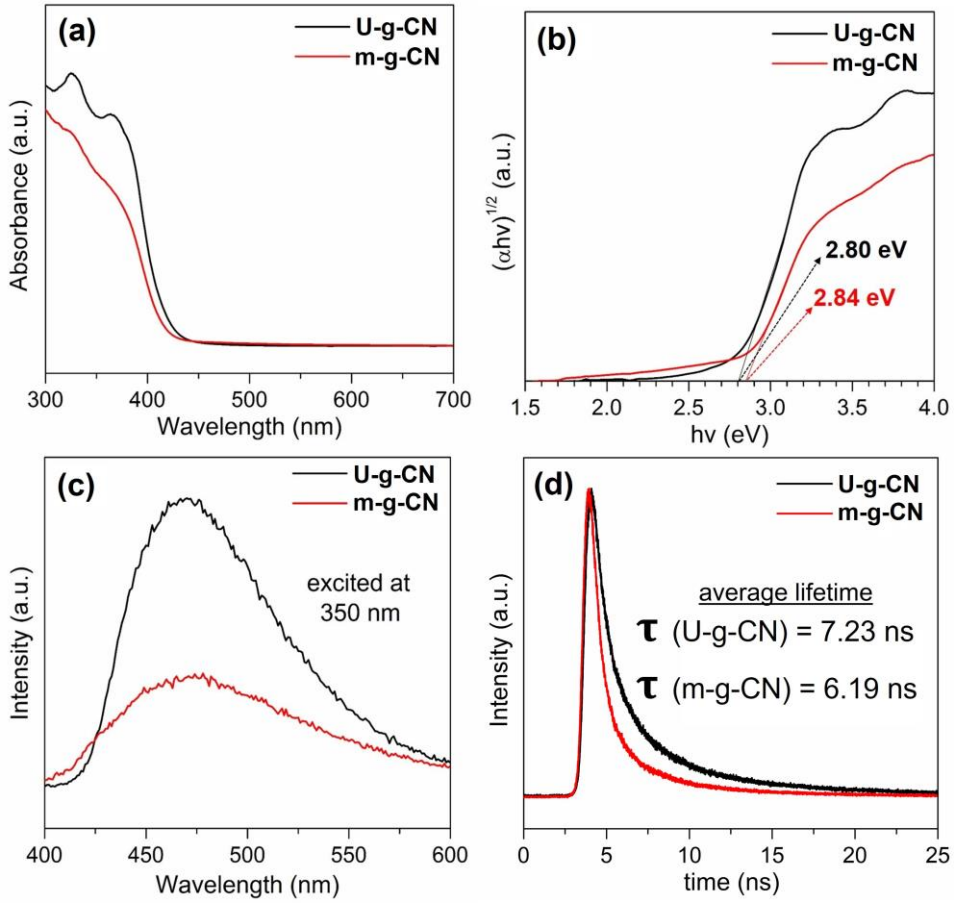

Figure 3.3: (a) UV−vis diffuse reflectance spectra, (b) Tauc plot, (c) PL spectra, and (d) time-resolved emission spectra of U-g-CN and m-g-CN support materials.

After the detailed structural characterization of both m-g-CN and U-g-CN, the comparison of the hydrogen generation rate of both m-g-CN/Pt and U-g-CN/Pt nanocatalysts in the HAB were illustrated in Figure 3.4. The enhanced absorption and emission properties, band gap, and charge kinetics of U-g-CN assisted with its higher photocatalytic activity, when it was suggested as support material instead of m-g-CN for the in situ growth of Pt NPs and dehydrogenation of AB, concomitantly. The photocatalytic hydrogen generation rate of U-g- CN/Pt nanocatalyst was

nearly 2-fold enhanced compared to m-g-CN/Pt, which was in agreement with the improved photophysical properties of the support material U-g-CN. That's why the next bimetallic MPt studies reported hereafter were conducted with the preference of U-g-CN instead of m-g-CN due to improved photophysical properties combined with enhanced photocatalytic activity, and the more practical and easy synthesis procedure than that of m-g-CN.

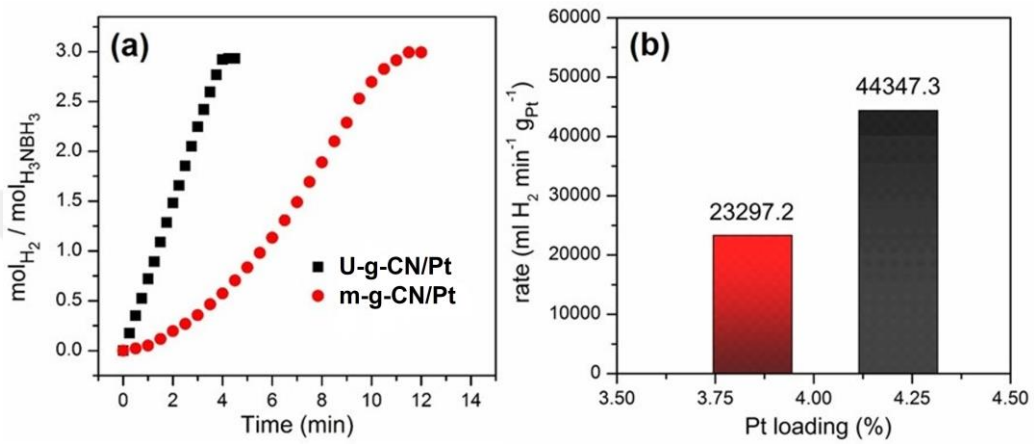

Figure 3.4: (a) Time versus mol H_2/mol H_3NBH_3 plots for the U-g-CN/Pt (4.24 wt% Pt) and m-g-CN/Pt (3.82 wt% Pt) catalyzed HAB conducted under white-light irradiation, (b) H_2 production rate graphs for each nanocatalyst.

3.3.2 Comparison of the catalytic activities of U-g-CN/MPt (M: Au, Ag, Cu) in the HAB and their characterization

Initially, U-g-CN/MPt nanocomposites including different amount of Pt and M were analyzed by ICP-MS to find the metal contents. According to the calculated weight percentage of the metals, the composition of each bimetallic nanocomposite was determined to be as illustrated in Table 3.1 which agrees with the experimental data.

Table 3.1: Pt and M loading weight percent (wt %) of U-g-CN/M(X)Pt(IV) composites by ICP-MS measurement.

Composition	Pt loading %	Au loading %	Ag loading %	Cu loading %
Pt_{100}	1.81	---	---	---
$Pt_{92}Au_8$	1.62	0.135	---	---
$Pt_{85}Au_{15}$	1.54	0.284	---	---
$Pt_{67}Au_{33}$	1.08	0.528	---	---
Au_{100}	---	1.58	---	---
$Pt_{92}Ag_8$	1.68	---	0.0765	---
$Pt_{81}Ag_{19}$	1.48	---	0.194	---
$Pt_{64}Ag_{36}$	1.21	---	0.381	---
Ag_{100}	---	---	1.38	---
$Pt_{90}Cu_{10}$	2.26	---	---	0.0799
$Pt_{81}Cu_{19}$	2.09	---	---	0.154
$Pt_{63}Cu_{37}$	1.53	---	---	0.287
Cu_{100}	---	---	---	0.672

Next, TEM analysis was performed on U-g-CN/$Pt_{100-x}Au_x$ and U-g-CN/Pt_{100} nanocatalysts. As clearly seen by the TEM images of all U-g-CN//$Pt_{100-x}Au_x$ (x=0, 8, 15, 33) nanocatalysts, highly dispersed small $Pt_{100-x}Au_x$ NPs having a narrow particle size distribution were observable in Figure 3.5. First, it can be concluded that there was no change in the morphology of the $Pt_{100-x}Au_x$ NPs as its composition was varied by introducing the Au metal. However, there were some clumps observable in the TEM images of bimetallic nanocatalysts. The Pt NPs formed on layered U-g-CN had an average particle size of 2.57 nm, which was slightly larger than that of bimetallic $Pt_{92}Au_8$, $Pt_{85}Au_{15}$, and $Pt_{67}Au_{33}$ NPs, calculated as 1.64, 2.44, and 2.01 nm, respectively (Figure 3.5c, f, h, k). $Pt_{92}Au_8$ NPs showed the smallest average particle size with the narrower particle size distribution and there was no observable linear relation between the average particle size and Au/Pt ratio in bimetallic compositions.

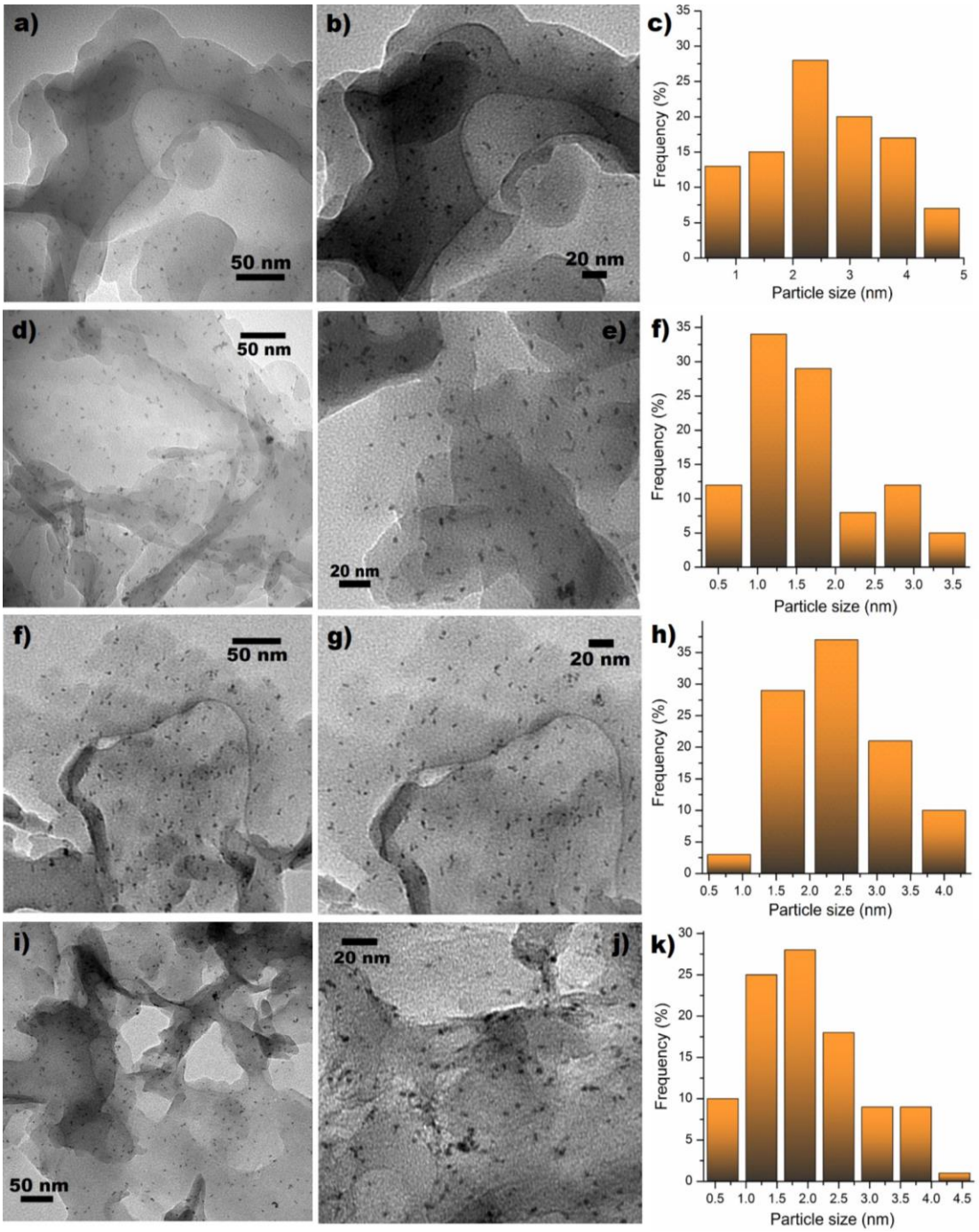

Figure 3.5: TEM images of U-g-CN/M_xPt_{100-x} nanocatalysts with 50 nm and 20 nm scale bars (a and b, d and e, f and g, i and j) for x=0, 8, 15, 33, respectively, particle size distribution of M_xPt100_{-x} NPs (c, f, h, k) for x=0, 8, 15, 33, respectively.

Figure 3.6a shows TEM image of U-g-CN/ $Pt_{92}Au_8$ nanocatalysts along with the inset showing a HRTEM image of $Pt_{92}Au_8$ NPs. From the HRTEM image of a single $Pt_{92}Au_8$ nanoparticle, it was concluded that $Pt_{92}Au_8$ had a lattice distance of 0.228 nm, which is between the lattice

distance values corresponding to (111) plane of fcc Pt (0.225 nm) and fcc Au (0.235 nm), implying that they might be formed in bimetallic alloys.[142] The HAADF-STEM and the associated EDX elemental mapping techniques were used to evaluate the distribution of the elements of N, Pt, Au in U-g-CN/$Pt_{92}Au_8$ nanocatalysts. From the elemental mapping images, it was concluded that Pt and Au were homogenously mixed in the $Pt_{92}Au_8$ NPs, which is supporting the formation of nanoalloy.

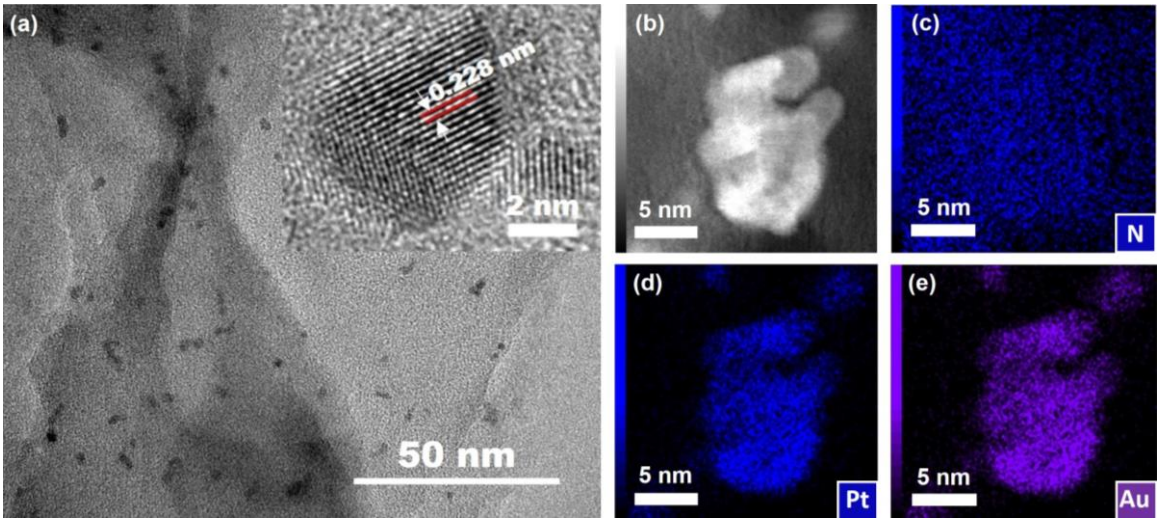

Figure 3.6: HRTEM image of U-g-CN/$Pt_{92}Au_8$ nanocatalyst with an inset image showing HRTEM image of $Pt_{92}Au_8$ NPs deposited on U-g-CN (a), HAADF-STEM image of U CN/$Pt_{92}Au_8$ nanocatalysts (b) with the associated EDX elemental mapping of N (c), Pt (d), and Au (e) elements.

To envisage the crystalline phases of the PtAu NPs, XRD analysis was carried out on U-CN/Pt_{100}, U-g-CN/$Pt_{92}Au_8$, U-g-CN/$Pt_{85}Au_{15}$, U-g-CN/$Pt_{67}Au_{33}$, and U-g-CN/Au_{100} nanocatalysts, and the recorded XRD patterns are depicted in Figure 3.7. The standard diffraction data of fcc phase of Pt and Au (JCPDS no. 70-2057 and 65-2868 respectively)[143], reveal that the peaks at $2\theta = 40.05^o$, 46.49^o, and 67.45^o observed in Pt_{100} pattern and the peaks at $2\theta = 38.37^o$, 44.56^o, 64.57^o observed in Au_{100} pattern can be associated with (111), (200), and (220) diffraction planes. As the Au/Pt atomic ratio is increased in nanocatalysts, both (111) and (200) planes are gradually shifted to lower 2θ degrees, falling between the 2θ degrees of corresponding (111) and (200) planes of individual metal NPs, Pt_{100} and Au_{100}. Additionally, the peaks observable at 2θ of 13.2^o and 27.5^o were assigned to (100) and (002) planes of U-g-CN, in accordance with the discussion in previous chapter.[138] These results support the solid-solution (alloy) formation between Au and Pt atoms.

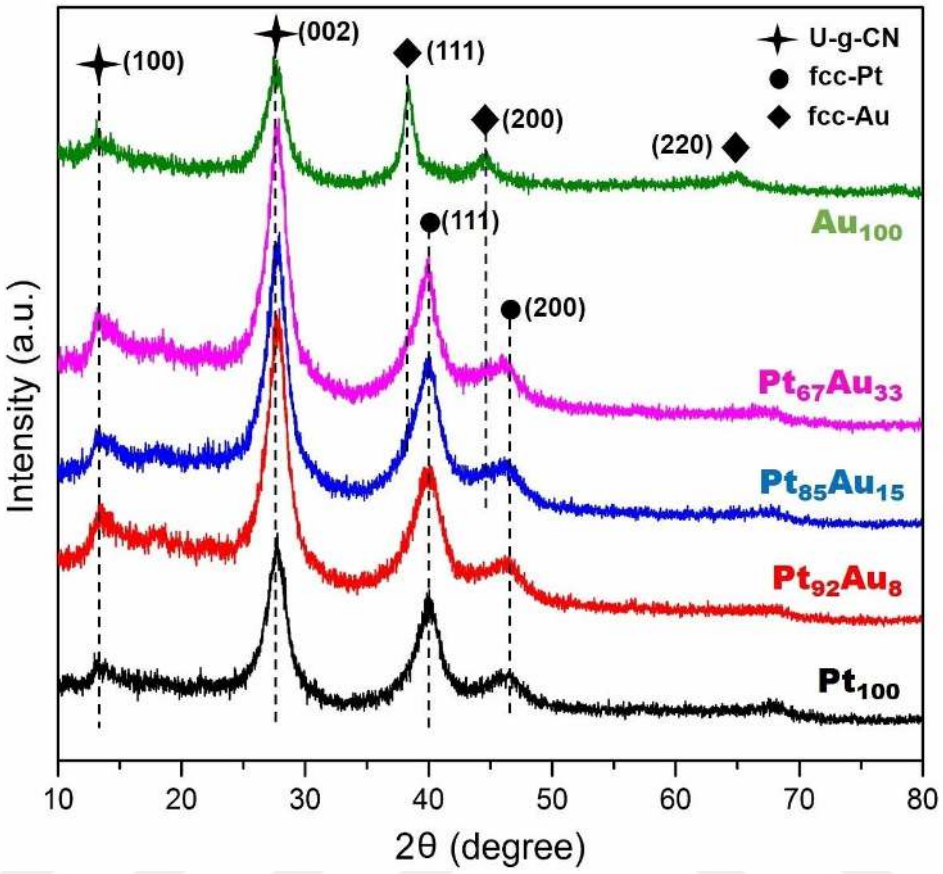

Figure 3.7: XRD patterns of U-g-CN/Pt_{100}, U-g-CN/$Pt_{92}Au_8$, U-g-CN/$Pt_{85}Au_{15}$, U-g-CN/$Pt_{67}Au_{33}$, and U-g-CN/Au_{100} nanocatalysts.

XPS measurement has been carried out to investigate the chemical states of the elements on the surface of U-g-CN/$Pt_{92}Au_8$ and U-g-CN/$Pt_{85}Au_{15}$ nanocatalysts, labelled on the graph according to their metal composition, as $Pt_{92}Au_8$ and $Pt_{85}Au_{15}$, respectively. XPS survey spectra of these nanocatalysts confirmed the existence of C, N, O, Pt, and Au atoms (Figure 3.8a). The XPS spectra of C 1s region were shown in Figure 3.8b, in which there were three major peaks at BEs of 284.5, 286.0, and 287.9 eV, which are attributed to C atoms in C–C or C = C functionalities, aromatic ring C coordinated to terminal amino group, and s-triazine aromatic ring C, respectively.[115] It should be noted that the BEs of all represented HR-XPS spectra were calibrated with reference to C 1s peak at 284.5 eV. In Figure 3.8c, XPS spectra of N 1s region displayed three major peaks at BEs of 398.4, 399.3, and 400.8 eV, which are referred to aromatic ring N, N connecting aromatic rings, and terminal amino group species, respectively. A slight shift from BE of 399.3 to 399.0 eV was observed when Au atomic percentage in the alloy was increased. A minor peak at 404.2 eV suggests the presence of $–NO_x$ functionalities due to the oxygen contamination. Figure 3.8d illustrates O 1s XPS spectra with two peaks at

531.8 and 533.0 eV, suggesting the presence of weakly adsorbed oxygen species on both U-g-CN and metals. In Figure 3.8e, Pt 4f XPS spectra of the U-g-CN/$Pt_{92}Au_8$ and U-g-CN/$Pt_{85}Au_{15}$ were represented together with that of U-g-CN/Pt_{100} nanocatalyst for comparison. In Pt_{100} spectra, the Pt $4f_{7/2}$ and Pt $4f_{5/2}$ peaks appear at BEs of 70.5 and 73.7 eV, indicating the presence of metallic Pt. It is worth noting that there were also two pairs of doublet peaks at BEs of 71.8/75.1 eV (doublet 1) and 74.2/76.9 eV (doublet 2), attributed to Pt^{2+} and Pt^{4+} ions (Figure A3, see Appendix). Owing to role of U-g-CN as a stabilizer, it was difficult to reduce all the Pt ions even after multiple times of reduction by AB, as discussed in Section 2.3. In Figure 3.8e, the zero-valent state of Pt was mainly shown to expand the discussion on the formation of alloy between Au and Pt. As the Pt loading of the composites was decreased, the intensity of Pt signals became weaker, as expected. In addition, the BEs of Pt 4f were slightly shifted to lower energy values compared to reference data of Pt_{100}, which is attributed to the electronic interaction between the Au and Pt nanoparticles. Figure 3.9f illustrates the Au 4f XPS spectra of the U-g-CN/$Pt_{92}Au_8$, U-g-CN/$Pt_{85}Au_{15}$, and reference U-g-CN/Au_{100} nanocatalysts, which presented peaks at BEs of 83.0 and 86.7 eV, which are readily assigned to Au $4f_{7/2}$ and Au $4f_{5/2}$ states of metallic Au, respectively. The intensity of Au peaks for the $Pt_{92}Au_8$ and $Pt_{85}Au_{15}$ nanoalloys agree with their stoichiometric ratios. These peaks show very slight shift but similar BEs when Pt was integrated into the nanoalloy with different ratios. Besides, two peaks observable at 84.3 and 88.1 eV are attributed to Au $4f_{7/2}$ and Au $4f_{5/2}$ peaks of Au^+ ion such that the partial reduction of Au was proven due to the stabilizing effect of U-g-CN, as it is also observed in Pt case (Figure A4, see Appendix). It is apparent from Figure 3.8e and 3.8f that both Pt 4f and Au 4f doublets slightly shift to lower binding energy in the alloys compared to their pure metal form, which is in conflict with electroneutrality consideration and a large number of previously reported AuPt alloy systems in which Au 4f peaks shift to higher binding energy.[143], [144] In literature, this contradiction was resolved by the charge compensation model showing that Au bimetallic systems can be interpreted according to s-d hybridization and charge compensation, which are caused by the electronegativity difference between Au and the second metal. If the electronegativity difference is small as is seen in the case of AuPt, charge transfer to Au is mainly 6s conduction character and d-charge depletion will take place to compensate 6s conduction flow to maintain electroneutrality locally.[145]

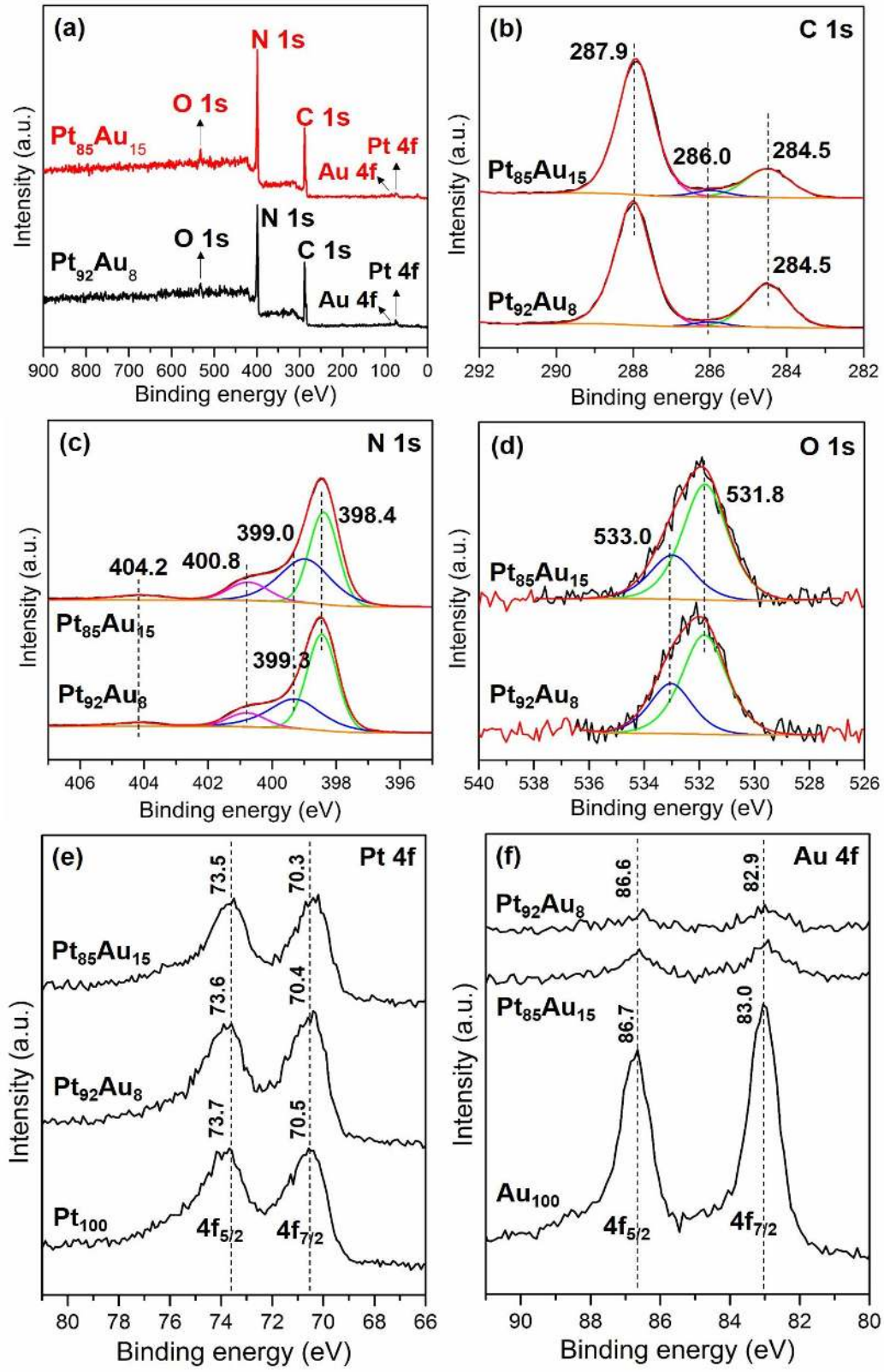

Figure 3.8: (a) XPS survey, HR-XPS (b) C 1s, (c) N 1s, (d) O 1s spectra of U-g-CN/$Pt_{92}Au_8$ and U-g-CN/$Pt_{85}Au_{15}$ nanocatalysts, (e) Pt 4f spectra of U-g-CN/Pt_{100}, U-g-CN/$Pt_{92}Au_8$, and U-g-CN/$Pt_{85}Au_{15}$ nanocatalysts, f) Au 4f spectra of U-g-CN/Au_{100}, U-g-CN/$Pt_{85}Au_{15}$, U-g-CN/$Pt_{92}Au_8$ nanocatalysts.

Next, the optical properties of the U-g-CN, U-g-CN/Pt_{100}, U-g-CN/$Pt_{92}Au_8$, and U-g-CN/$Pt_{85}Au_{15}$ nanocatalysts were investigated. Firstly, UV-Vis diffuse reflectance spectroscopy was carried out to analyze the absorption behavior of the nanocatalysts. As shown in Figure 3.9a, the absorption intensity is higher upon the growth of Pt or PtAu NPs on U-g-CN. The enhanced absorption ability of the nanocatalysts leads to change in their optical band gap values, which become less compared to U-g-CN. As calculated from the Tauc' plots of each measured nanocatalysts, the optical band gaps of U-g-CN, U-g-CN/Pt_{100}, U-g-CN/$Pt_{92}Au_8$, and U-g-CN/$Pt_{85}Au_{15}$ were found to be 2.80, 2.69, 2.72, and 2.68 eV, respectively (Figure 3.9b).

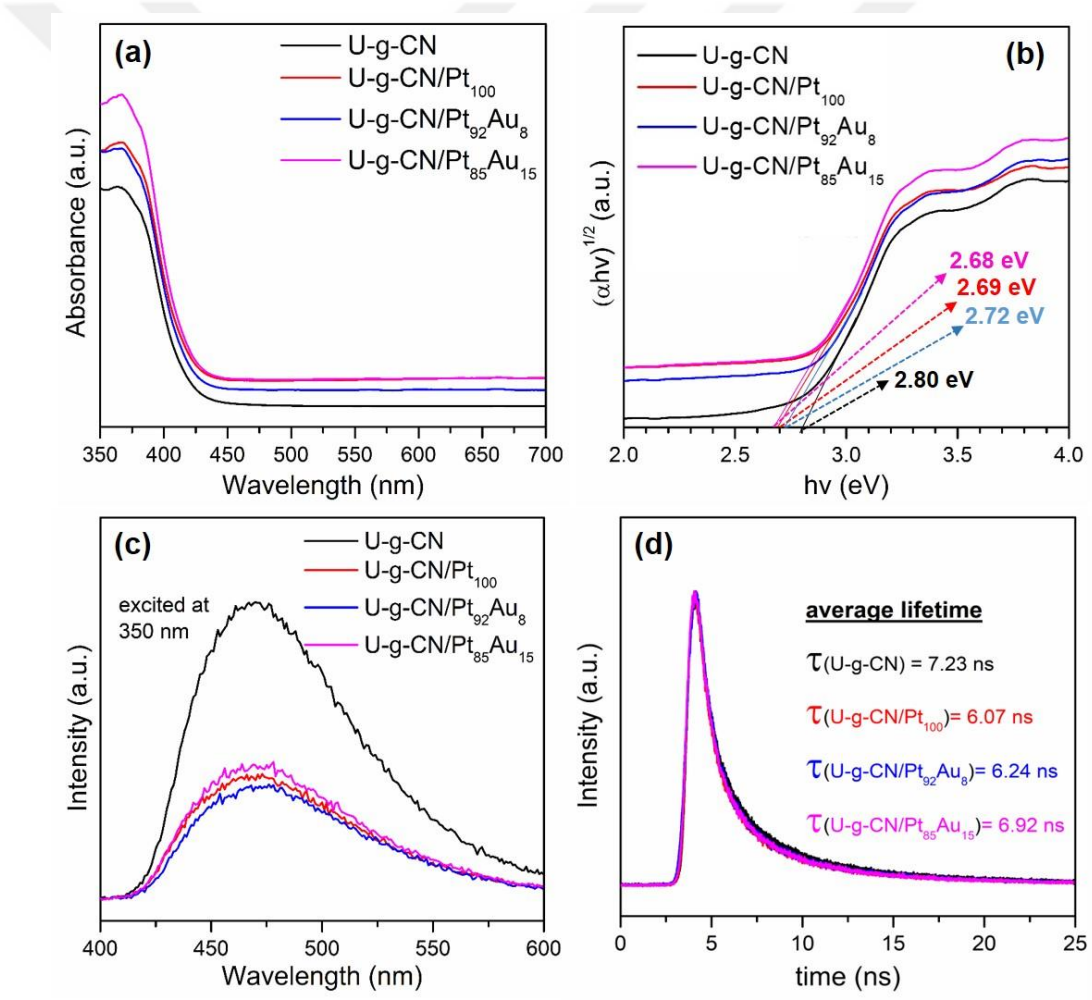

Figure 3.9: (a) UV-Vis Diffuse Reflectance spectra, (b) Tauc plot, (c) PL spectra, (d) Time-resolved emission spectra of U-g-CN, U-g-CN/Pt_{100}, U-g-CN/$Pt_{92}Au_8$, and U-g-CN/$Pt_{85}Au_{15}$ nanocatalysts.

Further analysis was performed with photoluminescence (PL) and time-resolved emission spectroscopy (TRES). According to Figure 3.9c, the emission intensity of U-g-CN was efficiently weakened after the growth of Pt or PtAu NPs on U-g-CN. As discussed in the previous chapter, the recovery of electron-hole separation rate and lower emission intensity of U-g-CN is inevitable when the Schottky barrier was built up via generation of Pt NPs on U-g-CN. The same statement is also acceptable in the case of PtAu NPs. Besides, the variation of composition in bimetallic PtAu NPs does not result in change of their emission intensities significantly. The collected time-resolved emission spectra of the nanocatalysts, where biexponentional fitting was applied to calculate average lifetime of the charges, were illustrated in Figure 3.9d. By comparison to bare U-g-CN (τ_{av} = 7.23 ns), U-g-CN/Pt_{100} (τ_{av} = 6.07 ns), U-g-CN/$Pt_{92}Au_8$ (τ_{av} = 6.24 ns), and U-g-CN/$Pt_{85}Au_{15}$ ((τ_{av} = 6.92 ns) show much shorter lifetimes ((τ_{av}, inset of Figure 3.9d) which implies the presence of effective electron transfer channels from U-g-CN to the mono/bimetallic Pt NPs.[146] The lifetime of U-g-CN/Pt is even shorter than that of U-g-CN/$Pt_{92}Au_8$ and U-g-CN/$Pt_{85}Au_{15}$, demonstrating more efficient charge transfer from U-g-CN to monometallic Pt NPs. It should be noted that as the higher ratio of Au in the PtAu alloy NPs, the longer lifespan of the charges, and the higher PL intensity. The reason behind this observation might be the SPR effect of Au metal, triggering the flow of the electrons from Au metal to conduction band of U-g-CN via hot electron mechanism. This back flow of the electrons from Au metal to U-g-CN can elongate the lifespan of the charges along with increased PL intensity.[147]

Until now, the characterization of U-g-CN/PtAu nanoalloys were mainly focused on eludicating their higher photocatalytic activity in HAB. As shown in Figure 3.10, only U-g-CN/$Pt_{92}Au_8$ and U-g-CN/$Pt_{85}Au_{15}$ nanocatalysts provided higher photocatalytic hydrogen production compared to U-g-CN/Pt. The hydrogen production rate of 68.9 and 67.4 L H_2 g_{Pt}^{-1} min^{-1} were achieved by U-g-CN/$Pt_{92}Au_8$ (1.62 wt% Pt) and U-g-CN/$Pt_{85}Au_{15}$ (1.54 wt% Pt) nanocatalysts, respectively. However, there is a distinct drop in the catalytic activity after introducing higher amount of Au into the PtAu nanoalloy structure, and the catalytic activity of Au was found to be negligible as shown from the hydrogen generation graph of U-g-CN/Au_{100} (Figure 3.10a). The catalytic activity of U-g-CN/$Pt_{100-x}Au_x$ nanocatalysts with different Au/Au+Pt ratios in the HAB showed a volcano-shaped relationship. This behavior can be explained by the Sabatier' principle which is a general paradigm in heterogeneous catalysis field. It states that an optimum catalytic activity can be achieved on a catalytic surface with median binding energies for reactive intermediates. If the intermediates bind to surface too

weakly, it is difficult for the catalyst to activate them. Besides, if they bind too strongly, all the available active sites of the catalyst will be poisoned.[148], [149] Thus, in optimum ratio between Pt and Au in $Pt_{100-x}Au_x$ nanoalloy, a surface of nanoalloy catalyst, where the adsorption of substrates and desorption of products are the most favorable, is achieved.

In addition to the alloying effect between the Au and Pt metals, which resulted in an enhanced photocatalytic activity of U-g-CN/Au_1P_9 at the optimum composition, the plasmonic effect of Au metal, which might be causing electrons to flow on Pt under light, should also be emphasized in the higher catalytic activity of PtAu alloy NPs. Along with the electrons, which are originated by photo responsive U-g-CN and transferred to the Pt, the electron-enriched active Pt sites can be generated for a better release of hydrogen via HAB, which is triggered by the electron flow from active Pt sites to the electron deficient boron. Moreover, the back flow of the electrons from Pt to the CB of U-g-CN and hot electron transfer from Au metal to U-g-CN can be hindered to a certain extent thanks to the formation of Schottky barrier. It can be concluded that enhanced photocatalytic activity of AuPt is attributed to the combination of both alloying, plasmonic effects of Au, and formation of Schottky barrier.[150]

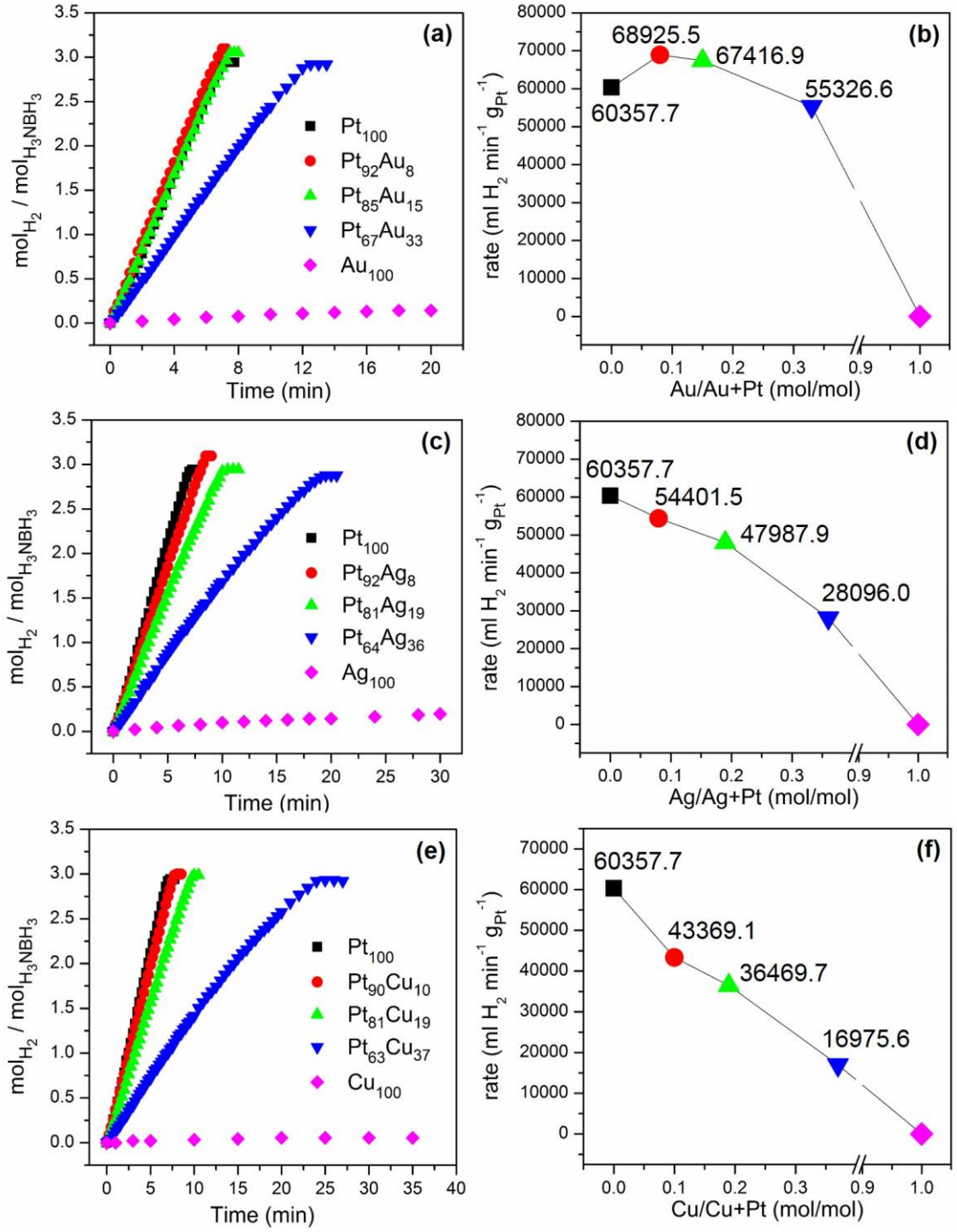

Figure 3.10: Time versus mol H_2/mol H_3NBH_3 plots for the U-g-CN/$Pt_{100-x}M_x$ catalyzed HAB reaction with different x values and M elements: x= 0, 8, 15, 33, 100 and M= Au (a), x= 0, 8, 19, 36, 100 and M= Ag (c), x= 0, 10, 19, 37, 100 and M= Cu (e); M/(M+Pt) versus H_2 production rate plots for M= Au (b), M= Ag (d), M= Cu (f).

The kinetics of U-g-CN/$Pt_{92}Au_8$ catalyzed HAB was investigated by varying the catalyst amount, AB amount, and the temperature under the white light illumination. The effect of catalyst amount on hydrogen generation rate was analyzed via maintaining AB amount (1 mmol) and temperature (25 ^oC) constant. The increase in the catalyst concentration ([Pt], mM) from 0.0415 mM to 0.125 mM leads to a rise in H_2 production rate (Figure 3.11a). The slope of the logarithmic plot of hydrogen generation rate versus Pt concentration was found to be 0.99, confirming that the rate with respect to Pt concentration is first-order (Figure 3.11b). The effect of AB concentration on hydrogen production rate was also tested by keeping catalyst concentration and temperature constant at 0.0831 mM and 25 ^oC, respectively, and varying AB concentration between 0.05-0.2 M, as shown in Figure 3.11c. The logarithmic plot of hydrogen generation rate versus AB concentration has given a slope of -0.02, indicating that the HAB reaction is independent of AB concentration (Figure 3.11d). Lastly, the effect of temperature on the reaction was investigated by keeping amount of catalyst and AB constant at [Pt] = 0.0831 mM [AB] = 0.1 M, and changing the temperature between 288-303 K. A remarkable enhancement in hydrolysis rate is observed as the reaction temperature is raised up (Figure 3.11e). The rate constant, k_{obs}, for each T condition was calculated (the values of k_{obs} are shown in Table A2, see Appendix A) and the Arrhenius plot was obtained by plotting the logarithmic value of k_{obs} versus the inverse temperature (1/T). According to the slope of Arrhenius plot, the apparent activation energy (E_{app}) of the U-g-CN/$Pt_{92}Au_8$ nanocatalyst in HAB was calculated to be 52.7 kJ/mol, which is larger than that of m-g-CN/Pt (3.82 wt% Pt) nanocatalyst, 40.7 kJ/mol (Figure 3.11f).

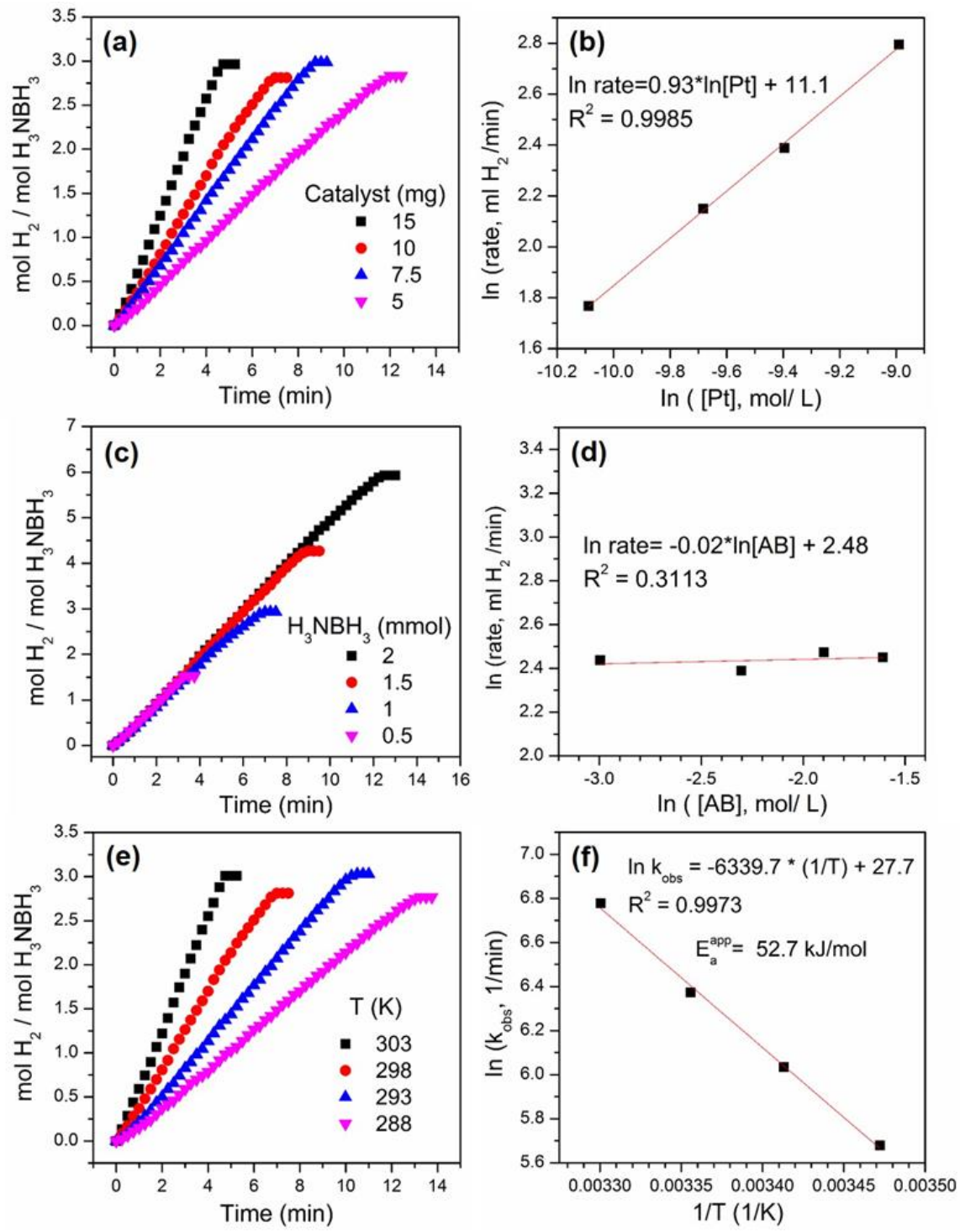

Figure 3.11: Time versus mol H_2/mol H_3NBH_3 plots for the U-g-CN/$Pt_{92}M_8$ catalyzed HAB reaction at different reaction conditions including (a) [AB] = 0.1 M, T = 25 °C, and [Pt] = 0.0415 −0.125 mM, (c) [Pt] = 0.0831 mM, T= 25 °C, and [AB] = 0.05-0.2 M, (e) [AB] = 0.1 M, [Pt] = 0.0831 mM, and T = 288-303 K; logarithmic plots of H_2 production rate versus (b) Pt concentration, (d) AB concentration, (f) Arrhenius plot of ln k_{obs} versus 1/T.

A reusability test was performed to understand the durability of the U-g-CN/$Pt_{92}Au_8$ nanocatalysts in the HAB (Figure 3.12a). After each run, the nanocatalysts were collected by following the same washing and drying procedure explained in Section 2.3. In the 5th run, it can only maintain 35% of its initial hydrogen production (L H_2 min^{-1}). TEM image of the nanocatalyst after 5th run was taken to investigate any change in particle size and dispersion. The average particle size was calculated to be 2.61 nm, larger than its initial size (Figure 3.12b). Besides, there were some observable agglomerates which might contribute to lower hydrogen production together with the loss of catalyst amount during washing/drying process.

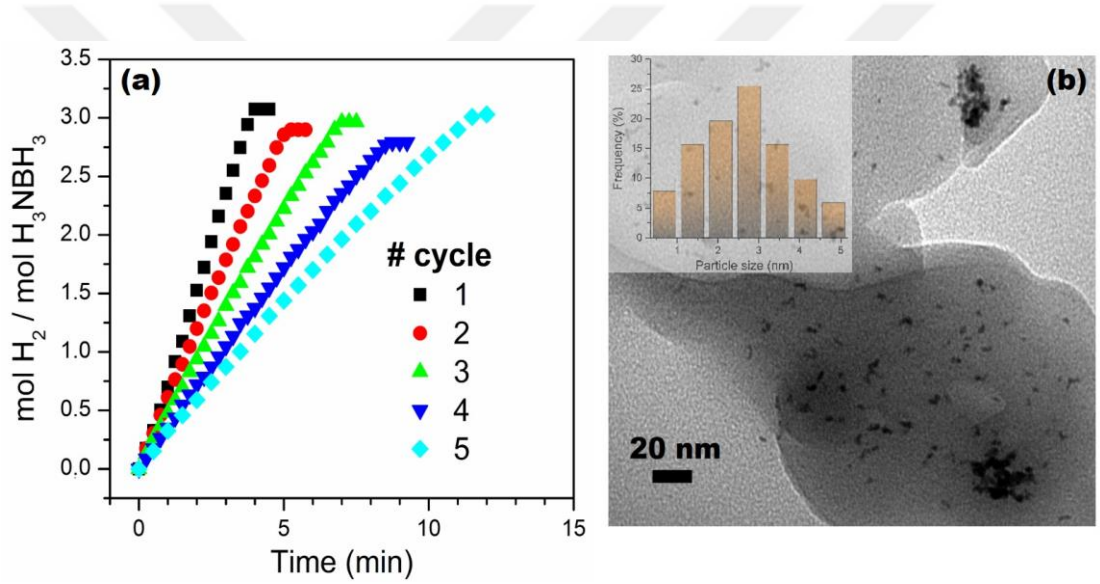

Figure 3.12: (a) H_2 generation versus time catalyzed by U-g-CN/$Pt_{92}M_8$ nanocatalyst during a 5-run reusability test, (b) TEM image of the nanocatalyst after 5th run.

Chapter 4

U-g-CN/a-WO_x/Pt NANOCATALYSTS FOR THE HAB

4.1 Introduction

As it was already discussed in the previous chapters, g-CN as a support material possesses many advantages such as being non-toxic, metal-free, and earth abundant 2D semiconductor along with having visible light response and a narrow band gap of ~2.7 eV. Then, we also showed that U-g-CN possessed several other advantages such as being easily prepared, improved charge kinetics and photophysical properties. However, photocatalytic activity of pristine U-g-CN is still poor compared to traditional inorganic semiconductor photocatalysts mainly due to the high recombination rate of photogenerated electron-hole pairs. This drawback of the U-g-CN can be eliminated via the construction of its heterojunctions with other semiconductors having proper band gap and edge potentials. [151]–[153] In this respect, oxygen-deficient/non-stoichiometric tungsten oxides, called as WO_x, are very active materials for various photocatalytic applications. Depending on the valence state of W, which is varied between +6 and +4, the electronic structure and optical properties of WO_x can be modified continuously.[111], [154], [155]

In this chapter, the fabrication of U-g-CN/WO_x heterojunctions was aimed to provide a further enhancement in the separation and transfer of photogenerated charge carriers of U-g-CN as a semiconductor support material for the synthesis of Pt NPs. A facile synthesis method, comprsing the thermal decomposition of $Na_2WO_4.2H_2O$ in the presence of urea, was followed. Next, in-situ synthesis of Pt NPs supported on as-prepared U-g-CN/WO_x nanocomposites during the HAB was realized under the white-light irradiation. The effect of white light and W loading on the photocatalytic activity of U-g-CN/WO_x/Pt nanocatalysts were investigated in the HAB. The reasons behind the enhancement of photocatalytic activity were also discussed based on their characterization results.

4.2 Experimental

4.2.1 Chemicals

Urea, sodium tungstate dihydrate ($Na_2WO_4.2H_2O$, ≥ 99%, ACS reagent), chloroplatinic acid hexahydrate ($H_2PtCl_6.6H_2O$, >37.5 % Pt basis, ACS reagent), ammonia borane (AB, 97%), ethanol absolute (≥ 99.9%) and deionized water (DI, 0.055 $\mu S.cm^{-1}$) are the chemicals and solvents purchased and used as received.

4.2.2 Instrumentation

All instruments mentioned in Section *2.2.2* were used.

4.2.3 Synthesis of U-g-CN/WO_x nanocomposites

For the synthesis of pristine U-g-CN, 5 gram of urea was put into a quartz holder covered with a quartz lid and placed in a tubular quartz furnace under a gentle argon gas flow. The urea was heated to 550 ºC within 2 hours and kept at this temperature for 4 h, and then let to be cooled down naturally. The yielded yellow g-CN powder was weighted (215 mg) and proper amount of $Na_2WO_4.2H_2O$ salt to be used for the synthesis of experimentally 1-5 wt% W theoretically was loaded to g-CN. The required amount of $Na_2WO_4.2H_2O$ salt was found to be 3.9, 7.9, 11.9, 16.1, and 20.3 mg to get experimentally 1, 2, 3, 4, and 5 wt% W loaded composites, respectively. After that, the calculated amount of $Na_2WO_4.2H_2O$ salt was weighted and mixed with 5 gram of urea by grinding in a mortar with pestle along 15 min. The grinding mixture was heated by just following the same heating procedure, which is applied to urea to obtain bare U-g-CN. After heating, the brownish yellow colored U-g-CN/WO_x nanocomposites were obtained and labelled according to their theoretical W loading percent. It is worth noting that as the amount of W incorporated into the nanocomposite was increased, color of the yielded nanocomposite gets dark brown.

4.2.4 Synthesis of U-g-CN/WO_x/Pt(IV) composites

30 mg of U-g-CN/WO_x nanocomposites was dispersed in 10 mL of absolute ethanol by sonication in the ultrasonic bath for 1 hour. A certain amount of $H_2PtCl_6.6H_2O$ salt dissolved in DI water was added into the U-g-CN/WO_x dispersion dropwise under sonication. The resultant dispersion was sonicated in the ultrasonic bath for 3 hours, followed by overnight stirring. Finally, theoretically 1 wt% Pt loaded U-g-CN/WO_x/Pt(IV) composite was obtained by evaporation of solvent at 50 ºC under vacuum.

4.2.5 In-situ synthesis of U-g-CN/WO$_x$/Pt nanocatalysts and the concomitant HAB

10 mg of U-g-CN/WO$_x$/Pt(IV) composites were dispersed in 6 mL of DI water in the ultrasonic bath along 20 minutes. The all mixture was inserted into the reaction vessel via pipette and the residual amount of mixture was again dispersed in 2 mL of water and added into the vessel. The same system described in Section *2.2.5* and schematically represented in Figure 1.6 was used to measure the H_2 generation during the HAB. Hydrogen generation was initialized with the addition 30.8 mg of AB dissolved in 2 mL of H_2O. The obtained U-g-CN/WO$_x$/Pt nanocatalysts were washed and dried by following the same procedures explained in Section *2.2.5*.

4.3 Results and Discussion

The W and Pt contents of the U-g-CN/WO$_x$/Pt nanocatalysts were determined by conducting ICP-MS analysis. As shown in Table 4.1, there is a difference between the theoretical and experimental wt% W (determined by ICP-MS) loadings, gets larger by increasing the theoretical W loading. The reason might be attributed to the higher decomposition of urea into the gaseous by-products such as CO_2 and NH_3 in the presence of more $Na_2WO_4.2H_2O$ salts. The same amount of Pt precursor was added into all U-g-CN/WO$_x$ nanocomposites to yield U-g-CN/WO$_x$/Pt(IV) composites with 1 wt% Pt loading. According to the ICP-MS results, Pt loading of the composites were consistent with their theoretical loading percent, and they were relatively close to each other.

Table 4.1: W and Pt loading weight percent (wt %) of U-g-CN/WO$_x$/Pt(IV) composites by ICP-MS measurements.

W loading % (theoretical)	W loading % (ICP-MS)	Pt loading % (ICP-MS)
5	13.4	-
4	10.3	0.690
3	4.72	0.679
2	1.92	0.729
1	0.845	0.706
0	-	0.742

Since the highest photocatalytic activity of the U-g-CN/WO_x/Pt nanocatalysts in HAB was achieved when the U-g-CN/WO_x heterojunction containing 4.72 wt% W was used as support material for the in-situ synthesis of Pt NPs during HAB, the structural characterization studies was mainly done on these samples. The morphology and elemental distribution in the U-g-CN/WO_x (4.72 wt% W) heterojunctions were characterized by TEM and high-angle annular dark field STEM (HAADF-STEM) coupled with EDX elemental mapping. Figure 4.1a-d exhibit a typical layered structure of U-g-CN including large number of pores in nanometer size which is caused by the release of CO_2 and H_2O during the thermal polycondensation of urea. There were some wrinkled paper-like aggregated nanostructures observable in the darker region of the images, which are attributed to the WO_x species. Figure 4.1e-i displays a HAADF-STEM image and the associated elemental mapping analyses for N, W, and O atoms. These results implied that g-CN and WO_x species were almost homogenously distributed in the composite structure.

TEM images of the U-g-CN/WO_x/Pt nanocatalysts were also recorded to investigate morphology and distribution of the Pt NPs over U-g-CN/WO_x composites. As shown in Figure 4.2a-c, ultra-small Pt NPs with an average particle size of 1.51 nm were dispersed on the U-g-CN/WO_x composites without any agglomeration. Additionally, there was no noticeable change observable in the layered structure of U-g-CN in conjunction with the other wrinkled paper-like WO_x structures. Due to very low loading of Pt (0.679 wt%) in the U-g-CN/WO_x/Pt(IV) composite, the Pt NPs generated on the composite looked highly apart from each other. Additionally, the HAADF-STEM image (Figure 4.2e) associated EDX elemental mapping images for C, N, W, O, and Pt (Figure 4.2f-k) displayed that Pt NPs were deposited on both g-CN nanosheets and wrinkled paper-like WO_x structures. Upon these results, it can be concluded that Pt formed Schottky junctions on both g-CN and WO_x, which enhances its photocatalytic activity in HAB compared to that of U-g-CN/Pt nanocatalyst including no WO_x species.

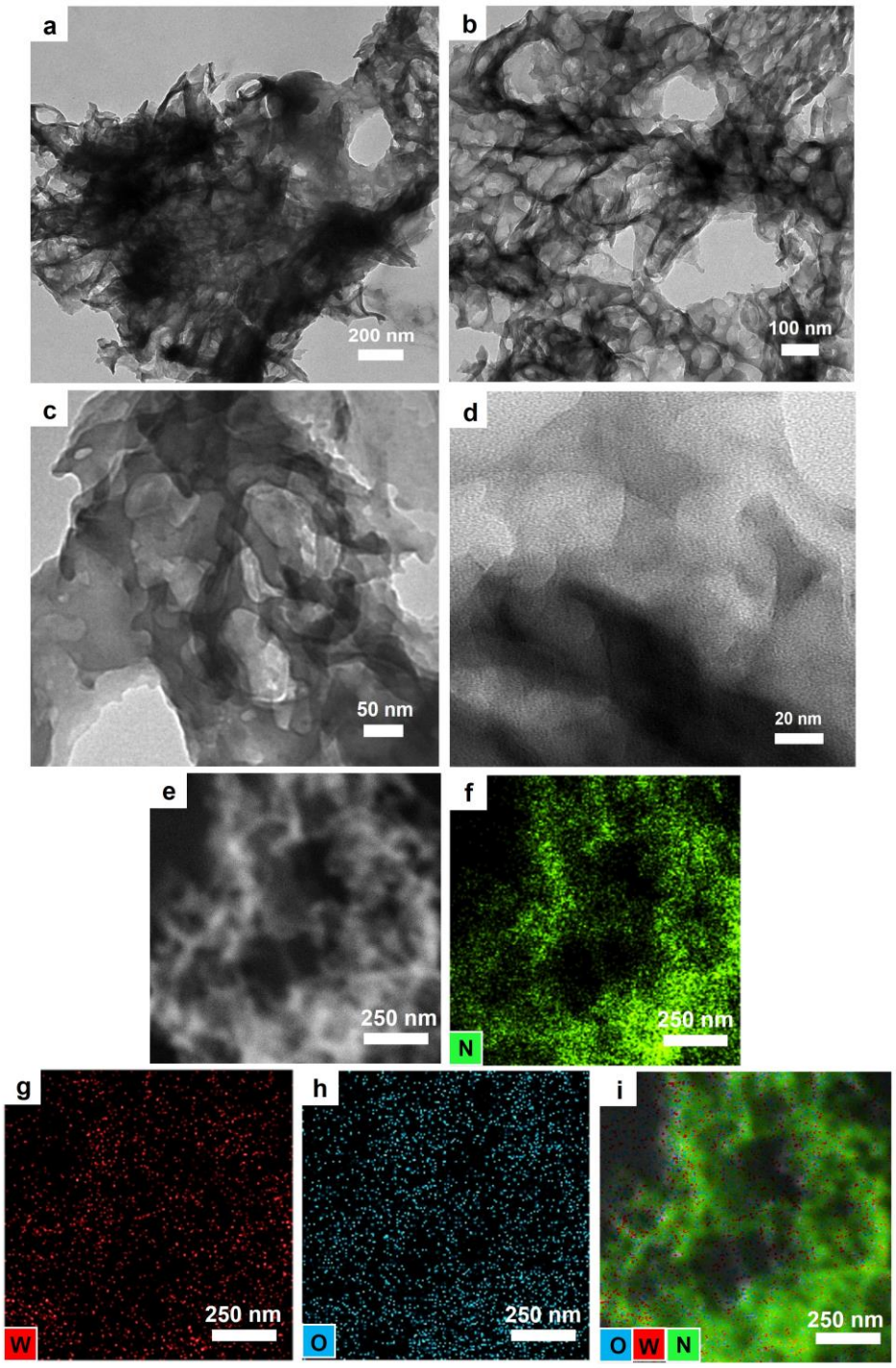

Figure 4.1: TEM images of U-g-CN/WO_x (4.72 wt% W) nanocomposite with 200 nm, 100 nm, 50 nm, and 20 nm scale bars (a-d), HAADF-STEM image (e), corresponding EDX elemental mapping images of U-g-CN/WO_x (4.72 wt% W) nanocomposite (f-i). The green, red and blue dots represent N, W, and O, respectively.

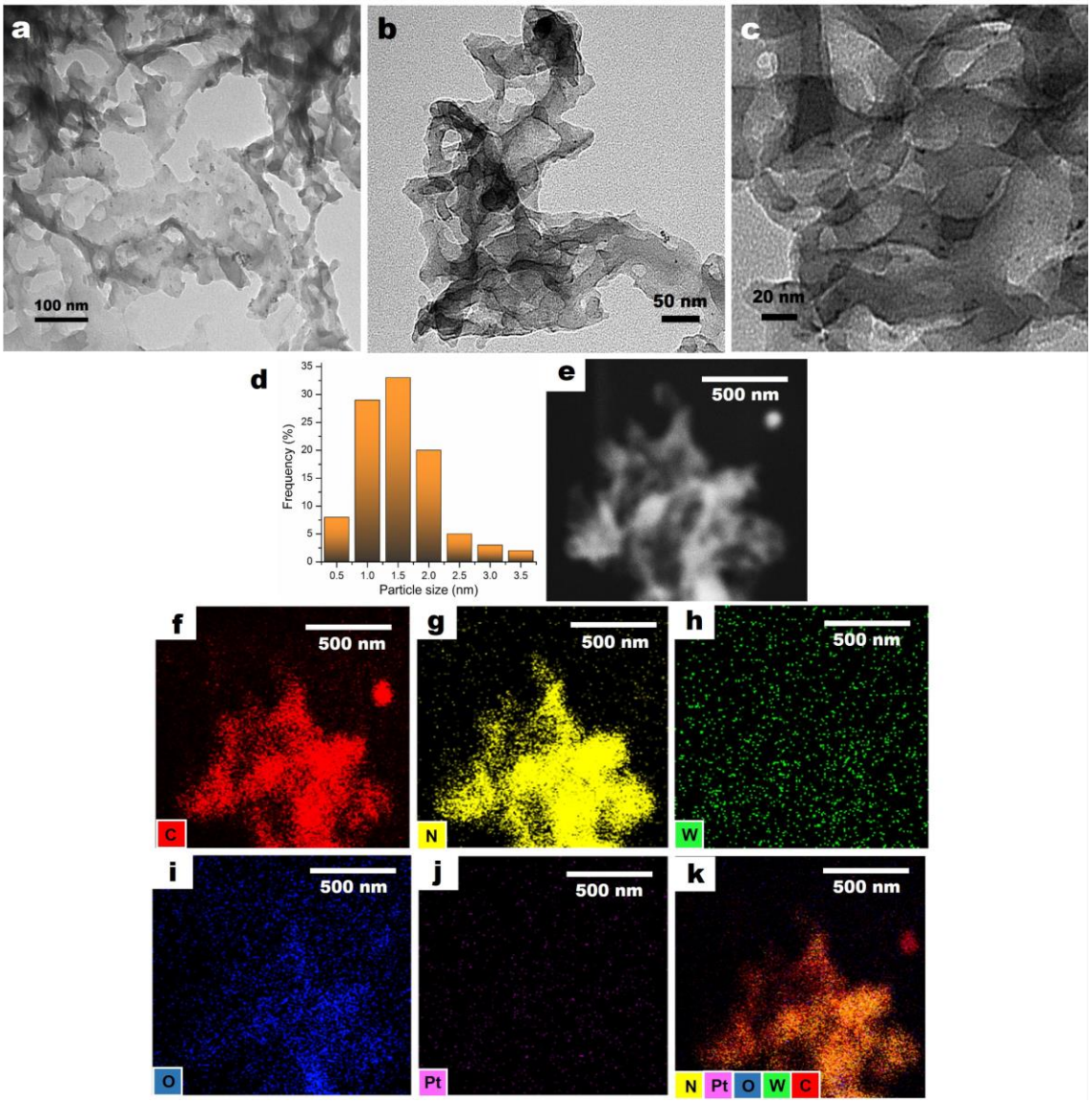

Figure 4.2: TEM images of U-g-CN/WO_x/Pt (4.72 wt% W and 0.679 wt% Pt) nanocatalyst with 100 nm, 50nm, and 20 nm scale bars (a, b, and c), Pt NP size distribution histogram (d), HAADF-STEM image (e), corresponding EDX elemental mapping images of U-g-CN/WO_x/Pt (4.72 wt% W and 0.679 wt% Pt) nanocatalysts (f-k). The red, yellow, green, blue, and pink dots represent C, N, W, O, and Pt, respectively.

After the morphological characterization, XRD was employed to investigate the crystal structure of U-g-CN/WO_x composites containing different amount of W. For the pure U-g-CN, two peaks, which are main diffraction peak appeared at 27.3° and a small peak appeared at 13.1° were indexed to the (100) and (200) planes of U-g-CN, respectively (Figure 4.3). The XRD patterns of the composites exhibited only the diffraction planes of U-g-CN, which indicated that U-g-CN was the only crystalline phase existing in all synthesized U-g-CN/WO_x composites. However, the relative diffraction intensity of U-g-CN decreased with increasing W content in the composites. As a reference sample, the XRD pattern of $Na_2WO_4.2H_2O$ precursor that was heated at 550 ºC for 4 hours was also shown in Figure 4.3. There was no peak attributed to Na_2WO_4 observable in the XRD patterns of U-g-CN/WO_x composites with the W content less than 10.3 wt%. The residual of Na_2WO_4 salt was removed from the 10.3% W loaded composites by washing with water. Furthermore, it is clearly observed that the diffraction peak for (002) plane of g-CN shifts to higher diffraction angles as the W loading percent was increased from 0.845 wt% to 10.3 wt%, corresponding to the shortened interplanar distance between the conjugated aromatic systems in U-g-CN. When the higher amount of Na, W, and O heteroatoms were impregnated into the U-g-CN framework, the interaction between the layers of U-g-CN becomes strengthened which results in lattice contraction in U-g-CN, which is well consistent with the literature.[156]

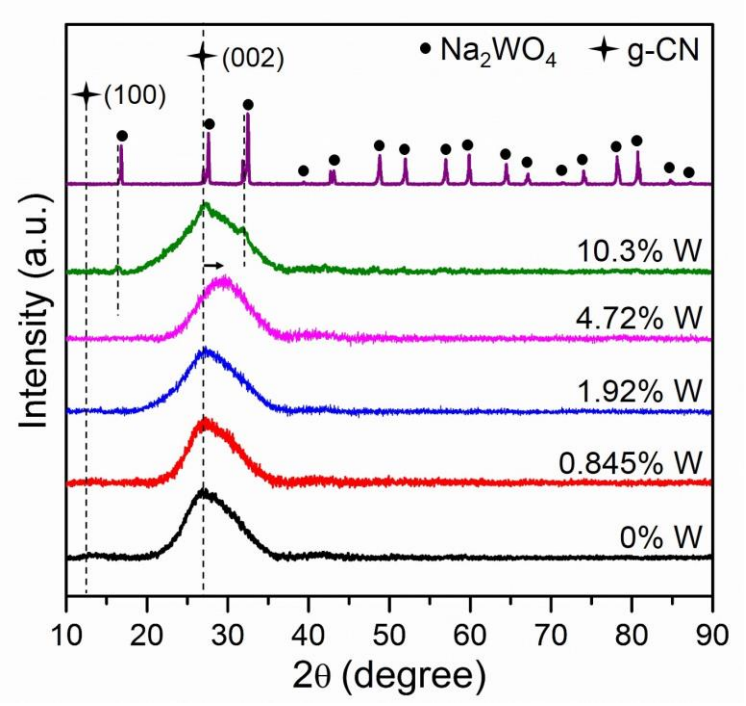

Figure 4.3: XRD patterns of U-g-CN/WO_x composites including 0, 0.845, 1.92, 4.72, 10.3 wt% W, and Na_2WO_4.

The element/chemical state information from the surface of U-g-CN/WO_x (4.72 wt% W) composite was acquired by XPS analysis. The XPS survey spectra of the samples confirmed the presence of C, N, O, and W elements (Figure 4.4a). The high-resolution XPS spectrum of C 1s region showed three major peaks at BEs of 284.5, 285.9, and 287.9 eV, which were attributed to C atoms in C−C or C = C functional groups, aromatic ring C coordinated to terminal amino groups of g-CN, and s-triazine aromatic ring C in g-CN, respectively (Figure 4.4b). In Figure 4.4c, XPS spectra of N 1s region displayed three major peaks at BEs of 398.5, 399.8, and 400.7 eV, which were referred to aromatic ring N, N connecting aromatic rings, and terminal amino group species in g-CN, respectively. A minor peak at 403.8 eV indicated the existence of –NO_x groups, which were also observable in N 1s spectra of both samples. The deconvoluted XPS spectrum of O 1s core-level of U-g-CN/WO_x (4.72 wt% W) composites displayed four peaks located at BEs of 530.5, 531.9, 533.2, and 535.3 eV (Figure 4.4d), which were readily assigned to the chemical binding states of O-W (lattice oxygen), O-vacancy, -OH, and adsorbed H_2O, respectively.[157] The W 4f XPS spectrum exhibited three pairs of doublet at BEs of 30.23 eV/ 32.93 eV, 33.83 eV /35.83 eV, and 34.93 eV /37.03 eV, indicating that the surface of the composite composed of W species in the oxidation state of W^0, W^{5+}, and W^{6+}, respectively (Figure 4.4e).[158], [159] Additionally, there was a satellite feature at BE of 40.23 eV indicating the presence of WO_3. As a result, it can be concluded that the surface of U-g-CN/WO_x (4.72 wt% W) composites mainly consist of fully oxidized WO_3 and partially reduced WO_{3-x} species at +5 and 0 oxidation states. The surface of the composites was also analyzed before (U-g-CN/WO_x/Pt(IV)) and after (U-g-CN/WO_x/Pt) the HAB reaction, and the obtained spectra was compared with the that of fresh composites. In Figure 4.5a, the W 4f XPS spectra of the U-g-CN/WO_x/Pt nanocatalysts after the HAB clearly revealed that the peak intensity ratio of W^{6+}/W^{5+} species partially reduced. The reducing environment of HAB caused the partial reduction of WO_3 species. It is also worth mentioning that the intensity of the W 4f peaks of U-g-CN/WO_x/Pt nanocatalyst was lower than that of U-g-CN/WO_x and U-g-CN/WO_x/Pt(IV) composites, which clearly indicating the removal of WO_x species from the surface of the composites during the HAB. In Figure 4.4b, Pt 4f XPS spectra of the samples before and after HAB reaction is illustrated. The Pt $4f_{7/2}$ peaks belonging to +4 and +2 oxidation states of Pt was observable for the U-g-CN/WO_x/Pt(IV) composites. After the reduction during the HAB, Pt $4f_{7/2}$ spectra of the obtained U-g-CN/WO_x/Pt nanocatalyst showed two asymmetric peaks attributed to metallic Pt and Pt^{2+}.

The peaks attributing to the U-g-CN/WO_x/Pt nanocatalyst had lower intensities compared to U-g-CN/WO_x/Pt(IV) composites due to the loss of Pt and WO_x species from the surface of the nanocatalysts during the reduction process. According to valence band XPS spectra shown in Fig. 4.4f, the valence band maxima of pristine U-g-CN and U-g-CN/WO_x (4.72 wt% W) composites were estimated to be 2.1 eV and 1.6 eV, respectively, indicating upper shift in the valence band structure with the construction of heterostructure between U-g-CN and WO_x species. According to the characterization results of the synthesized binary composites, the obtained wrinkled paper like tungsten oxides were found to be in non-crystalline phase and in multivalent oxidation states such that they were preferred to be called as a-WO_x species.

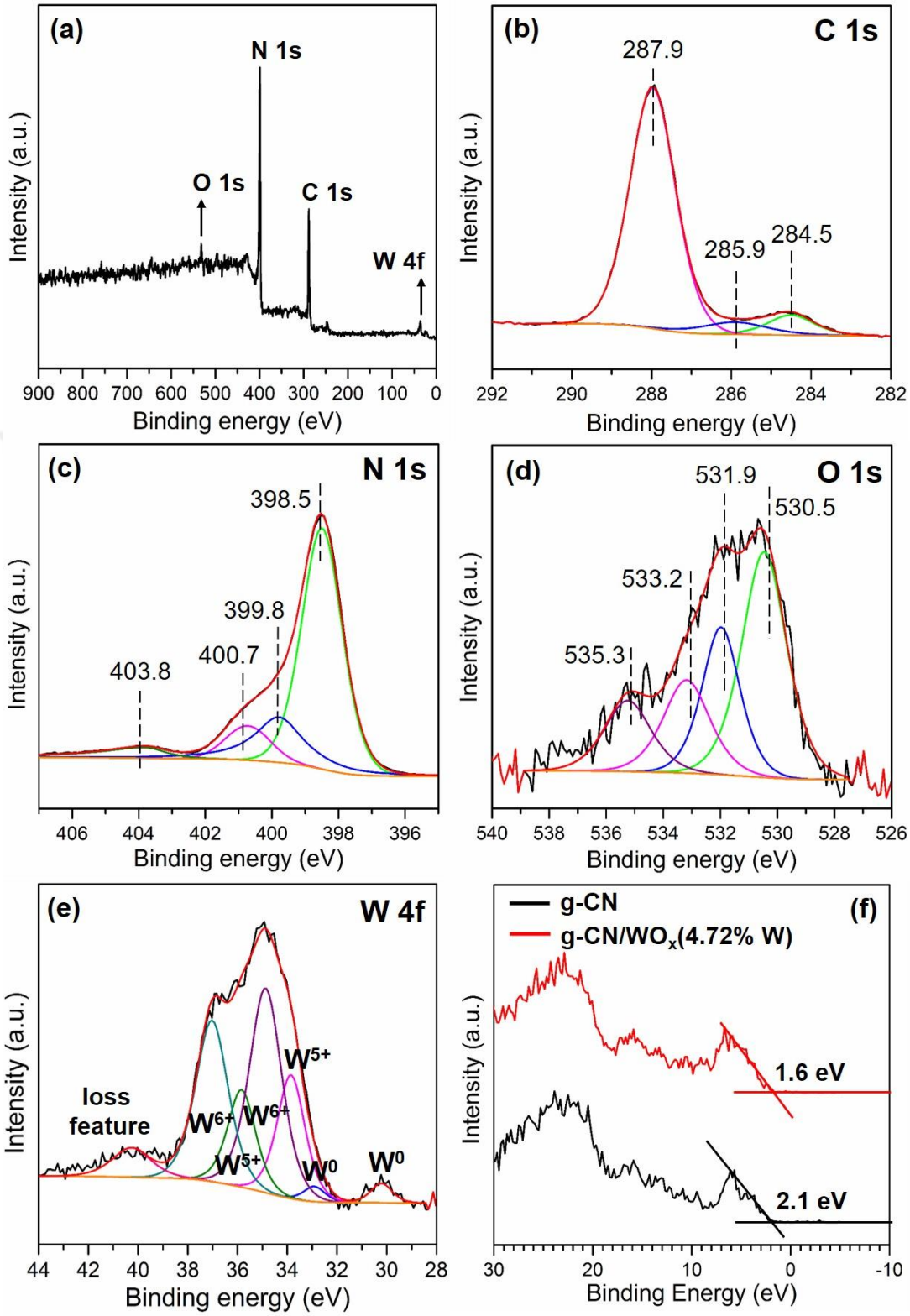

Figure 4.4: (a) XPS survey of U-g-CN/WO_x (4.72 wt% W), HR-XPS (b) C 1s, (c) N 1s, (d) O 1s, (e) W 4f spectra of U-g-CN/WO_x (4.72 wt% W), f) Valence band XPS spectra of g-CN and U-g-CN/WO_x (4.72 wt% W).

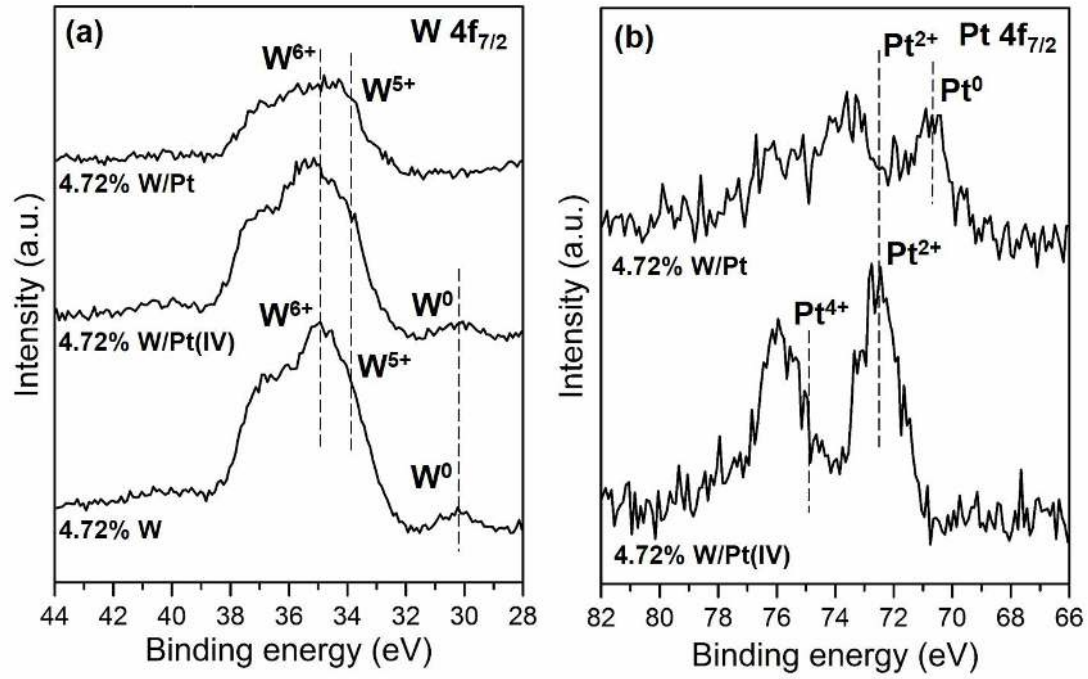

Figure 4.5: (a) XPS spectra of U-g-CN/WO_x (4.72 wt% W) composites before Pt ion addition, after Pt ion addition, and after AB reduction (labelled as 4.72% W, 4.72% W/Pt(IV), and 4.72% W/Pt, respectively), (a) W $4f_{7/2}$, (b) Pt $4f_{7/2}$.

The photophysical properties of pristine U-g-CN and U-g-CN/WO_x composites consisting of different amount of W were studied by UV-Vis diffuse reflectance spectroscopy (UV-vis-DRS), photoluminescence (PL), and time-resolved emission spectroscopy (TRES). First, the UV-vis-DRS spectra of all samples showed typical semiconductor absorption behavior in the visible region (Figure 4.6a). The composites exhibited higher absorption intensity compared to pristine U-g-CN and their adsorption wavelength shifted gradually to the longer wavelengths as the W content of the composites increased. Moreover, the color of the composites change from yellow to brown by increasing W loading, implying the modification of the optical properties of U-g-CN/WO_x composites.[160] In addition, the optical band gap energies (E_g) of pristine g-CN and U-g-CN/WO_x composites with 0.845, 1.92, 4.72, and 10.3 wt% W were estimated to be 2.78, 2.75, 2.72, 2.72, and 2.63 eV, respectively, by the interception of the tangents to the X-axis of Tauc's plot (Figure 4.6b). For the explanation of the mechanism behind the photocatalytic activity enhancement, the PL emission spectroscopy and time-resolved emission spectroscopy measurements were carried out. It is obvious from Figure 4.6c that the PL intensity of U-g-CN reduced gradually after incorporation of different amount of WO_x species indicating that the

separation of the photogenerated charges were greatly enhanced in the WO_x loaded nanocomposites compared to that in the bare U-g-CN. Furthermore, the lifetime of charge carriers was determined by TRES, which could be well fitted by following the bi-exponential decay model. As shown in Figure 4.6d, compared with the pristine U-g-CN (τ_{av} = 8.62 ns), the U-g-CN/WO_x composites showed much shorter lifetimes, which were calculated to be 7.76, 7.28, 7.02, and 5.37 ns for the composites having 0.845, 1.92, 4.72, and 10.3 wt% W, respectively. This result indicates the presence of effective electron transfer channels accelerating the flow of the electrons to the surface.[138] The lowered PL intensity and decreased average lifespan of the charges strongly supports the heterojunction construction between U-g-CN and WO_x components.

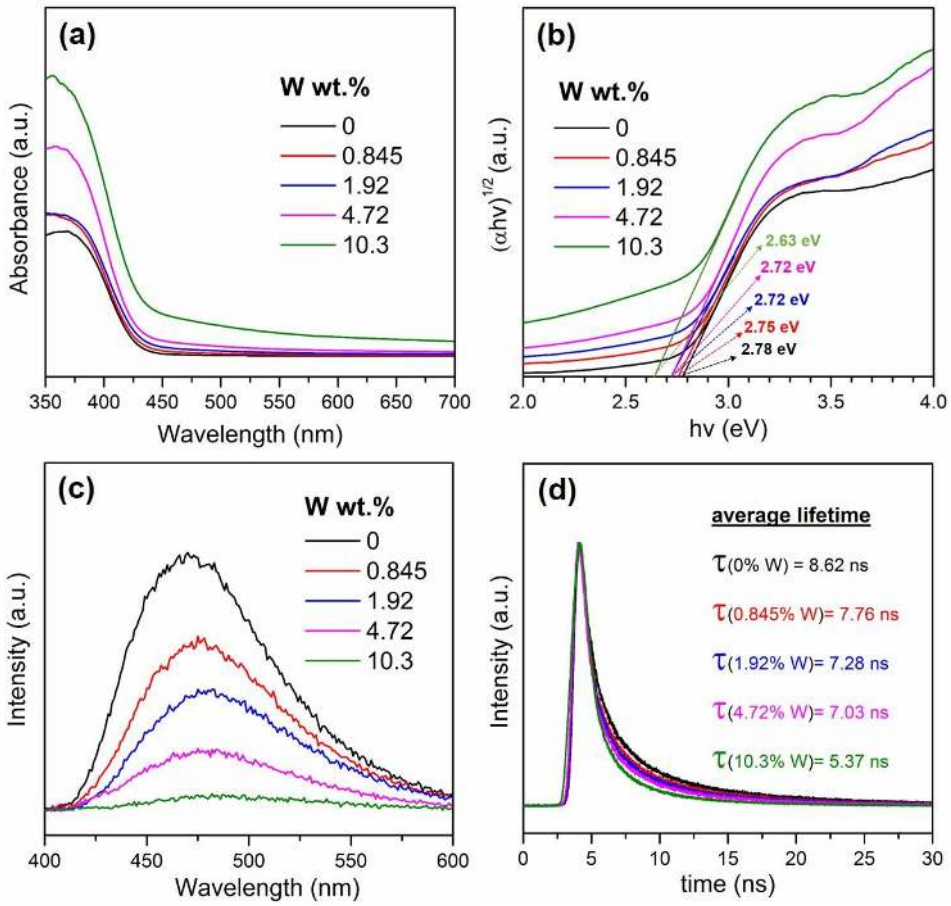

Figure 4.6: (a) UV-Vis Diffuse Reflectance spectra, (b) Tauc plot, (c) PL spectra, (d) Time-resolved emission spectra of U-g-CN and U-g-CN/WO_x nanocomposites consisting of 0.845, 1.92, 4.72, and 10.3 wt% W.

The photocatalytic activity of U-g-CN/WO_x/Pt nanocatalysts was investigated in hydrogen generation from the HAB. Firstly, the effect of light on the catalytic activity of U-g-CN/WO_x/Pt(IV) nanocomposites including 4.72 wt% W and 0.679 wt% Pt was shown in Figure 4.7. The hydrogen evolution rate was 4.8-times higher under the white light irradiation, supporting the formation of an effective heterojunction photocatalyst in the HAB. Afterwards, the effect of W loading in the U-g-CN/WO_x/Pt nanocatalysts was investigated (Figure 4.8). The maximum H_2 generation rate of 48.1 L H_2 g_{Pt}^{-1} min^{-1} was obtained by using the U-g-CN/WO_x/Pt nanocatalysts including 4.72 wt% W. As the W loading of the composite was increased from 4.72 wt% to 10.3 wt%, a sharp decrease from 48.1 to 15.0 L H_2 g_{Pt}^{-1} min^{-1} in the photocatalytic hydrogen production rate was observed. Even though the efficiency of charge separation along with lifetime of the charges improved in the 10.3 wt% W loaded nanocatalysts as shown in Figure 4.6c, the reason behind the decrease of the photocatalytic activity might be due to the existence of Na_2WO_4 residuals on the surface which might hinder the interaction between the surface-active sites and reactant species.

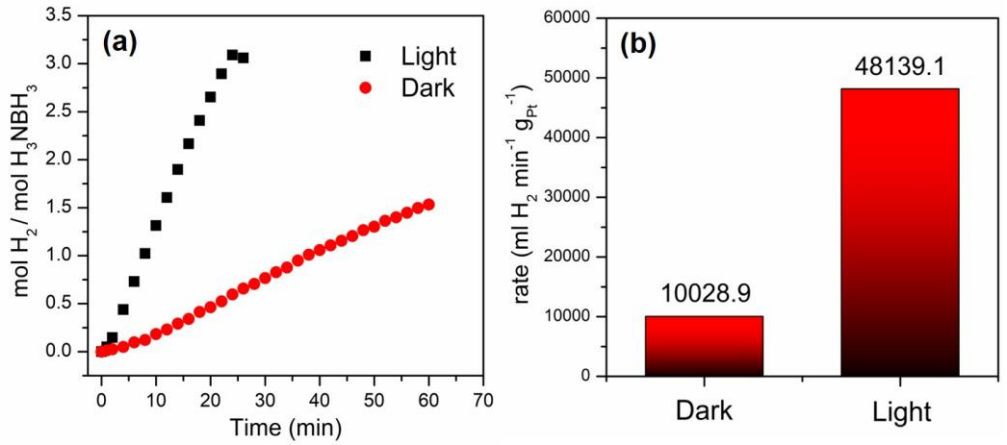

Figure 4.7: (a) Time versus mol H_2/mol H_3NBH_3 plots for the U-g-CN/WO_x/Pt (4.72 wt% W) catalyzed HAB conducted in the dark and under white-light irradiation, (b) H_2 production rate for each condition.

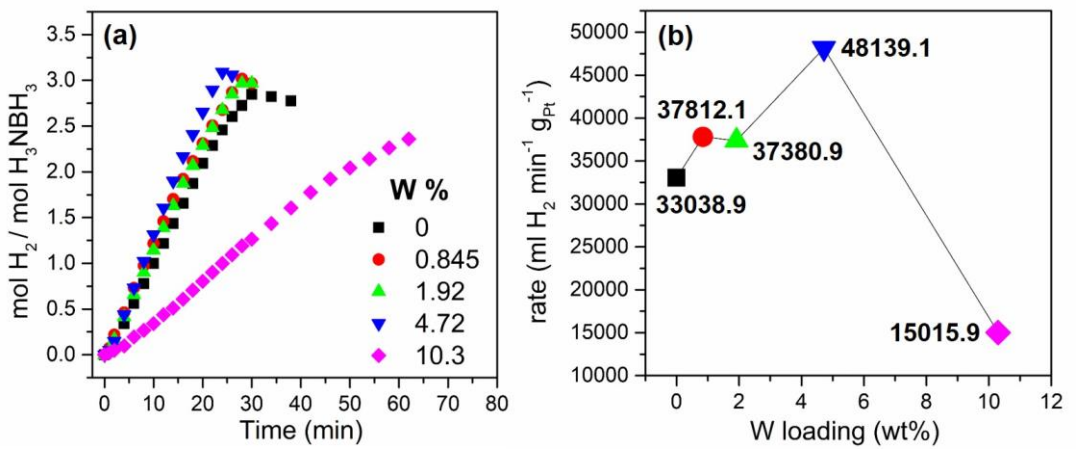

Figure 4.8: (a) Time versus mol H_2/mol H_3NBH_3 plots of the U-g-CN/WO_x/Pt nanocatalysts with different content (0, 0.845, 1.92, 4.72, and 10.3) of W, (b) H_2 production rate (mL H_2 g_{Pt}^{-1} min^{-1}) comparison of the corresponding catalysts.

According to the results of the kinetic studies, the HAB in the presence of U-g-CN/WO_x/Pt nanocatalysts proceeded via first-order with respect to the Pt concentration and zeroth-order with respect to the AB concentration. As a result, the rate law can be written as rate = k_{obs}[Pt] for the HAB in the presence of U-g-CN/WO_x/Pt (4.72 wt% W) nanocatalysts (Figure 4.9a-d). Additionally, the rate constants, k_{obs} (the values of k_{obs} are shown in Table A3, see Appendix A), calculated by inserting the reaction rates for each temperature into the rate law, were used to draw Arrhenius Plot (ln k_{obs} versus 1/T). And, from the slope of Arrhenius Plot, the apparent activation energy (E_{app}) was found to be 76.9 kJ/mol^{-1} (Figure 4.9e-f).

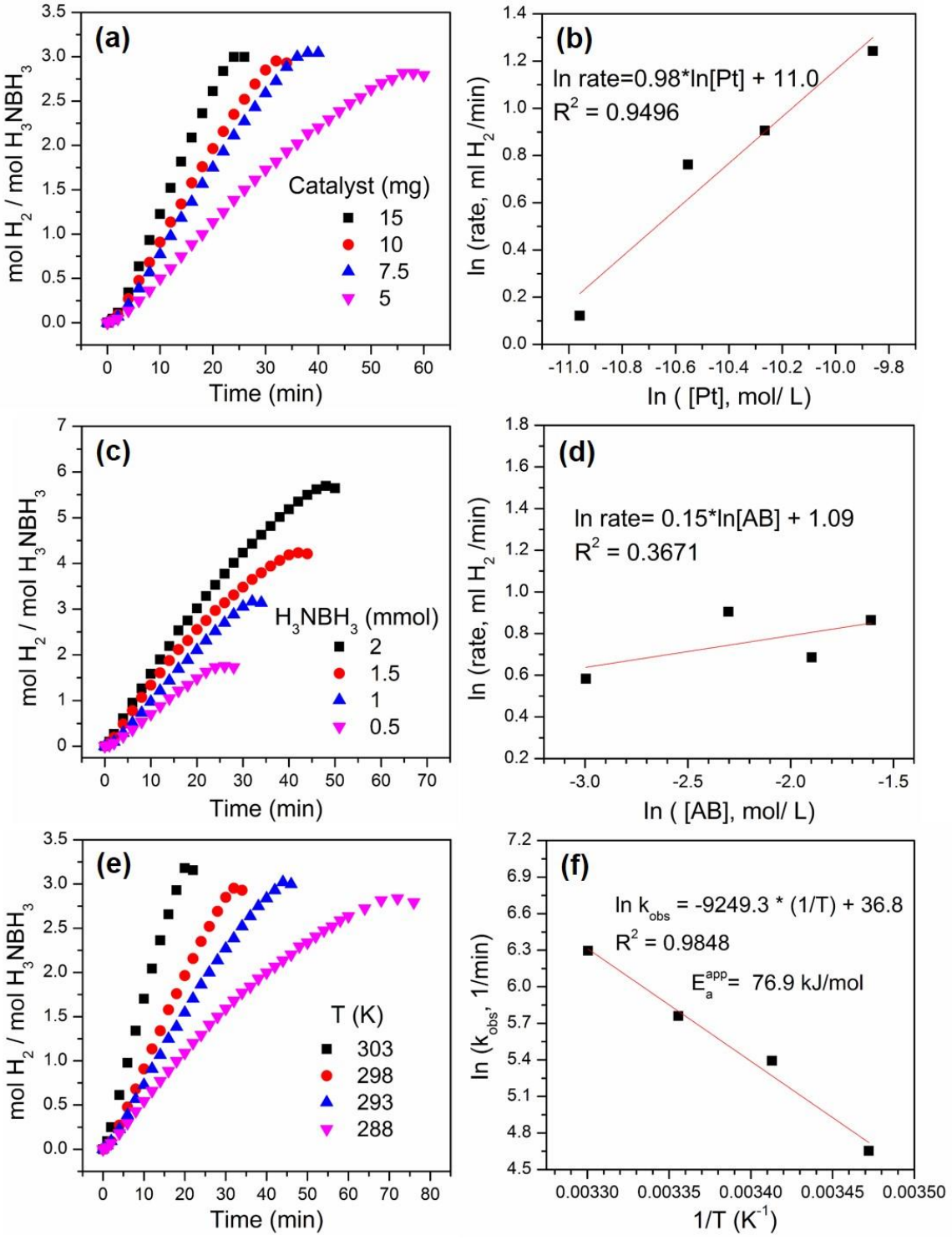

Figure 4.9: Time versus mol H_2/mol H_3NBH_3 plots for the U-g-CN/WO_x/Pt (4.72 wt% W) catalyzed HAB reaction at different reaction conditions including (a) [AB] = 0.1 M, T = 25 °C, and [Pt] = 0.0174 −0.0522 mM, (c) [Pt] = 0.0348 mM, T= 25 °C, and [AB] = 0.05-0.2 M, (e) [AB] = 0.1 M, [Pt] = 0.0348 mM, and T = 288-303 K; logarithmic plots of H_2 production rate versus (b) Pt concentration, (d) AB concentration, (f) Arrhenius plot of ln k_{obs} versus 1/T.

The reusability experiments revealed that U-g-CN/WO_x/Pt (4.72 wt% W) nanocatalysts preserved only 32.1% of its initial hydrogen production (L H_2 min^{-1}) after three consecutive runs. TEM image of the U-g-CN/WO_x/Pt nanocatalysts after the 3rd run, which is shown in the Figure 4.10b, illustrates that there are some agglomerated Pt NPs observable on U-g-CN/WO_x composites, which might be attributed to the decrease in activity along with the sample loss during washing procedure. Moreover, the U-g-CN/WO_x/Pt nanocatalysts did not have enough resistant to reduction environment created by AB such that the loss of W and Pt was observed even after 1st run, as depicted by the peak intensity decrease in the W $4f_{7/2}$ and Pt $4f_{7/2}$ XPS spectra of U-g-CN/WO_x/Pt (Figure 4.5a). When we combine this observation with the decrease in the activity even after first run, the role of W in the heterostructure along with Pt species is becoming more pronounced in order to enhance catalytic activity.

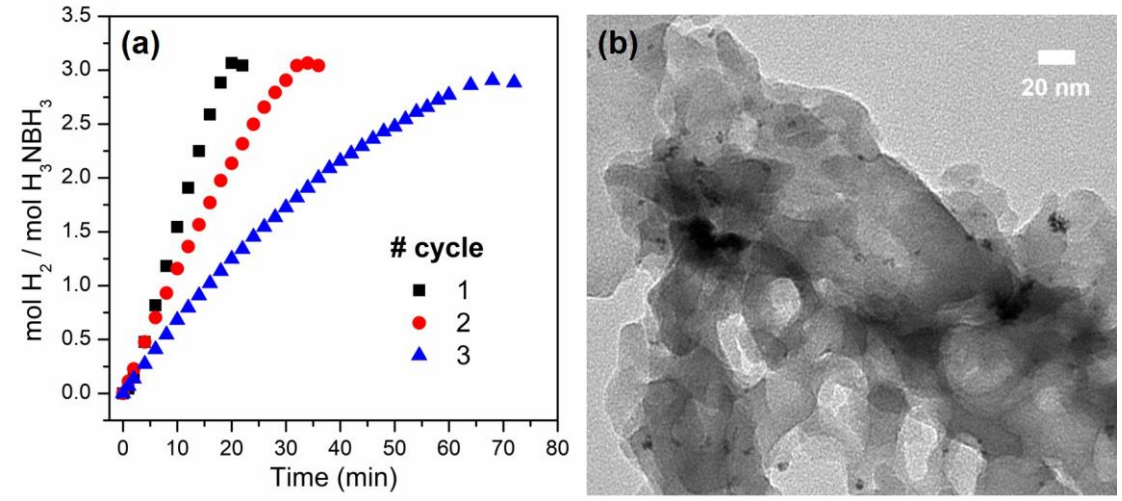

Figure 4.10: (a) H_2 generation versus time catalyzed by U-g-CN/WO_x/Pt (4.72 wt% W) nanocatalysts during a 3-run reusability test, (b) TEM image of the nanocatalyst after 3rd run.

Chapter 5

CONCLUSION

As a summary, this dissertation addressing the development of highly efficient Pt nanocatalysts for the HAB via rational design of g-CN based heterojunctions has led to some significant conclusions and insights as followings:

Part 1: m-g-CN/Pt nanocatalysts for the HAB

- m-g-CN served both as a stabilizer and semiconductor support material for the in-situ growth of Pt NPs during HAB reaction. Thanks to the formation of Schottky barrier at the interface between m-g-CN and Pt NPs, the recovery of the charge recombination along with prolonged lifetime of the charges were achieved.
- The stability effect of m-g-CN was mainly explained according to Pt 4f and N 1s HR-XPS spectra of m-g-CN/Pt (3.82 wt% Pt) nanocatalysts, implying that complete reduction of Pt ions cannot be achieved even after 10^{th} times reduction due to the formation of stable Pt complexes as the result of their interaction with the surface functional groups of m-g-CN.
- The catalytic activity of Pt NPs in the HAB was improved under white-light illumination owing to the photocatalysis, which was in accordance with the characterization results. This enhancement was around 2.25-fold for the m-g-CN/Pt (2.95 wt% Pt) nanocatalysts, and the hydrogen production rate reaching up to 31.5 and 23.3 L H_2 g_{Pt}^{-1} min^{-1} were provided by the most active m-g-CN/Pt nanocatalysts including 5.94 and 3.82 wt% Pt, respectively.
- The kinetic studies on m-g-CN/Pt (3.82 wt% Pt) nanocatalysts illustrated that HAB reaction progresses via first-order law according to Pt concentration and via zeroth-order law according to AB concentration. The E_{app} was found to be 40.7 kJ mol^{-1} for HAB.
- The excellent reusability of m-g-CN/Pt (3.82 wt% Pt) nanocatalysts, which maintained 78% of its initial activity after 10^{th} cycle, was also attributed to the stabilizer effect of m-g-CN.
- All the represented data in part-1 was published as a full paper in ACS Applied Nano Materials (2020, 3 (7), 6836-6846).[115]

Part 2: U-g-CN/MPt nanocatalysts for the HAB

- The photocatalytic activity of m-g-CN/Pt (3.82 wt% Pt) nanocatalysts in HAB was further enhanced from 23.3 to 44.3 L H_2 g_{Pt}^{-1} min^{-1} with the introduction of U-g-CN as a support material instead of m-g-CN. The reason behind this enhancement was attributed to the improved charge kinetics of U-g-CN compared to m-g- CN. Besides, the morphological differences between two support materials were found very effective on the dispersion and average particle size of the in-situ generated Pt NPs such that it was calculated to be 2.6 nm for the Pt NPs loaded on U-g-CN, which was slightly lower than the ones on m-g-CN (3.5 nm).
- Bimetallic AuPt, AgPt, and CuPt NPs deposited on U-g-CN were synthesized in-situ during the HAB and only U-g-CN/$Pt_{92}Au_8$ and U-g-CN/$Pt_{85}Au_{15}$ nanocatalysts showed higher catalytic activity compared to their monometallic counterpart, U-g-CN/Pt_{100}, under white LED illumination Therefore, the photocatalytic activity was further enhanced to 67.4 and 68.9 L H_2 g_{Pt}^{-1} min^{-1} in the presence of U-g-CN/$Pt_{85}Au_{15}$ and U-g-CN/$Pt_{92}Au_8$ nanocatalysts, respectively, compared to the hydrogen generation rate of 60.4 L H_2 g_{Pt}^{-1} min^{-1} for U-g-CN/Pt_{100}.
- The alloy formation between Pt and Au metals in $Pt_{92}Au_8$ NPs were demonstrated with the HRTEM and elemental mapping analyses, which were concluded by the calculated lattice distance of 0.228 nm for a single $Pt_{92}Au_8$ NP and homogenously distribution of both Pt and Au elements in $Pt_{92}Au_8$ NPs.
- The synergistic effect between two metals mainly caused by the electronic interaction between two metals were supported by Pt 4f and Au 4f HR-XPS spectra, which shows slightly shifting to lower binding energy values in both spectra.
- The improved charge kinetics of U-g-CN/PtAu nanocatalysts imply the presence of effective electron transfer channels from U-g-CN to the mono/bimetallic Pt NPs. Along with the alloying effect between Au and Pt metal, the plasmonic effect of Au metal that might be causing flow of electrons to Pt can generate electron enriched active Pt sites, leading to higher H_2 generation activities in U-g-CN/PtAu case.
- The kinetic studies on U-g-CN/$Pt_{92}Au_8$ nanocatalysts shows that HAB reaction follows first-order kinetics according to Pt concentration and zeroth-order kinetics according to AB concentration. The E_{app} was calculated to be 52.7 kJ mol^{-1} for HAB which was slightly larger than that of m-g-CN/Pt nanocatalysts.

- The U-g-CN/$Pt_{92}Au_8$ nanocatalysts can only maintain 35% of its initial hydrogen production (L H_2 min^{-1}) due to some observable agglomerates along with the loss of catalyst amount during washing/drying process.

Part 3: U-g-CN/a-WOx/Pt nanocatalysts for the HAB

- To eliminate the drawbacks of U-g-CN such as having high recombination rate of photogenerated electron-hole pairs, U-g-CN/WO_x heterojunctions were aimed to use as a support material for the in-situ generation of Pt NPs.
- The wrinkled paper-like WO_x species homogenously distributed in the composite structure were found to be in non-crystalline phase since the absence of crystalline phase peaks belong to WO_x was confirmed by XRD results even for the U-g-CN/WO_x composition including 10.3 wt% W.
- XPS analysis of U-g-CN/a-WO_x indicated that W atoms were in multiple oxidation states (W^0, W^{5+}, and W^{6+}).
- WO_x species were partially reduced and leave the surface of nanocatalysts along with Pt during HAB due to the observed peak intensity change in W 4f XPS before and after HAB.
- The increase in the hydrogen evolution rate under white light irradiation, which was 4.8 times compared to that in dark, clearly clarify the construction of more effective Schottky junction between U-g-CN/a-WO_x nanocomposites and Pt NPs compared to one formed between m-g-CN and Pt NPs.
- The maximum H_2 generation rate of 48.1 L H_2 g_{Pt}^{-1} min^{-1} was obtained by using 4.72 wt% W loaded U-g-CN/a-WO_x/Pt nanocatalysts is, which was significantly higher than that of U-g-CN/Pt (33.0 L H_2 g_{Pt}^{-1} min^{-1}). The enhanced charge kinetics, absorption abilities, and decrease in band gap of U-g-CN/a-WO_x heterojunctions were the main reasons behind the significant role of amorphous WO_x in photocatalytic HAB.
- The kinetic studies on U-g-CN/a-WO_x/Pt nanocatalysts demonstrated that HAB was first-order reaction with respect to the Pt concentration and zeroth-order reaction with respect to the AB concentration. And, E_{app} was found to be 76.9 kJ mol^{-1}, which is larger than that of m-g-CN/Pt and U-g-CN/$Pt_{92}Au_8$ nanocatalysts.
- U-g-CN/a-WO_x/Pt nanocatalysts keep only 32.1% its initial hydrogen production (L H_2 g_{Pt}^{-1} min^{-1}), which made it less durable and stable among all mentioned nanocatalysts until now even though it showed more pronounced heterojunction effect.

- Due to the loss of some a-WO_x species along with Pt from surface of the nanocatalysts during the hydrolysis reaction, which might be the most important reason of the decrease in the reusability activity, the role of a-WO_x in enhanced photocatalytic activity became more significant.

All the g-CN based heterojunction Pt nanocatalysts tested in the photocatalytic HAB were summarized in Table 5.1, including their hydrogen production rate, kinetic data, and reusability results.

Table 5.1: Summary of the hydrogen generation from the HAB catalyzed by Pt and g-CN based heterojunction photocatalysts.

Metal Catalyst	rate ($L\ H_2\ g_{Pt}^{-1}\ min^{-1}$) @ 25 °C	Ea (kJ/mol)	Cycle number	Maintaining initial Catalytic Activity
m-g-CN/Pt (5.94 wt% Pt)	31.5	-	-	-
m-g-CN/Pt (3.82 wt% Pt)	23.3	40.7	10	78% ($L\ H_2\ g_{Pt}^{-1}\ min^{-1}$)
U-g-CN/$Pt_{92}Au_8$	68.9	52.7	5	35% ($L\ H_2\ min^{-1}$)
U-g-CN/$Pt_{85}Au_{15}$	67.4	-	-	-
U-g-CN/Pt_{100}	60.4	-	-	-
U-g-CN/a-WO_x/Pt (4.72 wt% W)	48.1	76.9	3	32% ($L\ H_2\ min^{-1}$)

Considering the whole thesis work, this thesis contributes to the hydrogen energy, photocatalysis, and other related fields via representing the construction of Pt and g-CN based heterojunctions for more effective hydrogen production from HAB to manage with the H_2 energy storage problems.

BIBLIOGRAPHY

(1) Martins, F.; Felgueiras, C.; Smitkova, M.; Caetano, N. Analysis of Fossil Fuel Energy Consumption and Environmental Impacts in European Countries. *Energies* **2019**, *12* (6), 964. https://doi.org/10.3390/en12060964.

(2) Wu, F.; Maier, J.; Yu, Y. Guidelines and Trends for Next-Generation Rechargeable Lithium and Lithium-Ion Batteries. *Chemical Society Reviews*. Royal Society of Chemistry March 7, 2020, pp 1569–1614. https://doi.org/10.1039/c7cs00863e.

(3) AL Shaqsi, A. Z.; Sopian, K.; Al-Hinai, A. Review of Energy Storage Services, Applications, Limitations, and Benefits. *Energy Reports*. Elsevier Ltd December 1, 2020, pp 288–306. https://doi.org/10.1016/j.egyr.2020.07.028.

(4) Helen McCay, M. Hydrogen. An Energy Carrier. In *Future Energy: Improved, Sustainable and Clean Options for our Planet*; Elsevier Inc., 2013; pp 495–510. https://doi.org/10.1016/B978-0-08-099424-6.00023-5.

(5) Sinsel, S. R.; Riemke, R. L.; Hoffmann, V. H. Challenges and Solution Technologies for the Integration of Variable Renewable Energy Sources—a Review. *Renewable Energy*. Elsevier Ltd January 1, 2020, pp 2271–2285. https://doi.org/10.1016/j.renene.2019.06.147.

(6) Pareek, A.; Dom, R.; Gupta, J.; Chandran, J.; Adepu, V.; Borse, P. H. Insights into Renewable Hydrogen Energy: Recent Advances and Prospects. *Mater. Sci. Energy Technol.* **2020**, *3*, 319–327. https://doi.org/10.1016/j.mset.2019.12.002.

(7) Hosseini, S. E.; Butler, B. An Overview of Development and Challenges in Hydrogen Powered Vehicles. *International Journal of Green Energy*. Taylor and Francis Inc. January 2, 2020, pp 13–37. https://doi.org/10.1080/15435075.2019.1685999.

(8) Eberle, U.; Felderhoff, M.; Schüth, F. Chemical and Physical Solutions for Hydrogen Storage. *Angew. Chemie Int. Ed.* **2009**, *48* (36), 6608–6630. https://doi.org/10.1002/anie.200806293.

(9) Ramirez-Vidal, P.; Canevesi, R. L. S.; Sdanghi, G.; Schaefer, S.; Maranzana, G.; Celzard, A.; Fierro, V. A Step Forward in Understanding the Hydrogen Adsorption and Compression on Activated Carbons. *ACS Appl. Mater. Interfaces* **2021**, *13* (10), 12562–12574. https://doi.org/10.1021/acsami.0c22192.

(10) Jain, V.; Kandasubramanian, B. Functionalized Graphene Materials for Hydrogen Storage. *Journal of Materials Science*. Springer February 1, 2020, pp 1865–1903. https://doi.org/10.1007/s10853-019-04150-y.

(11) Anikina, E.; Banerjee, A.; Beskachko, V.; Ahuja, R. Li-Functionalized Carbon Nanotubes for Hydrogen Storage: Importance of Size Effects. *ACS Appl. Nano Mater.* **2019**, *2* (5), 3021–3030. https://doi.org/10.1021/acsanm.9b00406.

(12) Dong, J.; Wang, X.; Xu, H.; Zhao, Q.; Li, J. Hydrogen Storage in Several Microporous Zeolites. *Int. J. Hydrogen Energy* **2007**, *32* (18), 4998–5004. https://doi.org/10.1016/j.ijhydene.2007.08.009.

(13) Shet, S. P.; Shanmuga Priya, S.; Sudhakar, K.; Tahir, M. A Review on Current Trends in Potential Use of Metal-Organic Framework for Hydrogen Storage. *International Journal of Hydrogen Energy*. Elsevier Ltd March 23, 2021, pp 11782–11803. https://doi.org/10.1016/j.ijhydene.2021.01.020.

(14) Hwang, H. T.; Varma, A. Hydrogen Storage for Fuel Cell Vehicles. *Current Opinion in Chemical Engineering*. Elsevier Ltd August 1, 2014, pp 42–48. https://doi.org/10.1016/j.coche.2014.04.004.

(15) Kayfeci, M.; Keçebaş, A. Hydrogen Storage. In *Solar Hydrogen Production: Processes, Systems and Technologies*; Elsevier, 2019; pp 85–110. https://doi.org/10.1016/B978-0-12-814853-2.00004-7.

(16) Møller, K. T.; Jensen, T. R.; Akiba, E.; Li, H. wen. Hydrogen - A Sustainable Energy Carrier. *Prog. Nat. Sci. Mater. Int.* **2017**, *27* (1), 34–40. https://doi.org/10.1016/j.pnsc.2016.12.014.

(17) Kumar, P.; Singh, S.; Hashmi, S. A. R.; Kim, K. H. MXenes: Emerging 2D Materials for Hydrogen Storage. *Nano Energy*. Elsevier Ltd July 1, 2021, p 105989. https://doi.org/10.1016/j.nanoen.2021.105989.

(18) Modisha, P. M.; Ouma, C. N. M.; Garidzirai, R.; Wasserscheid, P.; Bessarabov, D. The Prospect of Hydrogen Storage Using Liquid Organic Hydrogen Carriers. *Energy and Fuels*. American Chemical Society April 18, 2019, pp 2778–2796. https://doi.org/10.1021/acs.energyfuels.9b00296.

(19) Mellmann, D.; Sponholz, P.; Junge, H.; Beller, M. Formic Acid as a Hydrogen Storage Material-Development of Homogeneous Catalysts for Selective Hydrogen Release. *Chemical Society Reviews*. Royal Society of Chemistry July 21, 2016, pp 3954–3988. https://doi.org/10.1039/c5cs00618j.

(20) Wu, H.; Cheng, Y.; Fan, Y.; Lu, X.; Li, L.; Liu, B.; Li, B.; Lu, S. Metal-Catalyzed Hydrolysis of Ammonia Borane: Mechanism, Catalysts, and Challenges. *Int. J. Hydrogen Energy* **2020**, *45* (55), 30325–30340. https://doi.org/10.1016/j.ijhydene.2020.08.131.

(21) Demirci, U. B. Ammonia Borane, a Material with Exceptional Properties for Chemical Hydrogen Storage. *Int. J. Hydrogen Energy* **2017**, *42* (15), 9978–10013. https://doi.org/10.1016/j.ijhydene.2017.01.154.

(22) Liu, M.; Zhou, L.; Luo, X.; Wan, C.; Xu, L. Recent Advances in Noble Metal Catalysts for Hydrogen Production from Ammonia Borane. *Catalysts* **2020**, *10* (7), 1–34. https://doi.org/10.3390/catal10070788.

(23) Demirci, U. B. Ammonia Borane: An Extensively Studied, Though Not yet Implemented, Hydrogen Carrier. *Energies* **2020**, *13* (12). https://doi.org/10.3390/en13123071.

(24) Sanyal, U.; Demirci, U. B.; Jagirdar, B. R.; Miele, P. Hydrolysis of Ammonia Borane as a Hydrogen Source: Fundamental Issues and Potential Solutions towards Implementation. *ChemSusChem* **2011**, *4* (12), 1731–1739. https://doi.org/10.1002/cssc.201100318.

(25) Chandra, M.; Xu, Q. Dissociation and Hydrolysis of Ammonia-Borane with Solid Acids and Carbon Dioxide: An Efficient Hydrogen Generation System. *J. Power Sources* **2006**, *159* (2), 855–860. https://doi.org/10.1016/j.jpowsour.2005.12.033.

(26) Chandra, M.; Xu, Q. Room Temperature Hydrogen Generation from Aqueous Ammonia-Borane Using Noble Metal Nano-Clusters as Highly Active Catalysts. *J. Power Sources* **2007**, *168* (1 SPEC. ISS.), 135–142. https://doi.org/10.1016/j.jpowsour.2007.03.015.

(27) Xu, Q.; Chandra, M. Catalytic Activities of Non-Noble Metals for Hydrogen Generation from Aqueous Ammonia-Borane at Room Temperature. *J. Power Sources* **2006**, *163* (1 SPEC. ISS.), 364–370. https://doi.org/10.1016/j.jpowsour.2006.09.043.

(28) Yang, X.; Cheng, F.; Tao, Z.; Chen, J. Hydrolytic Dehydrogenation of Ammonia Borane Catalyzed by Carbon Supported Co Core-Pt Shell Nanoparticles. *J. Power Sources* **2011**, *196* (5), 2785–2789. https://doi.org/10.1016/j.jpowsour.2010.09.079.

(29) Fu, Z. C.; Xu, Y.; Chan, S. L. F.; Wang, W. W.; Li, F.; Liang, F.; Chen, Y.; Lin, Z. S.; Fu, W. F.; Che, C. M. Highly Efficient Hydrolysis of Ammonia Borane by Anion (-OH, F-, Cl-)-Tuned Interactions between Reactant Molecules and CoP Nanoparticles. *Chem. Commun.* **2017**, *53* (4), 705–708. https://doi.org/10.1039/c6cc08120g.

(30) Wu, H.; Wu, M.; Wang, B.; Yong, X.; Liu, Y.; Li, B.; Liu, B.; Lu, S. Interface Electron Collaborative Migration of Co–Co3O4/Carbon Dots: Boosting the Hydrolytic Dehydrogenation of Ammonia Borane. *J. Energy Chem.* **2020**, *48*, 43–53. https://doi.org/10.1016/j.jechem.2019.12.023.

(31) Hou, C. C.; Li, Q.; Wang, C. J.; Peng, C. Y.; Chen, Q. Q.; Ye, H. F.; Fu, W. F.; Che, C. M.; López, N.; Chen, Y. Ternary Ni-Co-P Nanoparticles as Noble-Metal-Free Catalysts to Boost the Hydrolytic Dehydrogenation of Ammonia-Borane. *Energy Environ. Sci.* **2017**, *10* (8), 1770–1776. https://doi.org/10.1039/c7ee01553d.

(32) Wang, C.; Tuninetti, J.; Wang, Z.; Zhang, C.; Ciganda, R.; Salmon, L.; Moya, S.; Ruiz, J.; Astruc, D. Hydrolysis of Ammonia-Borane over Ni/ZIF-8 Nanocatalyst: High Efficiency, Mechanism, and Controlled Hydrogen Release. *J. Am. Chem. Soc.* **2017**, *139* (33), 11610–11615. https://doi.org/10.1021/jacs.7b06859.

(33) Wei, Z.; Liu, Y.; Peng, Z.; Song, H.; Liu, Z.; Liu, B.; Li, B.; Yang, B.; Lu, S. Cobalt-Ruthenium Nanoalloys Parceled in Porous Nitrogen-Doped Graphene as Highly Efficient Difunctional Catalysts for Hydrogen Evolution Reaction and Hydrolysis of Ammonia Borane. *ACS Sustain. Chem. Eng.* **2019**, *7* (7), 7014–7023. https://doi.org/10.1021/acssuschemeng.8b06745.

(34) Akbayrak, S.; Çakmak, G.; Öztürk, T.; Özkar, S. Rhodium(0), Ruthenium(0) and Palladium(0) Nanoparticles Supported on Carbon-Coated Iron: Magnetically Isolable and Reusable Catalysts for Hydrolytic Dehydrogenation of Ammonia Borane. *Int. J. Hydrogen Energy* **2021**, *46* (25), 13548–13560. https://doi.org/10.1016/j.ijhydene.2020.02.023.

(35) Cheng, W.; Peng, Y.; Wang, Y.; Jiang, W.; Long, Y.; Fan, G. Amino-Group and Space-Confinement Assisted Synthesis of Small and Well-Defined Rh Nanoparticles as Efficient Catalysts toward Ammonia Borane Hydrolysis. *Int. J. Hydrogen Energy* **2021**, *46* (2), 2204–2212. https://doi.org/10.1016/j.ijhydene.2020.10.140.

(36) Chen, Y.; Chen, Q.; Fan, G. Smart Construction of Oxidized-Ti3C2TX Stabilized Rh Nanoparticles for Remarkable Improving the Catalytic Performance for Ammonia Borane Hydrolysis. *Int. J. Hydrogen Energy* **2020**, *45* (53), 28812–28820. https://doi.org/10.1016/j.ijhydene.2020.07.255.

(37) Qiu, X.; Liu, J.; Qiu, S.; Huang, P.; Chu, H.; Zou, Y.; Zhang, H.; Xu, F.; Sun, L. Hydrogen Generation from Ammonia Borane Hydrolysis Catalyzed by Ruthenium Nanoparticles Supported on Co–Ni Layered Double Oxides. *Sustain. Energy Fuels* **2021**. https://doi.org/10.1039/d1se00079a.

(38) Qiu, X.; Liu, J.; Huang, P.; Qiu, S.; Weng, C.; Chu, H.; Zou, Y.; Xiang, C.; Xu, F.; Sun, L. Hydrolytic Dehydrogenation of NH 3 BH 3 Catalyzed by Ruthenium Nanoparticles Supported on Magnesium-Aluminum Layered Double-Hydroxides. **2020**. https://doi.org/10.1039/d0ra01720e.

(39) Deka, J. R.; Saikia, D.; Hsia, K.-S.; Kao, H.-M.; Yang, Y.-C.; Chen, C.-S. Ru Nanoparticles Embedded in Cubic Mesoporous Silica SBA-1 as Highly Efficient Catalysts for Hydrogen Generation from Ammonia Borane. https://doi.org/10.3390/catal10030267.

(40) Akbayrak, S.; Özkar, S. Cobalt Ferrite Supported Platinum Nanoparticles: Superb Catalytic Activity and Outstanding Reusability in Hydrogen Generation from the Hydrolysis of Ammonia Borane. *J. Colloid Interface Sci.* **2021**, *596*, 100–107. https://doi.org/10.1016/j.jcis.2021.03.039.

(41) Miao, H.; Ma, K.; Zhu, H.; Yin, K.; Zhang, Y.; Cui, Y. Ammonia Borane Dehydrogenation and Selective Hydrogenation of Functionalized Nitroarene over a Porous Nickel-Cobalt Bimetallic Catalyst. *RSC Adv.* **2019**, *9* (26), 14580–14585. https://doi.org/10.1039/c9ra01551e.

(42) Guo, K.; Ding, Y.; Luo, J.; Gu, M.; Yu, Z. NiCu Bimetallic Nanoparticles on Silica Support for Catalytic Hydrolysis of Ammonia Borane: Composition-Dependent Activity and Support Size Effect. *ACS Appl. Energy Mater.* **2019**, *2* (8), 5851–5861. https://doi.org/10.1021/acsaem.9b00997.

(43) Yang, X.; Li, Q.; Li, L.; Lin, J.; Yang, X.; Yu, C.; Liu, Z.; Fang, Y.; Huang, Y.; Tang, C. CuCo Binary Metal Nanoparticles Supported on Boron Nitride Nanofibers as Highly Efficient Catalysts for Hydrogen Generation from Hydrolysis of Ammonia Borane. *J. Power Sources* **2019**, *431*, 135–143. https://doi.org/10.1016/j.jpowsour.2019.05.038.

(44) Du, X.; Tai, Y.; Liu, H.; Zhang, J.; Su, M.; Li, F.; Wang, S. Highly Dispersed CuNi Nanoparticles Supported on Reduced Graphene Oxide as Eflcient Catalysts for Hydrogen Generation from NH3BH3. *Zeitschrift fur Phys. Chemie* **2020**, *234* (10), 1645–1659. https://doi.org/10.1515/zpch-2018-1317.

(45) Li, Y.; Li, S. Low-Cost CuFeCo@MIL-101 as an Efficient Catalyst for Catalytic Hydrolysis of Ammonia Borane. *Int. J. Hydrogen Energy* **2020**, *45* (17), 10433–10441. https://doi.org/10.1016/j.ijhydene.2019.06.075.

(46) Mahyari, M.; Gavgani, J. N.; Hasani, A.; Kim, J. K.; Kim, S. Y. Monodisperse Copper Nanoparticles on Porphyrin-Derived Fe-N-Doped Carbon for Hydrogen Generation from Ammonia Borane. *Sci. Adv. Mater.* **2017**, *9* (9), 1572–1577. https://doi.org/10.1166/sam.2017.3174.

(47) Lai, S. W.; Lin, H. L.; Lin, Y. P.; Yu, T. L. Hydrolysis of Ammonia-Borane Catalyzed by an Iron-Nickel Alloy on an SBA-15 Support. *Int. J. Hydrogen Energy* **2013**, *38* (11), 4636–4647. https://doi.org/10.1016/j.ijhydene.2013.01.156.

(48) Din, M.; Metin, Ö.; Özkar, S. Water Soluble Polymer Stabilized Iron(0) Nanoclusters: A Cost-Effective and Magnetically Recoverable Catalyst in Hydrogen Generation from the Hydrolysis of Sodium Borohydride and Ammonia Borane. *Catal. Today* **2012**, *183* (1), 10–16. https://doi.org/10.1016/j.cattod.2011.05.007.

(49) Wang, Z.; Chen, Y.; He, Y.; Jiang, W.; Long, Y.; Fan, G. Facile Construction of Composition-Tuned Ruthenium-Nickel Nanoparticles on g-C3N4 for Enhanced Hydrolysis of Ammonia Borane without Base Additives. *Int. J. Hydrogen Energy* **2021**, *46* (21), 11587–11596. https://doi.org/10.1016/j.ijhydene.2020.12.199.

(50) Zhang, J.; Li, J.; Yang, L.; Li, R.; Zhang, F.; Dong, H. Efficient Hydrogen Production from Ammonia Borane Hydrolysis Catalyzed by TiO2-Supported RuCo Catalysts. *Int. J. Hydrogen Energy* **2021**, *46* (5), 3964–3973. https://doi.org/10.1016/j.ijhydene.2020.10.234.

(51) Li, Y. T.; Zhang, X. L.; Peng, Z. K.; Liu, P.; Zheng, X. C. Hierarchical Porous G-C3N4Coupled Ultrafine RuNi Alloys as Extremely Active Catalysts for the Hydrolytic Dehydrogenation of Ammonia Borane. *ACS Sustain. Chem. Eng.* **2020**, *8* (22), 8458–8468. https://doi.org/10.1021/acssuschemeng.0c03009.

(52) Sevim, M.; Kaplan, F. Ketjen Black Supported Monodisperse Nickel–Platinum Alloy Nanoparticles for the Efficient Catalyst in the Hydrolytic Dehydrogenation of Ammonia Borane. *Appl. Organomet. Chem.* **2021**, *35* (2). https://doi.org/10.1002/aoc.6095.

(53) Rakap, M. Synthesis and Characterization of Bimetallic Cobalt-Rhodium Nanoclusters as Effective Catalysts to Produce Hydrogen from Ammonia Borane Hydrolysis. *Renew. Energy* **2020**, *154*, 1076–1082. https://doi.org/10.1016/j.renene.2020.03.088.

(54) Zhang, M.; Xiao, X.; Wu, Y.; An, Y.; Xu, L.; Wan, C. Hydrogen Production from Ammonia Borane over PtNi Alloy Nanoparticles Immobilized on Graphite Carbon Nitride. *Catalysts* **2019**, *9* (12). https://doi.org/10.3390/catal9121009.

(55) Zhang, J.; Chen, W.; Ge, H.; Chen, C.; Yan, W.; Gao, Z.; Gan, J.; Zhang, B.; Duan, X.; Qin, Y. Synergistic Effects in Atomic-Layer-Deposited PtCox/CNTs Catalysts Enhancing Hydrolytic Dehydrogenation of Ammonia Borane. *Appl. Catal. B Environ.* **2018**, *235*, 256–263. https://doi.org/10.1016/j.apcatb.2018.04.070.

(56) Karaca, T.; Sevim, M.; Metin, Ö. Facile Synthesis of Monodisperse Copper–Platinum Alloy Nanoparticles and Their Superb Catalysis in the Hydrolytic Dehydrogenation of Ammonia Borane and Hydrazine Borane. *ChemCatChem* **2017**, *9* (22), 4185–4190. https://doi.org/10.1002/cctc.201701023.

(57) Feng, Y.; Liao, J.; Chen, X.; Wang, H.; Guo, B.; Li, H.; Zhou, L.; Huang, J.; Li, H. Synthesis of Rattle-Structured CuCo2O4 Nanospheres with Tunable Sizes Based on Heterogeneous Contraction and Their Ultrahigh Performance toward Ammonia Borane Hydrolysis. *J. Alloys Compd.* **2021**, *863*. https://doi.org/10.1016/j.jallcom.2020.158089.

(58) Feng, Y.; Shao, Y.; Chen, X.; Zhang, Y.; Liu, Q.; He, M.; Li, H. Sea-Urchin-like Hollow CuMoO4-CoMoO4Hybrid Microspheres, a Noble-Metal-like Robust Catalyst for the Fast Hydrogen Production from Ammonia Borane. *ACS Appl. Energy Mater.* **2021**, *4* (1), 633–642. https://doi.org/10.1021/acsaem.0c02521.

(59) Wu, Y.; Sun, Y.; Fu, W.; Meng, X.; Zhu, M.; Ramakrishna, S.; Dai, Y. Graphene-Based Modulation on the Growth of Urchin-like Na 2 Ti 3 O 7 Microspheres for Photothermally Enhanced H 2 Generation from Ammonia Borane . *ACS Appl. Nano Mater.* **2020**, *3* (3), 2713–2722. https://doi.org/10.1021/acsanm.0c00071.

(60) Liu, Y.; Guo, H.; Sun, K.; Jiang, J. Magnetic CoOx@C-Reduced Graphene Oxide Composite with Catalytic Activity towards Hydrogen Generation. *Int. J. Hydrogen Energy* **2019**, *44* (52), 28163–28172. https://doi.org/10.1016/j.ijhydene.2019.09.034.

(61) Li, J.; Li, F.; Liao, J.; Liu, Q.; Li, H. Cu0.4 Co0.6 MoO4 Nanorods Supported on Graphitic Carbon Nitride as a Highly Active Catalyst for the Hydrolytic Dehydrogenation of Ammonia Borane. *Catalysts* **2019**, *9* (9). https://doi.org/10.3390/catal9090714.

(62) Shang, Y.; Feng, K.; Wang, Y.; Sun, X.; Zhong, J. Carbon Nitride Supported Ni0.5Co0.5O Nanoparticles with Strong Interfacial Interaction to Enhance the Hydrolysis of Ammonia Borane. *RSC Adv.* **2019**, *9* (20), 11552–11557. https://doi.org/10.1039/c9ra01743g.

(63) Song, J.; Gu, X.; Zhang, H. Electrons and Hydroxyl Radicals Synergistically Boost the Catalytic Hydrogen Evolution from Ammonia Borane over Single Nickel Phosphides under Visible Light Irradiation. *ChemistryOpen* **2020**, *9* (3), 366–373. https://doi.org/10.1002/open.201900335.

(64) Yang, J.; Yuan, Q.; Liu, Y.; Huang, X.; Qiao, Y.; Lu, J.; Song, C. Low-Cost Ternary Ni-Fe-P Catalysts Supported on Ni Foam for Hydrolysis of Ammonia Borane. *Inorg. Chem. Front.* **2019**, *6* (5), 1189–1194. https://doi.org/10.1039/c9qi00048h.

(65) Yang, C.; Men, Y.; Xu, Y.; Liang, L.; Cai, P.; Luo, W. In Situ Synthesis of NiCoP Nanoparticles Supported on Reduced Graphene Oxide for the Catalytic Hydrolysis of Ammonia Borane. *Chempluschem* **2019**, *84* (4), 382–386. https://doi.org/10.1002/cplu.201800670.

(66) Ozerova, A. M.; Bulavchenko, O. A.; Komova, O. V.; Netskina, O. V.; Zaikovskii, V. I.; Odegova, G. V.; Simagin, V. I. Cobalt Boride Catalysts for Hydrogen Storage Systems Based on NH 3BH 3 and NaBH 4. *Kinet. Catal.* **2012**, *53* (4), 511–520. https://doi.org/10.1134/S0023158412040088.

(67) Kang, Y.; Jiang, B.; Yang, J.; Wan, Z.; Na, J.; Li, Q.; Li, H.; Henzie, J.; Sakka, Y.; Yamauchi, Y.; Asahi, T. Amorphous Alloy Architectures in Pore Walls: Mesoporous Amorphous NiCoB Alloy Spheres with Controlled Compositions via a Chemical Reduction. *ACS Nano* **2020**, *14* (12), 17224–17232. https://doi.org/10.1021/acsnano.0c07178.

(68) Yu, Y.; Yang, W.; Sun, X.; Zhu, W.; Li, X. Z.; Sellmyer, D. J.; Sun, S. Monodisperse MPt (M = Fe, Co, Ni, Cu, Zn) Nanoparticles Prepared from a Facile Oleylamine Reduction of Metal Salts. *Nano Lett.* **2014**, *14* (5), 2778–2782. https://doi.org/10.1021/nl500776e.

(69) Zhang, J.; Chen, W.; Ge, H.; Chen, C.; Yan, W.; Gao, Z.; Gan, J.; Zhang, B.; Duan, X.; Qin, Y. Synergistic Effects in Atomic-Layer-Deposited PtCox/CNTs Catalysts Enhancing Hydrolytic Dehydrogenation of Ammonia Borane. *Appl. Catal. B Environ.* **2018**, *235*, 256–263. https://doi.org/10.1016/j.apcatb.2018.04.070.

(70) Slot, T. K.; Yue, F.; Xu, H.; Ramos-Fernandez, E. V.; Sepúlveda-Escribano, A.; Sofer, Z.; Rothenberg, G.; Raveendran Shiju, N. Surface Oxidation of Ti3C2Tx Enhances the Catalytic Activity of Supported Platinum Nanoparticles in Ammonia Borane Hydrolysis.

2D Mater. **2021**, *8* (1), 15001. https://doi.org/10.1088/2053-1583/ababef.

(71) Kamegawa, T.; Nakaue, T. Complete Hydrogen Release from Aqueous Ammonia-Borane over a Platinum-Loaded Titanium Dioxide Photocatalyst. *Chem. Commun.* **2015**, *51* (94), 16802–16805. https://doi.org/10.1039/c5cc06639e.

(72) Ju, Y.; Kim, J. Composition-Dependent Catalytic Activity of Bimetallic PtPd Dendrimer-Encapsulated Nanoparticles Having an Average Size of 1.7 Nm for Hydrolytic Dehydrogenation of Ammonia Borane. *Korean J. Chem. Eng* **2020**, *37* (8), 20. https://doi.org/10.1007/s11814-020-0604-4.

(73) Semiz, L. Hydrogen Generation from Ammonia Borane by Chemically Dealloyed Platinum Nanoparticles. *React. Kinet. Mech. Catal.* **2020**, *129* (1), 205–218. https://doi.org/10.1007/s11144-019-01700-y.

(74) Uzundurukan, A.; Devrim, Y. Carbon Nanotube-Graphene Hybrid Supported Platinum as an Effective Catalyst for Hydrogen Generation from Hydrolysis of Ammonia Borane. *Int. J. Hydrogen Energy* **2019**, *44* (49), 26773–26782. https://doi.org/10.1016/j.ijhydene.2019.08.153.

(75) Zhao, H.; Yu, G.; Yuan, M.; Yang, J.; Xu, D.; Dong, Z. Ultrafine and Highly Dispersed Platinum Nanoparticles Confined in a Triazinyl-Containing Porous Organic Polymer for Catalytic Applications. *Nanoscale* **2018**, *10* (45), 21466–21474. https://doi.org/10.1039/c8nr05756g.

(76) Deka, J. R.; Budi, C. S.; Lin, C. H.; Saikia, D.; Yang, Y. C.; Kao, H. M. Carboxylic Acid Functionalized Cage-Type Mesoporous Silica FDU-12 as Support for Controlled Synthesis of Platinum Nanoparticles and Their Catalytic Applications. *Chem. - A Eur. J.* **2018**, *24* (51), 13540–13548. https://doi.org/10.1002/chem.201802146.

(77) Zhou, Q.; Qi, L.; Yang, H.; Xu, C. Hierarchical Nanoporous Platinum–Copper Alloy Nanoflowers as Highly Active Catalysts for the Hydrolytic Dehydrogenation of Ammonia Borane. *J. Colloid Interface Sci.* **2018**, *513*, 258–265. https://doi.org/10.1016/j.jcis.2017.11.040.

(78) Zhou, Q.; Xu, C. Nanoporous PtCo/Co3O4 Composites with High Catalytic Activities toward Hydrolytic Dehydrogenation of Ammonia Borane. *J. Colloid Interface Sci.* **2017**, *508*, 542–550. https://doi.org/10.1016/j.jcis.2017.08.054.

(79) Yuan, M.; Cui, Z.; Yang, J.; Cui, X.; Tian, M.; Xu, D.; Ma, J.; Dong, Z. Ultrafine Platinum Nanoparticles Modified on Cotton Derived Carbon Fibers as a Highly Efficient Catalyst for Hydrogen Evolution from Ammonia Borane. *Int. J. Hydrogen Energy* **2017**, *42* (49), 29244–29253. https://doi.org/10.1016/j.ijhydene.2017.09.178.

(80) Zhou, Q.; Xu, C. Stratified Nanoporous PtTi Alloys for Hydrolysis of Ammonia Borane. *J. Colloid Interface Sci.* **2017**, *496*, 235–242. https://doi.org/10.1016/j.jcis.2017.02.030.

(81) Zhang, J.; Chen, C.; Chen, S.; Hu, Q.; Gao, Z.; Li, Y.; Qin, Y. Highly Dispersed Pt Nanoparticles Supported on Carbon Nanotubes Produced by Atomic Layer Deposition for Hydrogen Generation from Hydrolysis of Ammonia Borane. *Catal. Sci. Technol.* **2017**, *7* (2), 322–329. https://doi.org/10.1039/c6cy01960a.

(82) Yao, Q.; Shi, Y.; Zhang, X.; Chen, X.; Lu, Z. H. Facile Synthesis of Platinum–Cerium(IV) Oxide Hybrids Arched on Reduced Graphene Oxide Catalyst in Reverse Micelles with High Activity and Durability for Hydrolysis of Ammonia Borane. *Chem. - An Asian J.* **2016**, *11* (22), 3251–3257. https://doi.org/10.1002/asia.201601147.

(83) Zhou, Q.; Xu, C. Nanoporous PtRu Alloys with Unique Catalytic Activity toward Hydrolytic Dehydrogenation of Ammonia Borane. *Chem. - An Asian J.* **2016**, *11* (5), 705–712. https://doi.org/10.1002/asia.201500970.

(84) Yu, P. J.; Hsieh, C. C.; Chen, P. Y.; Weng, B. J.; Chen-Yang, Y. W. Highly Active and Reusable Silica-Aerogel-Supported Platinum-Cobalt Bimetallic Catalysts for the Dehydrogenation of Ammonia Borane. *RSC Adv.* **2016**, *6* (113), 112109–112116. https://doi.org/10.1039/C6RA24249A.

(85) Hu, Y.; Wang, Y.; Lu, Z. H.; Chen, X.; Xiong, L. Core-Shell Nanospheres Pt@SiO 2 for Catalytic Hydrogen Production. *Appl. Surf. Sci.* **2015**, *341*, 185–189. https://doi.org/10.1016/j.apsusc.2015.02.094.

(86) Rakap, M. Poly(N-Vinyl-2-Pyrrolidone)-Stabilized Palladium-Platinum Nanoparticles-Catalyzed Hydrolysis of Ammonia Borane for Hydrogen Generation. *J. Power Sources* **2015**, *276*, 320–327. https://doi.org/10.1016/j.jpowsour.2014.11.146.

(87) Rakap, M. Hydrogen Generation from Hydrolysis of Ammonia Borane in the Presence of Highly Efficient Poly(N-Vinyl-2-Pyrrolidone)-Protected Platinum-Ruthenium Nanoparticles. *Appl. Catal. A Gen.* **2014**, *478*, 15–20. https://doi.org/10.1016/j.apcata.2014.03.022.

(88) Wang, L.; Wang, K.; He, T.; Zhao, Y.; Song, H.; Wang, H. Graphitic Carbon Nitride-Based Photocatalytic Materials: Preparation Strategy and Application. *ACS Sustain. Chem. Eng.* **2020**, acssuschemeng.0c05246. https://doi.org/10.1021/acssuschemeng.0c05246.

(89) Thomas, A.; Fischer, A.; Goettmann, F.; Antonietti, M.; Müller, J. O.; Schlögl, R.; Carlsson, J. M. Graphitic Carbon Nitride Materials: Variation of Structure and Morphology and Their Use as Metal-Free Catalysts. *J. Mater. Chem.* **2008**, *18* (41), 4893–4908. https://doi.org/10.1039/b800274f.

(90) Zhu, J.; Xiao, P.; Li, H.; Carabineiro, S. A. C. Graphitic Carbon Nitride: Synthesis, Properties, and Applications in Catalysis. *ACS Applied Materials and Interfaces*. American Chemical Society October 8, 2014, pp 16449–16465. https://doi.org/10.1021/am502925j.

(91) Chen, Z.; Mitchell, S.; Vorobyeva, E.; Leary, R. K.; Hauert, R.; Furnival, T.; Ramasse, Q. M.; Thomas, J. M.; Midgley, P. A.; Dontsova, D.; Antonietti, M.; Pogodin, S.; López, N.; Pérez-Ramírez, J. Stabilization of Single Metal Atoms on Graphitic Carbon Nitride. *Adv. Funct. Mater.* **2017**, *27* (8), 1605785. https://doi.org/10.1002/adfm.201605785.

(92) Vilé, G.; Albani, D.; Nachtegaal, M.; Chen, Z.; Dontsova, D.; Antonietti, M.; López, N.; Pérez-Ramírez, J. A Stable Single-Site Palladium Catalyst for Hydrogenations. *Angew. Chemie - Int. Ed.* **2015**, *54* (38), 11265–11269. https://doi.org/10.1002/anie.201505073.

(93) Gao, G.; Jiao, Y.; Waclawik, E. R.; Du, A. Single Atom (Pd/Pt) Supported on Graphitic Carbon Nitride as an Efficient Photocatalyst for Visible-Light Reduction of Carbon Dioxide. *J. Am. Chem. Soc.* **2016**, *138* (19), 6292–6297. https://doi.org/10.1021/jacs.6b02692.

(94) Khan, M. R.; Chuan, T. W.; Yousuf, A.; Chowdhury, M. N. K.; Cheng, C. K. Schottky Barrier and Surface Plasmonic Resonance Phenomena towards the Photocatalytic Reaction: Study of Their Mechanisms to Enhance Photocatalytic Activity. *Catalysis Science and Technology*. Royal Society of Chemistry May 1, 2015, pp 2522–2531. https://doi.org/10.1039/c4cy01545b.

(95) Kavitha, R.; Nithya, P. M.; Girish Kumar, S. Noble Metal Deposited Graphitic Carbon Nitride Based Heterojunction Photocatalysts. *Applied Surface Science*. Elsevier B.V. April 1, 2020, p 145142. https://doi.org/10.1016/j.apsusc.2019.145142.

(96) Bumajdad, A.; Madkour, M. Understanding the Superior Photocatalytic Activity of Noble Metals Modified Titania under UV and Visible Light Irradiation. *Physical Chemistry Chemical Physics*. Royal Society of Chemistry April 28, 2014, pp 7146–7158. https://doi.org/10.1039/c3cp54411g.

(97) Cai, Y.-Y.; Li, X.-H.; Zhang, Y.-N.; Wei, X.; Wang, K.-X.; Chen, J.-S. Highly Efficient Dehydrogenation of Formic Acid over a Palladium-Nanoparticle-Based Mott-Schottky Photocatalyst. *Angew. Chemie Int. Ed.* **2013**, *52* (45), 11822–11825. https://doi.org/10.1002/anie.201304652.

(98) Li, X. H.; Antonietti, M. Metal Nanoparticles at Mesoporous N-Doped Carbons and Carbon Nitrides: Functional Mott–Schottky Heterojunctions for Catalysis. *Chem. Soc. Rev.* **2013**, *42* (16), 6593–6604. https://doi.org/10.1039/c3cs60067j.

(99) Kontoleta, E.; Tsoukala, A.; Askes, S. H. C.; Zoethout, E.; Oksenberg, E.; Agrawal, H.; Garnett, E. C. Using Hot Electrons and Hot Holes for Simultaneous Cocatalyst Deposition on Plasmonic Nanostructures. *ACS Appl. Mater. Interfaces* **2020**, *12* (32), 35986–35994. https://doi.org/10.1021/acsami.0c04941.

(100) Wang, L.; Tong, Y.; Feng, J.; Hou, J.; Li, J.; Hou, X.; Liang, J. G-C3N4-Based Films: A Rising Star for Photoelectrochemical Water Splitting. *Sustainable Materials and Technologies*. Elsevier B.V. April 1, 2019, p e00089. https://doi.org/10.1016/j.susmat.2018.e00089.

(101) Murugan, C.; Bhojanaa, K. B.; Ong, W. J.; Jothivenkatachalam, K.; Pandikumar, A. Improving Hole Mobility with the Heterojunction of Graphitic Carbon Nitride and Titanium Dioxide via Soft Template Process in Photoelectrocatalytic Water Splitting. *Int. J. Hydrogen Energy* **2019**, *44* (59), 30885–30898. https://doi.org/10.1016/j.ijhydene.2019.09.114.

(102) Shin, H.; Jung, W. G.; Kim, D. H.; Jang, J. S.; Kim, Y. H.; Koo, W. T.; Bae, J.; Park, C.; Cho, S. H.; Kim, B. J.; Kim, I. D. Single-Atom Pt Stabilized on One-Dimensional Nanostructure Support via Carbon Nitride/SnO2Heterojunction Trapping. *ACS Nano* **2020**, *14* (9), 11394–11405. https://doi.org/10.1021/acsnano.0c03687.

(103) Shao, B.; Liu, X.; Liu, Z.; Zeng, G.; Zhang, W.; Liang, Q.; Liu, Y.; He, Q.; Yuan, X.; Wang, D.; Luo, S.; Gong, S. Synthesis and Characterization of 2D/0D g-C3N4/CdS-Nitrogen Doped Hollow Carbon Spheres (NHCs)Composites with Enhanced Visible Light Photodegradation Activity for Antibiotic. *Chem. Eng. J.* **2019**, *374*, 479–493. https://doi.org/10.1016/j.cej.2019.05.202.

(104) Kim, W. J.; Jang, E.; Park, T. J. Enhanced Visible-Light Photocatalytic Activity of ZnS/g-C 3 N 4 Type-II Heterojunction Nanocomposites Synthesized with Atomic Layer Deposition. *Appl. Surf. Sci.* **2017**, *419*, 159–164. https://doi.org/10.1016/j.apsusc.2017.05.012.

(105) Guo, F.; Shi, W.; Lin, X.; Che, G. Hydrothermal Synthesis of Graphitic Carbon Nitride-BiVO4 Composites with Enhanced Visible Light Photocatalytic Activities and the Mechanism Study. *J. Phys. Chem. Solids* **2014**, *75* (11), 1217–1222. https://doi.org/10.1016/j.jpcs.2014.05.011.

(106) Ma, X.; Chen, Q.; Liu, G.; Zhou, Y.; Ma, D.; Xin, S.; Yu, C.; Zhang, B.; Xin, Y. Construction of Netlike 3D Z-Scheme Photoelectrodes with Improved Photocatalytic Performance Based on g-C3N4 Nanosheets Modified TiO2 Nanobelt-Tubes. *Chem. Eng. Sci.* **2020**, *226*, 115844. https://doi.org/10.1016/j.ces.2020.115844.

(107) Duan, B.; Mei, L. A Z-Scheme Fe2O3/g-C3N4 Heterojunction for Carbon Dioxide to Hydrocarbon Fuel under Visible Illuminance. *J. Colloid Interface Sci.* **2020**, *575*, 265–273. https://doi.org/10.1016/j.jcis.2020.04.112.

(108) Ye, R.; Fang, H.; Zheng, Y. Z.; Li, N.; Wang, Y.; Tao, X. Fabrication of CoTiO3/g-C3N4 Hybrid Photocatalysts with Enhanced H2 Evolution: Z-Scheme Photocatalytic Mechanism Insight. *ACS Appl. Mater. Interfaces* **2016**, *8* (22), 13879–13889. https://doi.org/10.1021/acsami.6b01850.

(109) Li, L.; Jiang, D.; Wu, X.; Sun, X.; Qu, X.; Shi, L.; Du, F. 2D/2D WO3·H2O/g-C3N4 Heterostructured Assemblies for Enhanced Photocatalytic Water Decontamination via Strong Interfacial Contact. *J. Mater. Sci.* **2020**, *55* (10), 4238–4250. https://doi.org/10.1007/s10853-019-04264-3.

(110) Li, X.; Song, X.; Ma, C.; Cheng, Y.; Shen, D.; Zhang, S.; Liu, W.; Huo, P.; Wang, H. Direct Z-Scheme WO3/Graphitic Carbon Nitride Nanocomposites for the Photoreduction of CO2. *ACS Appl. Nano Mater.* **2020**, *3* (2), 1298–1306. https://doi.org/10.1021/acsanm.9b02083.

(111) Jaryal, A.; Battula, V. R.; Kailasam, K. Oxygen Deficient WO3- XNanorods and g-CN Nanosheets Heterojunctions: A 1D-2D Interface with Engineered Band Structure for Cyclohexanol Oxidation in Visible Light. *ACS Appl. Energy Mater.* **2020**, *3* (5), 4669–4676. https://doi.org/10.1021/acsaem.0c00302.

(112) Ishikawa, Y.; Liao, M. S.; Cabrera, C. R. Energetics of H2O Dissociation and COads + OHads Reaction on a Series of Pt-M Mixed Metal Clusters: A Relativistic Density-Functional Study. *Surf. Sci.* **2002**, *513* (1), 98–110. https://doi.org/10.1016/S0039-6028(02)01697-7.

(113) Chen, W.; Fu, W.; Qian, G.; Zhang, B.; Chen, D.; Duan, X.; Zhou, X. Synergistic Pt-WO3 Dual Active Sites to Boost Hydrogen Production from Ammonia Borane. *iScience* **2020**, *23* (3), 100922. https://doi.org/10.1016/j.isci.2020.100922.

(114) Jafari, T.; Moharreri, E.; Amin, A. S.; Miao, R.; Song, W.; Suib, S. L. Photocatalytic Water Splitting - The Untamed Dream: A Review of Recent Advances. *Molecules*. MDPI AG July 1, 2016. https://doi.org/10.3390/molecules21070900.

(115) Aksoy, M.; Metin, Ö. Pt Nanoparticles Supported on Mesoporous Graphitic Carbon Nitride as Catalysts for Hydrolytic Dehydrogenation of Ammonia Borane. *ACS Appl. Nano Mater.* **2020**. https://doi.org/10.1021/acsanm.0c01208.

(116) Erdogan, D. A.; Sevim, M.; Kısa, E.; Emiroglu, D. B.; Karatok, M.; Vovk, E. I.; Bjerring, M.; Akbey, Ü.; Metin, Ö.; Ozensoy, E. Photocatalytic Activity of Mesoporous Graphitic Carbon Nitride (Mpg-C3N4) Towards Organic Chromophores Under UV and VIS Light Illumination. *Top. Catal.* **2016**, *59* (15–16), 1305–1318. https://doi.org/10.1007/s11244-016-0654-3.

(117) Nişancı, B.; Turgut, M.; Sevim, M.; Metin, Ö. Three-Component Cascade Reaction in a Tube: In Situ Synthesis of Pd Nanoparticles Supported on Mpg-C3N4, Dehydrogenation of Ammonia Borane and Hydrogenation of Nitroarenes. *ChemistrySelect* **2017**, *2* (22), 6344–6349. https://doi.org/10.1002/slct.201701188.

(118) Sevim Yılmaz, M.; Kaplan, B. Y.; Metin, Ö.; Gürsel, S. A. A Facile Synthesis and Assembly of Ultrasmall Pt Nanoparticles on Reduced Graphene Oxide-carbon Black Hybrid for Enhanced Performance in PEMFC. *Mater. Des.* **2018**, *151*, 29–36. https://doi.org/10.1016/j.matdes.2018.04.041.

(119) Zhao, B.; Wang, B.; Lu, H.; Dai, S.; Huang, Z. Tuning the Visible-Light Photocatalytic Degradation Activity of Thin Nanosheets Constructed Porous g-C3N4 Microspheres by Decorating Ionic Liquid Modified Carbon Dots: Roles of Heterojunctions and Surface Charges. *New J. Chem.* **2019**, *43* (25), 10141–10150. https://doi.org/10.1039/c9nj00308h.

(120) Ergen, S.; Nişanci, B.; Metin, Ö. One-Pot Reductive Amination of Aldehydes with Nitroarenes Using Formic Acid as the Hydrogen Donor and Mesoporous Graphitic Carbon Nitride Supported AgPd Alloy Nanoparticles as the Heterogeneous Catalyst. *New J. Chem.* **2018**, *42* (12), 10000–10006. https://doi.org/10.1039/c8nj01569d.

(121) Dupin, J.-C.; Gonbeau, D.; Vinatierb, P.; Levasseurb, A. Systematic XPS Studies of Metal Oxides, Hydroxides and Peroxides. https://doi.org/10.1039/a908800h.

(122) Cai, Q.; Hong, W.; Li, J.; Jian, C.; Liu, W. A Silicon Photoanode for Efficient Ethanol Oxidation under Alkaline Conditions. *RSC Adv.* **2017**, *7* (35), 21809–21814. https://doi.org/10.1039/c7ra02848b.

(123) Eguiluz, K. I. B.; Malpass, G. R. P.; Pupo, M. M. S.; Salazar-Banda, G. R.; Avaca, L. A. Synthesis, Characterization, and Electrocatalytic Activity toward Methanol Oxidation of Carbon-Supported Ptx-(RuO2-M)1- x Composite Ternary Catalysts (M = CeO2, MoO3, or PbO X). *Energy and Fuels* **2010**, *24* (7), 4012–4024. https://doi.org/10.1021/ef100424m.

(124) Romanchenko, A.; Likhatski, M.; Mikhlin, Y. X-Ray Photoelectron Spectroscopy (XPS) Study of the Products Formed on Sulfide Minerals Upon the Interaction with Aqueous Platinum (IV) Chloride Complexes. *Minerals* **2018**, *8* (12), 578. https://doi.org/10.3390/min8120578.

(125) Shi, Q.; Zhu, C.; Engelhard, M. H.; Du, D.; Lin, Y. Highly Uniform Distribution of Pt Nanoparticles on N-Doped Hollow Carbon Spheres with Enhanced Durability for Oxygen Reduction Reaction. **2017**. https://doi.org/10.1039/c6ra25391a.

(126) Torrent, J.; Barrón, V. Diffuse Reflectance Spectroscopy. In *Methods of Soil Analysis, Part 5: Mineralogical Methods*; wiley, 2015; Vol. 5, pp 367–385. https://doi.org/10.2136/sssabookser5.5.c13.

(127) Makuła, P.; Pacia, M.; Macyk, W. How To Correctly Determine the Band Gap Energy of Modified Semiconductor Photocatalysts Based on UV-Vis Spectra. *Journal of Physical Chemistry Letters*. American Chemical Society December 6, 2018, pp 6814–6817. https://doi.org/10.1021/acs.jpclett.8b02892.

(128) Chen, H. W.; Ku, Y.; Kuo, Y. L. Effect of Pt/TiO2 Characteristics on Temporal Behavior of o-Cresol Decomposition by Visible Light-Induced Photocatalysis. *Water Res.* **2007**, *41* (10), 2069–2078. https://doi.org/10.1016/j.watres.2007.02.021.

(129) Eken Korkut, S.; Küçükkeçeci, H.; Metin, Ö. Mesoporous Graphitic Carbon Nitride/Black Phosphorus/AgPd Alloy Nanoparticles Ternary Nanocomposite: A Highly Efficient Catalyst for the Methanolysis of Ammonia Borane. *ACS Appl. Mater. Interfaces* **2020**, *12* (7), 8130–8139. https://doi.org/10.1021/acsami.9b18917.

(130) Watzky, M. A.; Finke, R. G. Transition Metal Nanocluster Formation Kinetic and Mechanistic Studies. A New Mechanism When Hydrogen Is the Reductant: Slow, Continuous Nucleation and Fast Autocatalytic Surface Growth. *J. Am. Chem. Soc.* **1997**, *119* (43), 10382–10400. https://doi.org/10.1021/ja9705102.

(131) Widegren, J. A.; Aiken, J. D.; Özkar, S.; Finke, R. G. Additional Investigations of a New Kinetic Method to Follow Transition-Metal Nanocluster Formation, Including the Discovery of Heterolytic Hydrogen Activation in Nanocluster Nucleation Reactions. *Chem. Mater.* **2001**, *13* (2), 312–324. https://doi.org/10.1021/cm0006852.

(132) Akbayrak, S.; Kaya, M.; Volkan, M.; Özkar, S. Ruthenium(0) Nanoparticles Supported on Magnetic Silica Coated Cobalt Ferrite: Reusable Catalyst in Hydrogen Generation from the Hydrolysis of Ammonia-Borane. *J. Mol. Catal. A Chem.* **2014**, *394*, 253–261. https://doi.org/10.1016/j.molcata.2014.07.010.

(133) Guo, L. T.; Cai, Y. Y.; Ge, J. M.; Zhang, Y. N.; Gong, L. H.; Li, X. H.; Wang, K. X.; Ren, Q. Z.; Su, J.; Chen, J. S. Multifunctional Au-Co@CN Nanocatalyst for Highly Efficient Hydrolysis of Ammonia Borane. *ACS Catal.* **2015**, *5* (1), 388–392. https://doi.org/10.1021/cs501692n.

(134) Gao, M.; Yu, Y.; Yang, W.; Li, J.; Xu, S.; Feng, M.; Li, H. Ni Nanoparticles Supported on Graphitic Carbon Nitride as Visible Light Catalysts for Hydrolytic Dehydrogenation of Ammonia Borane. *Nanoscale* **2019**, *11* (8), 3506–3513. https://doi.org/10.1039/C8NR09005J.

(135) Neelgund, G. M.; Oki, A. Photothermal Effect: An Important Aspect for the Enhancement of Photocatalytic Activity under Illumination by NIR Radiation. *Mater. Chem. Front.* **2018**, *2* (1), 64–75. https://doi.org/10.1039/C7QM00337D.

(136) Mohajeri, N.; T-Raissi, A.; Adebiyi, O. Hydrolytic Cleavage of Ammonia-Borane Complex for Hydrogen Production. *J. Power Sources* **2007**, *167* (2), 482–485. https://doi.org/10.1016/j.jpowsour.2007.02.059.

(137) Wang, W.; Lu, Z.-H.; Luo, Y.; Zou, A.; Yao, Q.; Chen, X. Mesoporous Carbon Nitride Supported Pd and Pd-Ni Nanoparticles as Highly Efficient Catalyst for Catalytic Hydrolysis of NH_3BH_3. *ChemCatChem* **2018**, *10* (7), 1620–1626. https://doi.org/10.1002/cctc.201701989.

(138) Altan, O.; Metin, Ö. Boosting Formic Acid Dehydrogenation via the Design of a Z-Scheme Heterojunction Photocatalyst: The Case of Graphitic Carbon Nitride/Ag/Ag3PO4-AgPd Quaternary Nanocomposites. *Appl. Surf. Sci.* **2021**, *535*, 147740. https://doi.org/10.1016/j.apsusc.2020.147740.

(139) O. Altan. Impact of Graphitic Carbon Nitrides Synthesized from Different Precursors on Schottky Junction Charactersitics. *Turkish J. Chem.* **2021**, *In press*.

(140) Dong, F.; Wang, Z.; Sun, Y.; Ho, W. K.; Zhang, H. Engineering the Nanoarchitecture and Texture of Polymeric Carbon Nitride Semiconductor for Enhanced Visible Light Photocatalytic Activity. *J. Colloid Interface Sci.* **2013**, *401*, 70–79. https://doi.org/10.1016/j.jcis.2013.03.034.

(141) Mishra, U. K.; Singh, J. *Semiconductor Device Physics and Design*; Springer Netherlands, 2008. https://doi.org/10.1007/978-1-4020-6481-4.

(142) Moniri, S.; Reza Hantehzadeh, M.; Ghoranneviss, M.; Asadi Asadabad, M. Au-Pt Alloy Nanoparticles Obtained by Nanosecond Laser Irradiation of Gold and Platinum Bulk Targets in an Ethylene Glycol Solution. *Eur. Phys. J. Plus* **2017**, *132* (7). https://doi.org/10.1140/epjp/i2017-11582-9.

(143) Rahmi, E.; Umar, A. A.; Rahman, M. Y. A.; Salleh, M. M.; Oyama, M. Fibrous AuPt Bimetallic Nanocatalyst with Enhanced Catalytic Performance. *RSC Adv.* **2016**, *6* (33), 27696–27705. https://doi.org/10.1039/C5RA27849J.

(144) Feng, J.; Huang, P.; Wu, F.-Y. Gold–Platinum Bimetallic Nanoclusters with Enhanced Peroxidase-like Activity and Their Integrated Agarose Hydrogel-Based Sensing Platform for the Colorimetric Analysis of Glucose Levels in Serum. *Analyst* **2017**, *142* (21), 4106–4115. https://doi.org/10.1039/C7AN01343D.

(145) Wang, D.; Cui, X.; Xiao, Q.; Hu, Y.; Wang, Z.; Yiu, Y. M.; Sham, T. K. Electronic Behaviour of Au-Pt Alloys and the 4f Binding Energy Shift Anomaly in Au Bimetallics- X-Ray Spectroscopy Studies. *AIP Adv.* **2018**, *8* (6), 65210. https://doi.org/10.1063/1.5027251.

(146) Cao, S.; Li, H.; Tong, T.; Chen, H. C.; Yu, A.; Yu, J.; Chen, H. M. Single-Atom Engineering of Directional Charge Transfer Channels and Active Sites for Photocatalytic Hydrogen Evolution. *Adv. Funct. Mater.* **2018**, *28* (32), 1802169. https://doi.org/10.1002/adfm.201802169.

(147) Aksoy, İ.; Küçükkeçeci, H.; Sevgi, F.; Metin, Ö.; Hatay Patir, I. Photothermal Antibacterial and Antibiofilm Activity of Black Phosphorus/Gold Nanocomposites against Pathogenic Bacteria. *ACS Appl. Mater. Interfaces* **2020**, *12* (24), 26822–26831. https://doi.org/10.1021/acsami.0c02524.

(148) Yang, X.; Cheng, F.; Liang, J.; Tao, Z.; Chen, J. PtxNi1-x Nanoparticles as Catalysts for Hydrogen Generation from Hydrolysis of Ammonia Borane. *Int. J. Hydrogen Energy* **2009**, *34* (21), 8785–8791. https://doi.org/10.1016/j.ijhydene.2009.08.075.

(149) Ke, D.; Wang, J.; Zhang, H.; Li, Y.; Zhang, L.; Zhao, X.; Han, S. Fabrication of Pt–Co NPs Supported on Nanoporous Graphene as High-Efficient Catalyst for Hydrolytic Dehydrogenation of Ammonia Borane. *Int. J. Hydrogen Energy* **2017**, *42* (43), 26617–26625. https://doi.org/10.1016/j.ijhydene.2017.09.121.

(150) Zhang, S.; Li, M.; Zhao, J.; Wang, H.; Zhu, X.; Han, J.; Liu, X. Plasmonic AuPd-Based Mott-Schottky Photocatalyst for Synergistically Enhanced Hydrogen Evolution from Formic Acid and Aldehyde. *Appl. Catal. B Environ.* **2019**, *252*, 24–32. https://doi.org/10.1016/j.apcatb.2019.04.013.

(151) Kumar, S.; Tonda, S.; Baruah, A.; Kumar, B.; Shanker, V. Synthesis of Novel and Stable G-C3N4/N-Doped SrTiO3 Hybrid Nanocomposites with Improved Photocurrent and Photocatalytic Activity under Visible Light Irradiation. *Dalt. Trans.* **2014**, *43* (42), 16105–16114. https://doi.org/10.1039/c4dt01076k.

(152) He, Y.; Zhang, L.; Fan, M.; Wang, X.; Walbridge, M. L.; Nong, Q.; Wu, Y.; Zhao, L. Z-Scheme SnO2-x/g-C3N4 Composite as an Efficient Photocatalyst for Dye Degradation and Photocatalytic CO2 Reduction. *Sol. Energy Mater. Sol. Cells* **2015**, *137*, 175–184. https://doi.org/10.1016/j.solmat.2015.01.037.

(153) Liu, X.; Jin, A.; Jia, Y.; Jiang, J.; Hu, N.; Chen, X. Facile Synthesis and Enhanced Visible-Light Photocatalytic Activity of Graphitic Carbon Nitride Decorated with Ultrafine Fe2O3 Nanoparticles. *RSC Adv.* **2015**, *5* (112), 92033–92041. https://doi.org/10.1039/c5ra18466e.

(154) Kim, G.; Cho, H. J.; Sheu, Y.-M.; Ohta, H. Electrical, Optical, and Thermal Transport Properties of Oxygen-Deficient Amorphous WOx ($2.5 < x < 3$) Films. *J. Phys. Chem. C* **2019**. https://doi.org/10.1021/ACS.JPCC.9B02448.

(155) Liu, Y.; Dong, X.; Yuan, Q.; Liang, J.; Zhou, Y.; Qu, X.; Dong, B. In-Situ Synthesis of WO3–x/MoO3–x Heterojunction with Abundant Oxygen Vacancies for Efficient Photocatalytic Reduction of CO2. *Colloids Surfaces A Physicochem. Eng. Asp.* **2021**, *621*, 126582. https://doi.org/10.1016/j.colsurfa.2021.126582.

(156) Li, K.; Huang, Z.; Zeng, X.; Huang, B.; Gao, S.; Lu, J. Synergetic Effect of Ti3+ and Oxygen Doping on Enhancing Photoelectrochemical and Photocatalytic Properties of TiO2/g-C3N4 Heterojunctions. *ACS Appl. Mater. Interfaces* **2017**, *9* (13), 11577–11586. https://doi.org/10.1021/acsami.6b16191.

(157) Lee, S. Y.; Shim, G.; Park, J.; Seo, H. Tunable Polaron-Induced Coloration of Tungsten Oxide: Via a Multi-Step Control of the Physicochemical Property for the Detection of Gaseous F. *Phys. Chem. Chem. Phys.* **2018**, *20* (25), 16932–16938. https://doi.org/10.1039/c8cp00158h.

(158) Lett, C.; Yun, Y.; Araujo, J. R.; Melaet, G.; Baek, J.; Archanjo, B. S.; Oh, M.; Alivisatos, · A Paul; Gabor, ·; Somorjai, A. Activation of Tungsten Oxide for Propane Dehydrogenation and Its High Catalytic Activity and Selectivity. *Catal. Letters* **1915**, *0*, 3. https://doi.org/10.1007/s10562-016-1915-2.

(159) Bouvard, O.; Krammer, A.; Schüler, A. In Situ Core-Level and Valence-Band Photoelectron Spectroscopy of Reactively Sputtered Tungsten Oxide Films. In *Surface and Interface Analysis*; John Wiley and Sons Ltd, 2016; Vol. 48, pp 660–663. https://doi.org/10.1002/sia.5927.

(160) Liu, X.; Jin, A.; Jia, Y.; Xia, T.; Deng, C.; Zhu, M.; Chen, C.; Chen, X. Synergy of Adsorption and Visible-Light Photocatalytic Degradation of Methylene Blue by a Bifunctional Z-Scheme Heterojunction of WO 3 /g-C 3 N 4. *Appl. Surf. Sci.* **2017**, *405*, 359–371. https://doi.org/10.1016/j.apsusc.2017.02.025.

Appendix A

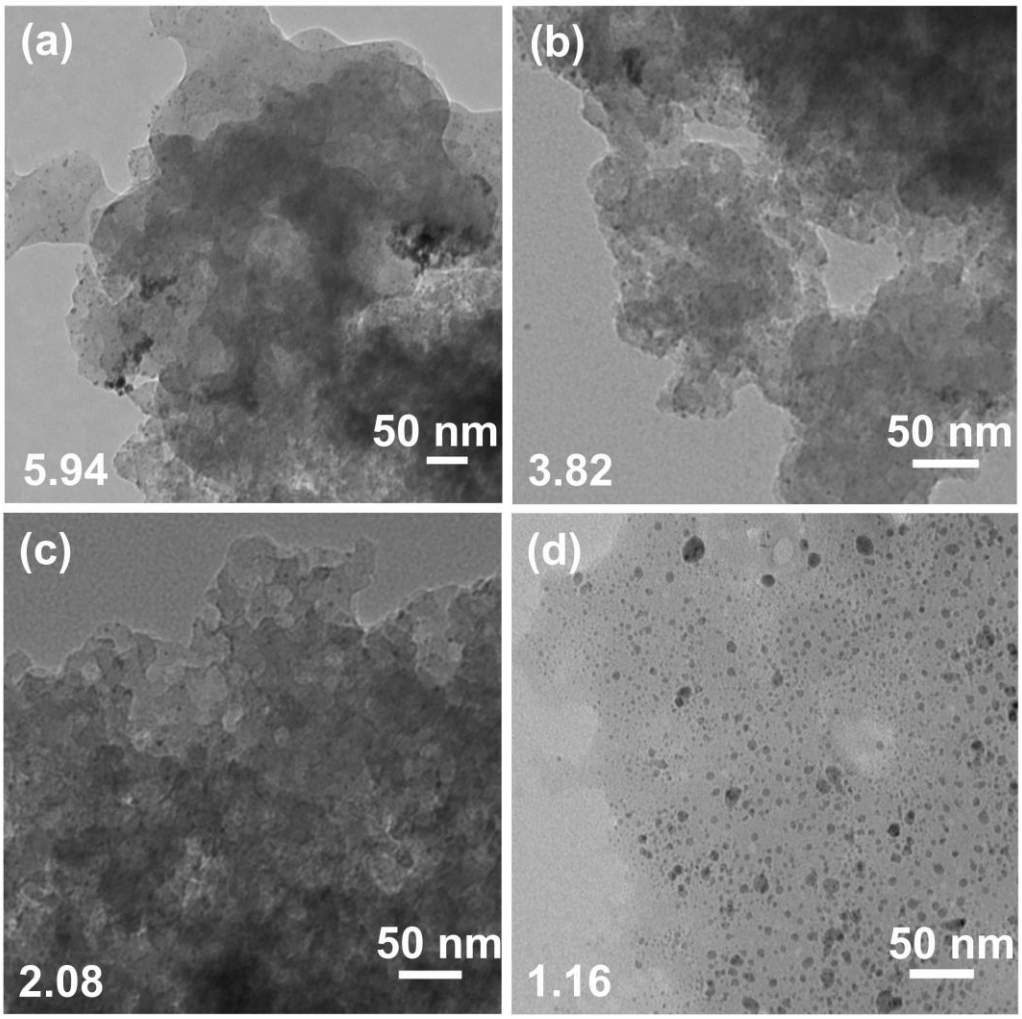

Figure A1: TEM images of m-g-CN /Pt nanocomposites with different Pt loadings (a) 5.94, (b) 3.82, (c) 2.08, and (d) 1.16 wt% Pt with scale bar 50 nm.[115]

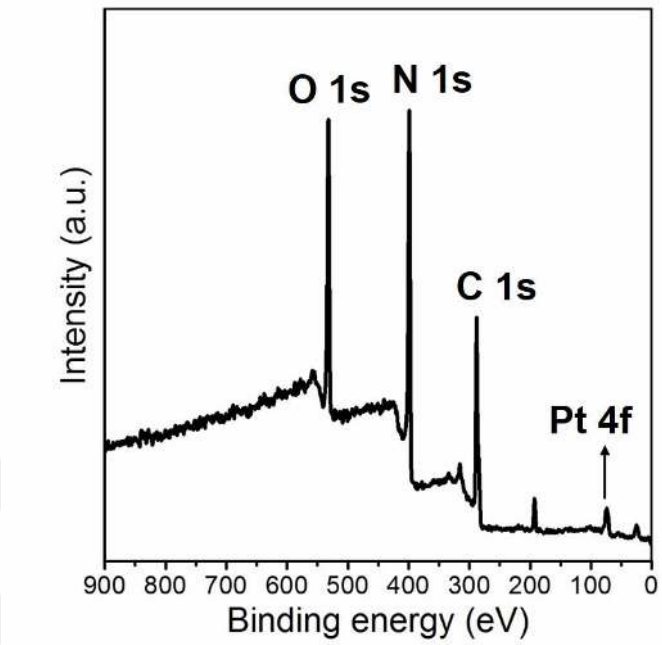

Figure A2: XPS survey spectra of m-g-CN/Pt nanocatalysts (3.82 wt% Pt).[115]

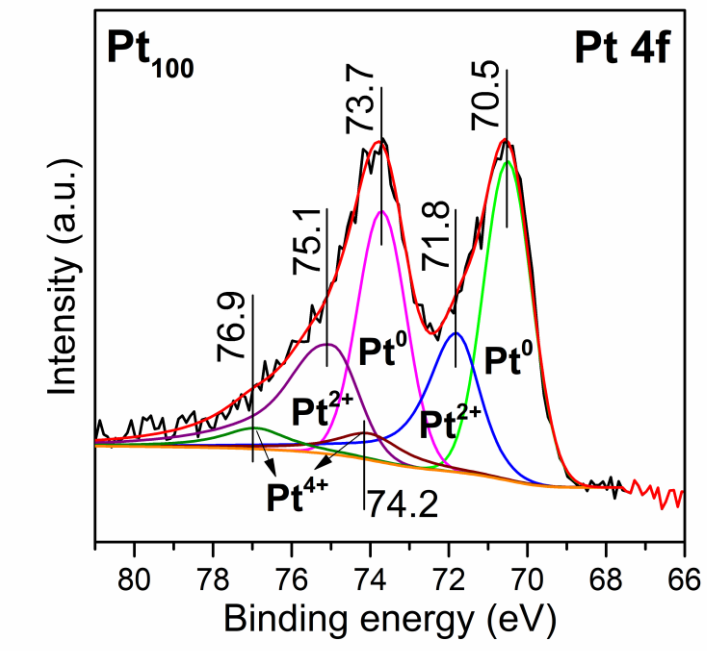

Figure A3: HR-XPS spectra of Pt 4f region of U-g-CN/Pt_{100} nanocatalyst.

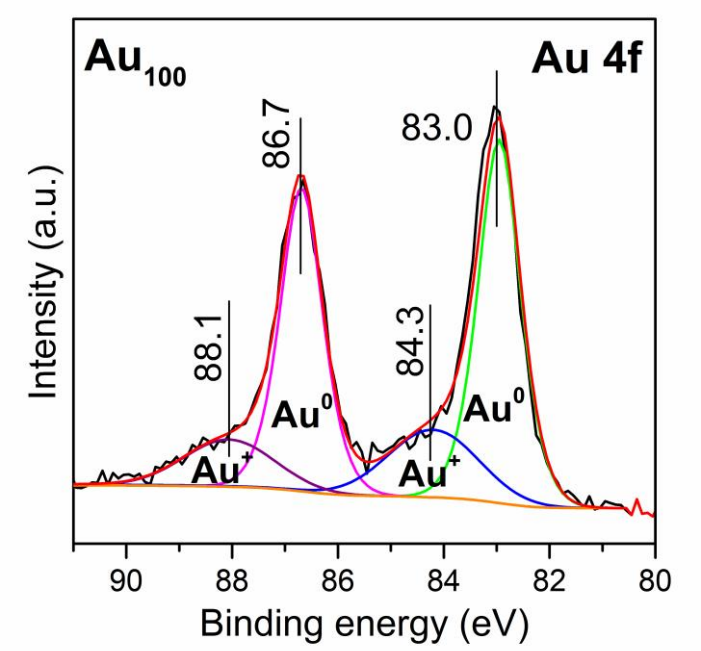

Figure A4: HR-XPS spectra of Au 4f region of U-g-CN/Au_{100} nanocatalysts.

Table A.1: The values of rate constant (k_{obs}) for the HAB catalyzed by m-g-CN/Pt (3.82 wt% Pt) nanocatalysts, calculated by the volume of hydrogen produced versus time, at different reaction conditions including [AB] = 100 mM, [Pt] = 0.2 mM, and T = 288-303 K.

Temperature (K)	Rate Constant, k_{app} (mol H_2 (mol Pt)$^{-1}$ min^{-1})
288	48.23
293	69.21
298	88.08
303	113.2

Table A.2: The values of rate constant (k_{obs}) for the HAB catalyzed by U-g-CN/$Pt_{92}M_8$ nanocatalysts, calculated by the volume of hydrogen produced versus time, at different reaction conditions including [AB] = 100 mM, [Pt] = 0.0831 mM, and T = 288-303 K.

Temperature (K)	Rate Constant, k_{app} (mol H_2 (mol Pt)$^{-1}$ min^{-1})
288	292.8
293	417.3
298	585.6
303	878.5

Table A.3: The values of rate constant (k_{obs}) for the HAB catalyzed by U-g-CN/WO_x/Pt (4.72 wt% W) nanocatalysts, calculated by the volume of hydrogen produced versus time, at different reaction conditions including [AB] = 100 mM, [Pt] = 0.0348 mM, and T = 288-303 K.

Temperature (K)	Rate Constant, k_{app} (mol H_2 (mol Pt)$^{-1}$ min^{-1})
288	104.8
293	219.7
298	317.1
303	541.7